UNIVERSITY OF OKLAHOMA
GRADUATE COLLEGE

INVESTIGATIONS OF THE MICROSTRUCTURAL AND MECHANICAL PROPERTIES OF THE FOUR HEART VALVES

A THESIS
SUBMITTED TO THE GRADUATE FACULTY
in partial fulfillment of the requirements for the
Degree of
MASTER OF SCIENCE

By
LUKE THOMAS HUDSON
Norman, Oklahoma
2021

INVESTIGATIONS OF THE MICROSTRUCTURAL AND MECHANICAL PROPERTIES OF THE FOUR HEART VALVES

A THESIS APPROVED FOR THE
SCHOOL OF AEROSPACE AND MECHANICAL ENGINEERING

BY THE COMMITTEE CONSISTING OF

Dr. Chung-Hao Lee, Chair

Dr. Marc Moore

Dr. Chenkai Dai

ABSTRACT

The four heart valves (HVs) regulate the unidirectional flow of blood throughout the four chambers of the heart. The artioventricular heart valves (AHVs) enforce this unidirectional flow between each atrium and the respective ventricle, while the semilunar heart valves (SHVs) governs the flow of blood from the ventricles into the major arteries. The ability to maintain this one directional flow during the cardiac cycle is governed by the collagenous leaflets (or cusps) that prevent retrograde blood flow. Dysfunction of the leaflet microstructure (e.g., stenosis) or failure of sub-valvular components can affect the mechanical properties of these tissues, negating complete coaptation and resulting in *valvular regurgitation*. Clinical therapeutics for heart valve regurgitation vary from native valve repair to implementation of mechanical or bioprosthetic heart valve, both of which exhibit limitations for long-term prevention of regurgitation. Understanding the relationship between the collagen microstructure and tissue mechanics of these heart valve leaflets will not only elucidate the underlying pathology, but also provide the constitutive relations necessary to inform multiscale computational models for improving the treatment of HV disease. To further examine the microstructural and mechanical properties of the HV leaflets, this thesis research employed a polarization-based opto-mechanical system, capable of quantifying the realignment and reorientation of the tissue's underlying collagen fiber architecture (CFA) when subjected to varying biaxial mechanical loads. Biaxial testing revealed a J-shaped stress-strain relationship for all HV leaflets, with greater extensibility in the tissue's radial direction than the circumferential direction under all biaxial testing protocols. We also observed the SHVs to be more extensible than the AHVs in the radial direction, and variations in the mechanical response contingent on anatomical position (i.e., left/right side of heart). For example, the tricuspid and pulmonary valve leaflets were more extensible in the radial direction than their left heart counterparts, the mitral and aortic valve. Our collagen microstructure quantifications showed a loading-dependent and spatially-varied CFA for all HV leaflets. Further, under equibiaxial loading, the collagen fibers were better aligned and were preferentially oriented towards the circumferential axis. Under non-equibiaxial loading, however, the CFA displayed reorientation towards the direction of

the greatest applied loading. The AHVs exhibited the greatest collagen fiber alignment under increased loading, while the SHVs were more susceptible to CFA reorientation, pointing towards the variations in physiological loading environment. Findings for the four HVs provide a microstructural basis for the observed mechanical behavior, and elucidate the differences in anatomical position and function. In summary, these investigations further elucidate the microstructure-mechanical relationship in HV leaflets, which is essential for developing multiscale models and refining clinical therapeutics.

ACKNOWLEDGMENTS

First, I would like to thank my advisor, Dr. Chung-Hao Lee, for his continued support throughout the last three years of research in the BBDL. Your mentorship and investment towards my career has helped me develop throughout my research journey and discover my true passions. To my committee members, Dr. Moore and Dr. Dai, your guidance and passion for research has been integral to my development and career path, I am thankful for your support throughout this process. I also would like to thank my colleagues in the BBDL, it has been a pleasure working with such intelligent individuals who have pushed me to challenge my own limitations. Devin, Colton, and Sergio - thank you for your insight and friendship during my time in the BBDL, and for contributing to my decision on pursuing graduate school. Next, I want to thank my family for their love and support throughout the ups and downs during my time at OU, I could not have accomplished my goals without you all. Thank you to all those that have stood by my side during my time OU, and many others that have invested in me throughout this journey. I would like to dedicate this thesis to Grayson Danner, you were a true friend to the fullest extent of the word, and I will carry you with me in all that I do.

TABLE OF CONTENTS

LIST OF FIGURES

LIST OF TABLES

1 INTRODUCTION

1.1 Motivation

The four heart valves (HVs) regulate the unidirectional flow of blood throughout the four chambers of the heart. More specifically, the artioventricular heart valves (AHVs) enforce this unidirectional flow between each atrium and the respective ventricle, while the semilunar heart valves (SHVs) governs the flow of blood from the ventricles into the arteries. The ability to maintain this one-way flow during the cardiac cycles is facilitated by the valve's leaflets (or cusps) that prevent a retrograde of blood from flowing backwards. In the case of valvular heart disease (VHD), the structural barrier created by these valve leaflets becomes compromised, causing a regurgitant jet of blood to flow. This valvular insufficiency can lead to an increased blood volume, pressure, and the inability to provide a sufficient amount of blood to other organ systems leading to heart failure. Current therapeutic techniques are largely limited by the diverse variations in a patient's specific valve morphology, the sub-valvular component geometries, and the severity of the disease being treated. Due to these limitations, the therapeutics utilized vary widely in efficacy, and commonly require invasive surgical procedures, re-operation on the previously treated valve, or even life long anti-coagulation medications to supplement the side effects of the surgery.

Given the fallibility of these surgical procedures, considerable efforts have been made within the field of cardiovascular biomechanics that seek to improve the outcome of these operations for VHD. The implementation of patient-specific computational models and numerical studies involving *in-silico* realization have been of increased interest for use in the clinical setting. The finite element-based patient-specific models could enable healthcare practitioners and surgeons to diagnose the valve abnormalities, plan surgical operations, and evaluate the therapeutics tailored to the patient's cardiovascular geometry. The versatility of these patient-specific models are highlighted by the ability to capture each patient's geometry in real time during the cardiac cycle using three-dimensional echocardiographic (3DE) imaging, or other medical imaging modalities. These high-fidelity models, although promising in terms of capturing the patient's

valvular hemodynamics and geometry, rely heavily on the implementation of mechanical and microstructural constitutive models that can accurately capture the behaviors of valvular leaflet tissues.

Tissue-engineered heart valves (TEHV) have been proposed as a unique therapeutic alternative that mitigates the use of mechanical prosthetic heart valves, which require life-long anti-coagulation medication. The process of manufacturing a TEHV construct begins with a decellularized extracellular matrix or biodegradable polymer and seeding the cells into the acellular scaffold, where the underlying microstructure is developed. These laboratory-derived heart valves, which are capable of developing with the patient, are of particular interest owing to their large implications for congenital heart diseases, commonly requiring multiple surgeries throughout a lifetime. Although pre-clinical studies have shown the exceptional efficacy in developing these TEHVs, there exists large disparities in the appropriate scaffolding material used to mimic the *in vivo* function of the native valve leaflet. Currently, cultivating a scaffold material that mimics the microstructural and mechanical properties of a native valve has been prolonged by the inability to examine the load-dependent nature of the collagen microstructure—a limitation of many existing collagen imaging techniques. Bridging this gap for both the native valvular structures and the TEHV scaffolds will lead to refined, biomimetic materials capable of matching the *in vivo* valve function.

Despite the significant improvement for both patient-specific models and TEHV in treating VHD, these potential therapeutics are limited by the current understanding of the tissue-level mechanical properties of the native valve and the microstructural changes in response to mechanical loads. Specifically, previous studies that have aimed to elucidate this relationship rely on the use of *destructive* optical techniques or micron-level field of view (FOV), negating the ability to observe the tissue-level microstructural-mechanical relationship within the *same specimen*. Observing this essential biomechanical relation non-destructively can further inform current mechanical and fiber-based constitutive models, leading to refined computational modeling tools and TEHV structures.

1.2 Objective and Scope

The first objective of this M.S. thesis is to establish a novel integrated experimental approach to understand the microstructural-mechanical relationship in cardiovascular valve tissues. The execution of this objective is fulfilled by characterizing the biaxial mechanical properties, collagen fiber architecture (CFA, *i.e.*, fiber orientation and alignment), and microscopic composition of the tricuspid valve (TV) leaflets. The leaflet-specific quantification will, *for the first time*, elucidate the CFA's reorientation and realignment with respect to equibiaxial and non-equibiaxial loading states. The implementation of these experimental protocols will provide a systematic way to non-destructively understand the microstructural basis for the observed tissue biomechanics at the bulk-tissue scale. Additionally, we seek to observe the intrinsic properties for each TV leaflet at the unloaded state, and the regional microstructural realignment and reorientation that occur under physiologically-relevant loads. This thorough analysis pipeline will enable future development of constitutive relations into computational models that better mimic the native organ-level function.

Extending upon this tissue characterization pipeline, the next objective is to provide a holistic examination of the biomechanical and microstructural properties of the other cardiac valves, namely the mitral valve (MV), the aortic valve (AV), and the pulmonary valve (PV). The mechanical properties of these valves have been sufficiently investigated; however, we lack the knowledge of the *load-dependent collagen fiber microstructure* of the leaflet tissues and their connection to the mechanical behaviors of the tissues.Specifically, each valve leaflet (or cusp) is subjected to physiologically-relevant equibaixial and non-equibiaxial loads, and the collagen fiber architecture changes are quantified. In addition, the incremental microstructural changes prior to peak equibiaxial loading are also investigated and the mechanical testing metrics (i.e., modulus, extensibility) extracted. Improving the understanding of all four HVs in combination will explicate the role of the collagen fiber microstructure in the tissue's mechanical beahviors and allow comparisons to be made between the AHVs and the SHVs.

The remainder of this thesis is organized as follows. In Chapter 2, the anatomy, function, and microstructure of heart valves are briefly introduced, together with a literature review of VHD, mechanical characterizations, and collagen microstructural quantification. Chapter 3 discusses the baseline mechanical and load-dependent microstructural

quantification of the TV leaflet tissues and the implementation of our integrated experimental approach. To expand upon these baseline investigations for the TV, Chapter 4 presents the mechanical-microstructural quantification of the MV leaflet tissues, followed by the characterizations for the two SHVs in Chapter. Finally, Chapter 6 provides a comparison between the AHVs and the SHVs, followed by the concluding remarks of the key findings of this thesis research and potential future extensions based upon the research work in this thesis.

2 LITERATURE REVIEW

2.1 Heart Valve Function

The four heart valves (HVs) regulate the unidirectional blood flow between the chambers of the heart (Fig. 2.1). When the deoxygenated blood enters the right side of the heart, it passes through the tricuspid valve (TV) and the pulmonary valves (PV) prior to its entrance into the lungs for oxygen exchange. Once re-oxygenated, the blood re-enters the left side of the heart, passing through the mitral valve (MV) and the aortic valve (AV) through the aorta to supply oxygenated blood to the body.

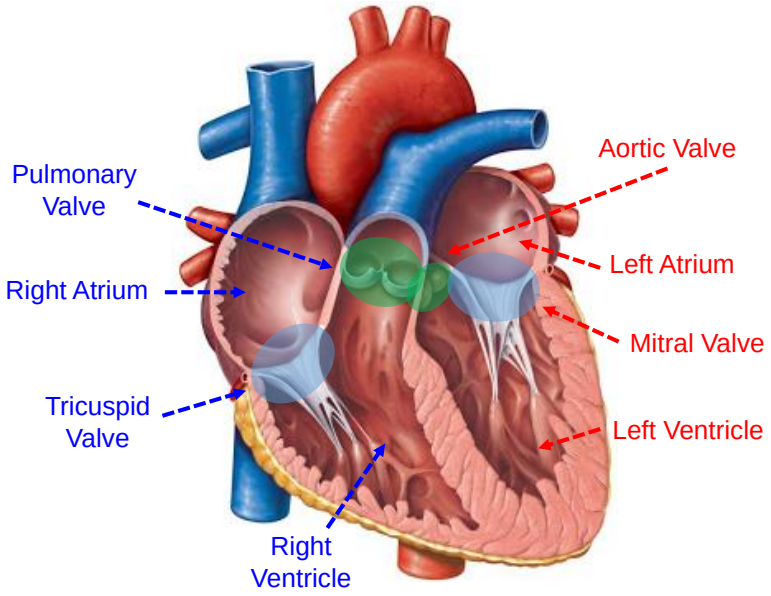

FIGURE 2.1 Schematic of the heart valve anatomy (image adopted from Biology Corner).

These heart valves can be classified into two distinct categories dependent on their morphology and anatomical position within the heart: (i) the atrioventricular heart valves (AHVs, the MV and the TV), located between the atrium and the corresponding ventricle; and (ii) the semilunar heart valves (SHVs, the AV and PV), categorized based on their semilunar (half-moon) geometry. In the two SHVs, the pulmonary valve opens and coapts subject to the pressure gradient between the right ventricle and the pulmonary artery, directing the deoxygenated blood. Similarly, the aortic valve directs the

oxygenated blood from the left ventricle through the same mechanism to the aorta. In contrast, the AHVs serve as an analogous role, regulating the unidirectional flow of blood from each atrium to the ventricle. Although the semilunar and atrioventricular valves share a common role in the overall cardiovascular function, there are unique differences in their sub-valvular components and physiological loading environment, resulting in the variations in their morphology, microstructure, and tissue-level mechanical behaviors.

2.2 Anatomy and Function of the Atrioventricular Heart Valves

The AHVs regulate the unidirectional flow of blood via the cyclic opening and closing of the valve leaflets (Fig. 2.2). The MV, also known as a bicuspid valve, is composed of two leaflets, namely the MV anterior leaflet (MVAL) and the MV posterior leaflet (MVPL), whereas the TV, although similar in function, consists of three leaflets: the TV anterior leaflet (TVAL), TV posterior leaflet (TVPL), and the TV septal leaflet (TVSL). These AHV leaflets are primarily asymmetric in shape and show wide variations in their morphological structure, introducing complexity and difficulty in making current surgical methodologies and procedures *personalized* [1, 2].

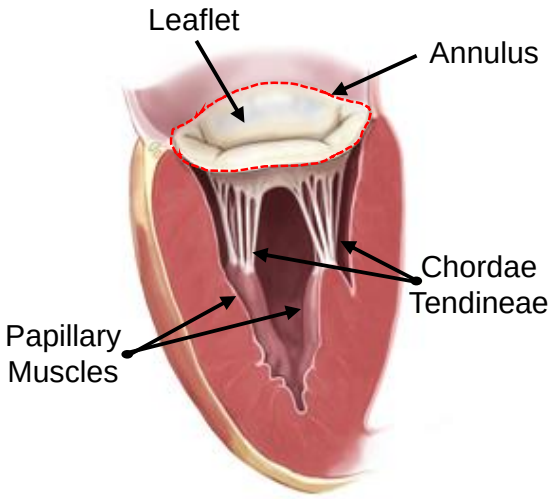

FIGURE 2.2 AHV anatomical structure and sub-valvular components (image adopted from Science Source).

The AHV leaflets are supported by the valve *annuli*, a fibrous-muscular ring that segregates the atria and the ventricle and connects the valve leaflets to the heart chambers (Fig. 2.2). Located distally from the *annulus* attachment at the free edge are the chordae tendineae (CT). During systole, the ventricles on each side of the heart will contract, allowing for the leaflets to coapt, and prevent the retrograde flow of blood into the atria. During this phase of the cardiac cycle, the AHV leaflets are subjected to the systolic pressure gradient that will be transferred to the chordae tendineae (CT) and the papillary muscles. Proper valve function is facilitated by the integrity and robust function of these sub-valvular components, which may be altered over the life cycle due to aging or diseases [3–5].

2.3 Anatomy and Function of the Semilunar Heart Valves

In the two SHVs, the AV is attached at the aortic root, separating the left ventricle and the aorta, and is composed of three scallop-shaped cusps: the aortic valve right coronary cusp (AV-RCC), aortic valve left coronary cusp (AV-LCC), and the aortic valve non-coronary cusp (AV-NCC). The PV, on the other hand, is complex in anatomical structure, consisting of the pulmonary valve anterior cusp (PV-AC), pulmonary valve left cusp (PV-LC), and the pulmonary valve right cusp (PV-RC) attached at the trunk of pulmonary artery (Fig. 2.3).

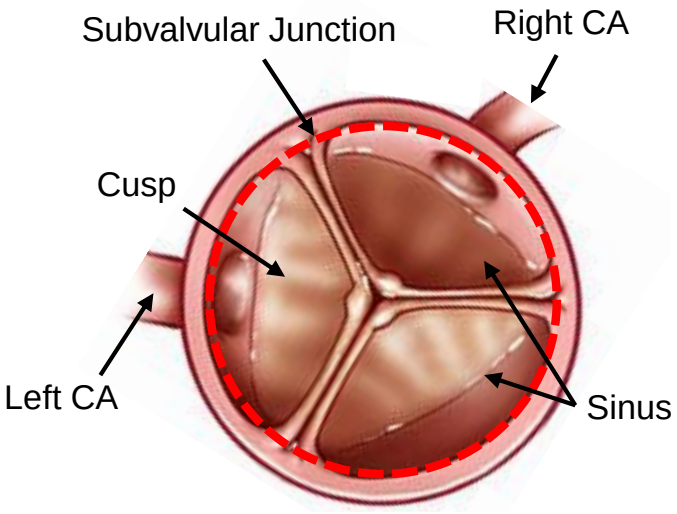

FIGURE 2.3 SHV anatomy and valvular components – subvalvular junction, sinus, and cusps (image adopted from Hispanic Heart Center).

These SHVs cusps follow a semilunar shape with a basal attachment to the walls of the outflow vessel at the subvalvular junction, creating a pockets behind the cusps denoted as sinuses (Fig. 2.3). The SHVs are subjected to a pressure gradient during diastole that is counteracted by the flow of blood within these sinuses, reducing the mechanical stress on the cusps by creating fluid currents and eddies between the vessel wall and the cusp, ultimately closing the valve [6, 7]. The anatomical structure and hemodynamics of the AV and the PV differ greatly from those of the AHVs leaflets, primarily due to the differences in the sub-valvular structures and the mechanistic and functional role that prevents blood regurgitation.

2.4 Microstructure of the Heart Valve Leaflets

The AHV leaflets and SHV cusps have a complex, layered microstructure that is composed of various constituents that each play a unique role in proper valve mechanics and function. Collagen fibers, elastin fibers, proteoglycans (PGs), and glycosaminoglycans (GAGs) are found in varying densities throughout each layer, providing morphological function transmurally throughout the tissue. Another key component within these valve structures are valve interstitial cells (VICs), which contribute to the growth and remodeling of tissue's extracellular matrix (ECM) in response to changes in the overall mechanical environment.

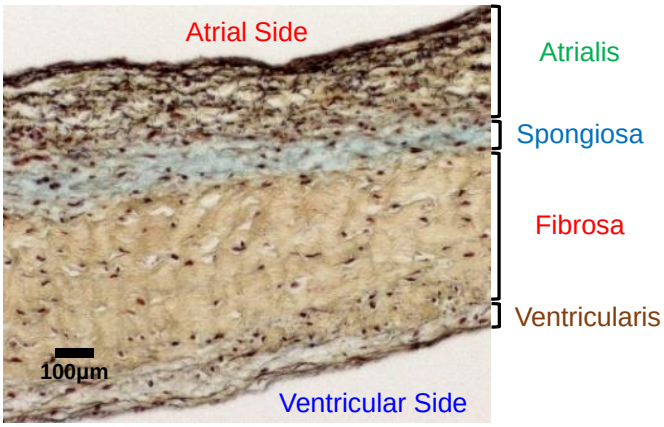

FIGURE 2.4 Microscope images taken of a TVAL stained by Movat's Pentachrome to capture VICs, elastin fibers (black), GAGs and PGs (blue), and collagen fibers (yellow) throughout the thickness (image adopted from [8]).

The microstructure of the AHV leaflets can be morphologically categorized into four distinct layers, as described from the atrial to the ventricular surfaces [9–11]: (i) the atrialis, composed primarily of radially-oriented elastin fibers that provide the tissues' low-stress elasticity; (ii) the spongiosa, containing non-fibrous components, such as glycosaminoglycans (GAGs) and proteoglycans (PGs), that act as a dampening mechanism during rapid leaflet bending; (iii) the collagen-rich fibrosa, the primary load bearing layer; and (iv) the ventricularis, which is composed of colagen and circumferentially-oriented elastin fibers that facilitate movement and restore the leaflets to their undeformed geometries during valve opening (Fig. 2.4).

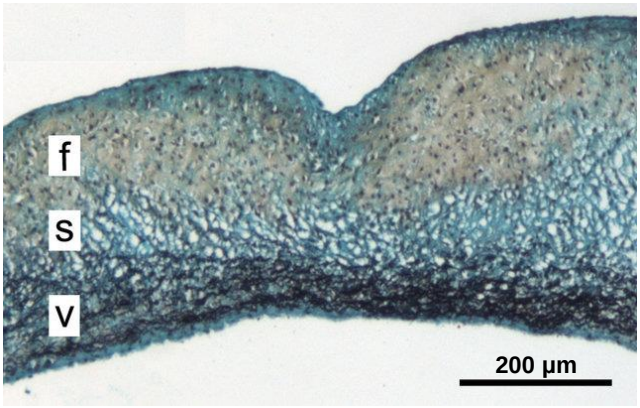

FIGURE 2.5 Microscope images taken of a AV cusp stained by Movat's Pentachrome to capture elastin fibers (black), GAGs and PGs (blue), and collagen fibers (yellow) throughout the thickness (image adopted from [12]).

In contrast, the AV and PV cusps follow similar morphological composition from the arterial to the ventricular surface, consisting three layers [12–16] : the (i) fibrosa, that contains load-bearing collagen fibers of the tissue; (ii) spongiosa, comprised of primarily GAGs; and the (iii) ventricularis, which is composed of elastin and collagen fiber networks that an exert a compressive force on the fibrosa, keeping the collagen fibers in an undulated formation under low forces (Fig. 2.5). Despite the functions provided by the other microstructure layers, the fibrosa layer is of primary focus due to its relationship to the tissue's load-bearing capacity [16, 17].

2.5 Heart Valve Disease and Current Treatment Options

Heart valve disease contains a broad spectrum of pathologies that can be detrimental to valvular function. Valvular regurgitation has proved to be the most common form cardiovascular related disease, with TV and AV regurgitation affecting 1.5-1.6 million Americans each year, and 7.8 million affected by MV regurgitation alone [18–20]. This disease is typically categorized into two distinct sub-classes, depending on the mechanism of action: (i) primary and (ii) secondary regurgitation. Primary regurgitation occurs when there is direct alterations to the valvular structure, such as chrodae tendineae tethering, preventing the valve from fully closing and allowing retrograde blood flow (Fig. 2.6) [21, 22]. Because of the calcification of the leaflets, valvular stenosis is also commonly associated with primary regurgitation, causing the leaflets to lose mobility and deformability under load. This pathology is of particular interest for the SHVs, due to its association with congenital patients and the lack of sub-valvular structures to facilitate the opening/closing of the leaflets [23–26].

Regardless of structural health, secondary regurgitation can still occur due to alterations in the sub-valvular structures that aid in cardiovascular function. In AHVs, pulmonary hypertension and right ventricular enlargement can result in annular dilation or the loss of the intrinsic saddle shape of the annulus, expanding the coaptation area (i.e., circumference on the annulus) needed to prevent regurgitant blood flow [27–29]. Likewise, pressure or volume-overload can produce dilation in the aortic and pulmonary roots, mimicking the same effect for the SHVs (Fig. 2.6) [30, 31]. Currently, there are several clinical remedies available to address the complex nature of valvuluar regurgitation, according to the severity of the disease and the patient's anatomical features. For secondary valve regurgitation, one of the most notable devices is the annuloplasty ring, which is sutured to the annulus to restore the complete leaflet coaptation and downsize the dilated annulus. This reduction in the circumference of the annulus restores coaptation to the leaflets, preventing further regurgitation within the patient. In repairing the AHVs, a single annuloplasty ring is typically sutured to the deformed geometry, whereas the SHVs require more complicated procedures to restrict the annulus of the artery at the sub- and supravalvular levels [32]. Although this device provides initial alleviation, recurrence is common in patients treated for MV (20%) and TV regurgitation (16-18%) within 5 years post-operation [33–35]. Greater success has been seen

in repairing SHVs with annuloplasty rings, yielding a 97% freedom from re-intervention, which is especially critical for older patients to reduce multiple invasive procedures [32, 36].

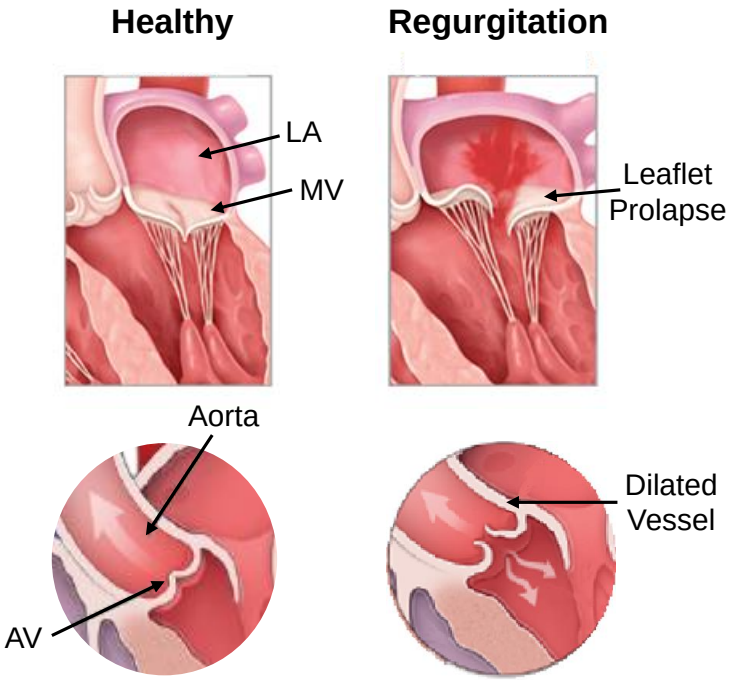

FIGURE 2.6 Schematic comparing healthy versus regurgitant flow in the AHVs and SHVs (imaged adopted from Temple Health)

In contrast, primary valve regurgitation commonly illicits direct clinical interaction with the sub-valvular features, such as leaflet re-sectioning after prolapse and neochordae implementation to replace the tethered structures [37–40]. In stenotic valves; however, complete valve replacement is typically pursued due the degradation and calcification of the underlying tissue microstructure. Mechanical heart valves have been essential in addressing valvular stenosis, providing long-term durability upon replacement, but require life-long anti-coagulants that increase the risk of haemorrhaging [41–43]. Xenogeneic bioprosthetic valves manufactured from de-cellularized animal models (i.e., bovine pericardium, porcine aortic valve) can eliminate the need for anti-coagulants, but show signs of substantial calcification and degradation within 10-20 years [44]. More importantly, these procedure may not be ideal for congenital patients, as the valvular geometry will change throughout development. Recent advancements in tissue-

engineered heart valves (TEHVs) have addressed these shortcomings in congenital procedures, allowing for growth and remodeling potential *in vivo* after implementation. TEHVs are still in development, with improvements focused on microstructural growth potential and valvular calcification prior to wide-spread clinical use [45]. Although current clinical therapeutics have displayed a promising trend in treating valvular heart disease, there exist a large variety of limitations that lead to surgical re-intervention after repair or replacement. To improve the surgical outcomes and efficacy of current treatments, significant efforts have been placed on examining the tissue-level mechanics and microstructure of the four heart valve leaflets.

2.6 Mechanical Characterizations of the HV Leaflets/Cusps

The first mechanical observations of the mitral valve (MV) leaflets were reported by May-Newman *et al.* [46], providing a foundational step in characterizing HV leaflet behavior. Almost 20 years later, mechanical characterizations of the TV leaflets were first provided by Heyden *et al.* [47], where they provided a survey of the mechanical properties for the leaflet tissues from all four cardiac heart valves.

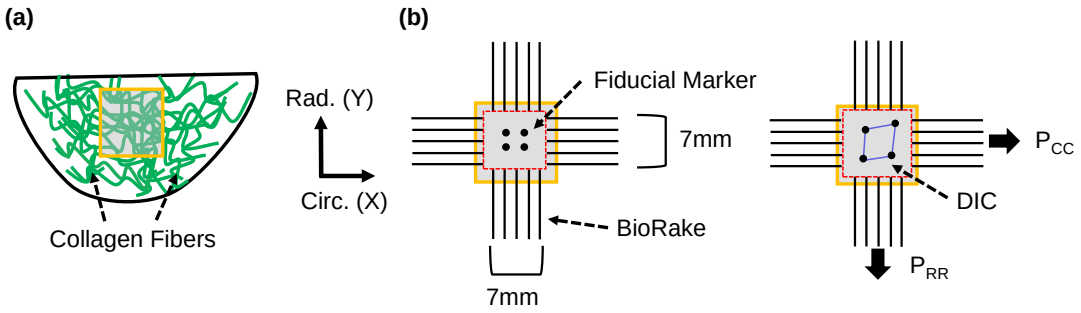

FIGURE 2.7 Tine-based biaxial testing procedures used in our lab to characterize the tissue-mechanics of HV leaflets: (a) the belly region of each leaflet is extracted and (b) mounted to a biaxial testing device where fiducial markers are applied to capture the in-plane strain via data image correlation (DIC).

These seminal studies captured the leaflet tissue's repeatable cyclic mechanical response after preconditioning, restoring each specimen to its *in vivo* configuration, as commonly used in other soft tissue biomechanical testing. Subsequent investigations have refined these fundamental procedures by performing biaxial testing on the central,

belly portion of the leaflets and utilizing various loading ratios of targeted stress values in the tissue's circumferential (C) and radial (R) directions to capture the complex tissue-level mechanical response (Fig. 2.7).

Several key findings regarding the biaxial mechanical properties of the AHV leaflets can be summarized as follows. First, the AHV leaflets exhibited material anisotropy under biaxial tension, yielding a J-shaped stress-strain curve consisting of three main regions in both tissue directions (Fig. 2.8): (i) a near-linear toe region with extensive leaflet deformation; (2) a highly nonlinear transition region displaying rapid increase in leaflet stiffness; and a (3) second linear region as peak target stress is reached. Moreover, the MV and TV leaflets showed greater extensibility in the tissue's radial direction compared to the circumferential direction under all loading protocols with distinct mechanical directional coupling [48–51]. Second, the mechanical properties are distinct to each AHV leaflet, with the MVPL showing greater extensibility and anisotropy when compared to its MVAL counterpart [10]. Similar observations were made for the three TV leaflets by Meador and Pham *et al.*, where the TVPL yielded greater material anisotropy compared to the TVSL and TVAL under equibiaxial load (Fig. 2.8) [52, 53]. Third, the AHVs exhibit a loading-rate dependent mechanical behavior, with slight decreases in peak tissue stretch as equibiaxial loading-rate increased [10, 54]. Finally, a time-dependent, stress-relaxation behavior was found for all AHV leaflets, although these quantifications are outside the scope of this current work [55, 56].

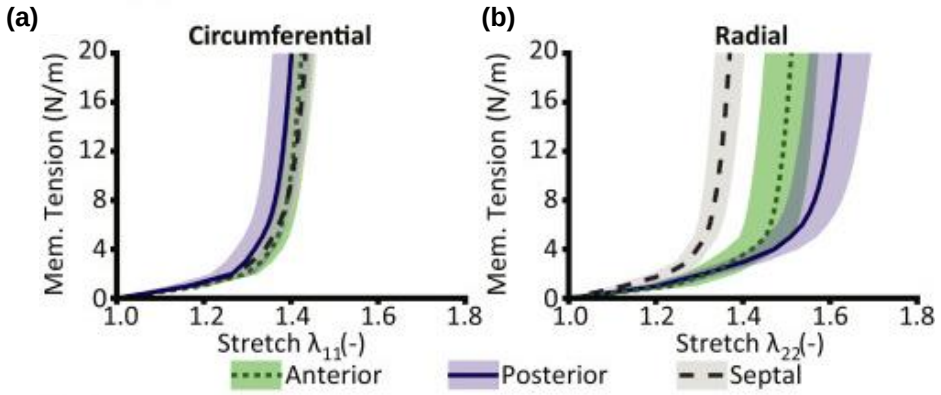

FIGURE 2.8 Biaxial testing results for the three TV leaflets in the (a) circumferential and (b) radial tissue directions (images modified from [52]).

Similar mechanical quantification have been made for the SHVs, although significantly more effort has been placed on the characterizing the AV cusps compared to its right heart counterpart. Overall, an analogous anisotropic, stress-strain responses was observed under equibiaxial mechanical loading for both the AV and PV cusps [15, 57–61]. For the same studies, greater extensibility in the tissue's radial direction was also observed for each specimen, pointing towards similarities in the tissue-level mechanical response between the AHVs and the SHVs [15, 57–59]. Huang *et al.* provided the first mechanical comparisons between the AV and PV cups, demonstrating a more anisotropic material behavior in the PV compared to the AV [57]. Furthermore, Billiar *et al.* revealed that varying biaxial loading protocols showed a distinct non-monotonic relationship between circumferential stress and strain for AV cusps, although the same behavior has yet to be observed for the PV (Fig. 2.9) [61].

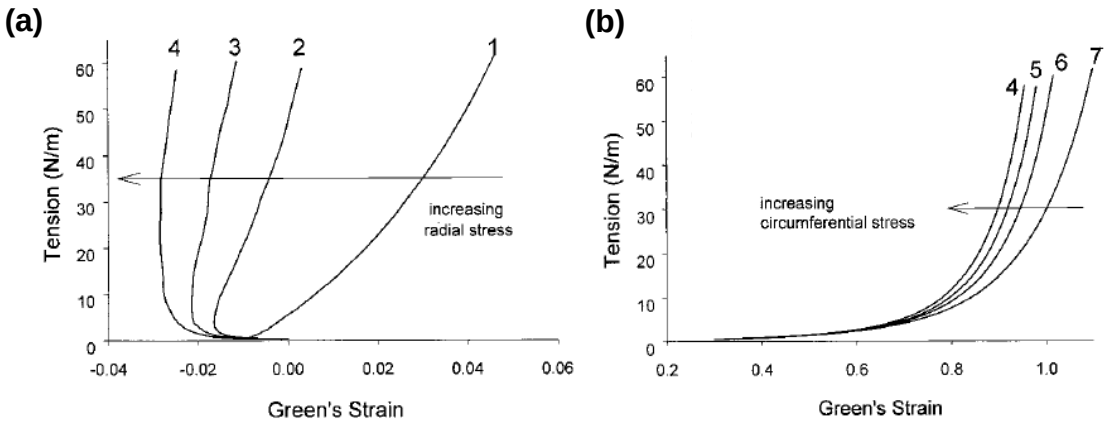

FIGURE 2.9 Biaxial testing results for glutraldehyde treated AV cusps under varying physiologically-relevant loads, exhibiting directional coupling between the (a) circumferential and (b) radial tissue directions (image adapted from [61]).

In more recent years, mechanical investigations have been geared towards the loading-rate dependency and stress-relation of the underlying tissue microstructure within the SHVs. For example, Anssari-Benam *et al.* observed a intrinsic stiffening behavior under increased biaxial stretch rate for the AV and PV cusps [62, 63], elucidating the importance of loading rate in the development of appropriate mechanical testing protocols. Likewise, stress-relaxation was present in both SHVs, although greater focus has been placed on the AV due to its clinical relevance and association with heart valve disease [64, 65]. Despite these standard mechanical observations, comparisons

have yet to be made between individual mechanical properties for both the AV and PV, leading to simplistic generalizations in literature between each cusp's structure-function relationship.

The observed anisotropic, non-linear mechanical responses seen in the four HV leaflets stems from the underlying collagen fiber architecture that governs the tissue's adaptation to load. As previously mentioned, the collagen fibers exhibit an undulated, "crimped" formation before progressive straightening occurs under low applied stress. Following the uncrimping of these fibers, the collagen fiber architecture is recruited and reorients to compensate for greater physiological stresses in the different tissue directions [66]. Due to the crimped nature of these fibers, the collagen fiber architecture does not initially contribute to the tissue-level mechanics, resulting large deformations under low stress in the toe region of the stress-strain curve. After further straightening, the rigidity of the tissue results in greater stiffness and non-linearity, owing to the dynamic nature of the collagen fiber architecture. Although this phenomena has been observed in the mechanical responses of the HV leaflets, there is a need for understanding the inter-relationship between the tissue-level mechanics and the load-dependent collagen fiber architecture.

2.7 Microstructural Characterizations of the HV Leaflets/Cusps

Collagen is the most abundant protein in the human body (25-30% of all protein), characterized into eight collagen types contingent on their biochemical structure [67, 68]. Collagen types I and III are the primary proteins found in heart valve leaflets, forming fibers (1-10 μm) that develop complex networks throughout the tissue domain. These networks exhibit dynamic behavior in response to physiological load, providing structural integrity and leaflet mechanical strength. Intrinsic to heart valve leaflets, collagen fibers also exhibit a highly-crimped configuration that straightens under applied load, which is essential to its tissue-level mechanical contributions [49]. A variety of collagen microstructural imaging techniques have been employed to investigate the underlying collagen-dominant microstrucure in heart valve leaflets. These techniques employ different mechanisms to enhance image contrast and identify the underlying fiber structures, but have different primary uses based on the desired resolution and field of view (FOV). The most common modalities can be categorized into two distinct families: (i)

contemporary techniques, that exhibit high resolution and precise sectioning capabilities: and (ii) structural quantification techniques, which can provide high contrast localized fiber orientation quantifications. Second harmonic generation (SHG) is one of the most widely accepted contemporary techniques used to observe the CFA.

SHG relies on nonlinear photon absorption/emission by fluorophores within the tissue, exhibiting different excitation wavelengths that are dependent on the molecule. This is especially useful in identifying collagen and elastin within tissue structures, due to their intrinsic contrast mechanisms. Second harmonic imaging has been used to investigate the uncrimping and preferred circumferential direction of collagen fibers in the MVAL leaflets (Fig. 2.10) [69–71], with similar applications in more recent years towards the TV leaflets [51, 52]. From these observations, the straightening and recruitment of collagen fibers was seen under applied mechanical load, with a preferred collagen fiber direction in the circumferential direction for all AHV leaflets. SHG has also provided a means to identify calcification and disease dependent variations in the collagen structure for congenital patients with AV or PV dysfunction [72–74], although the native structure of the valves has yet to be examined through this modality.

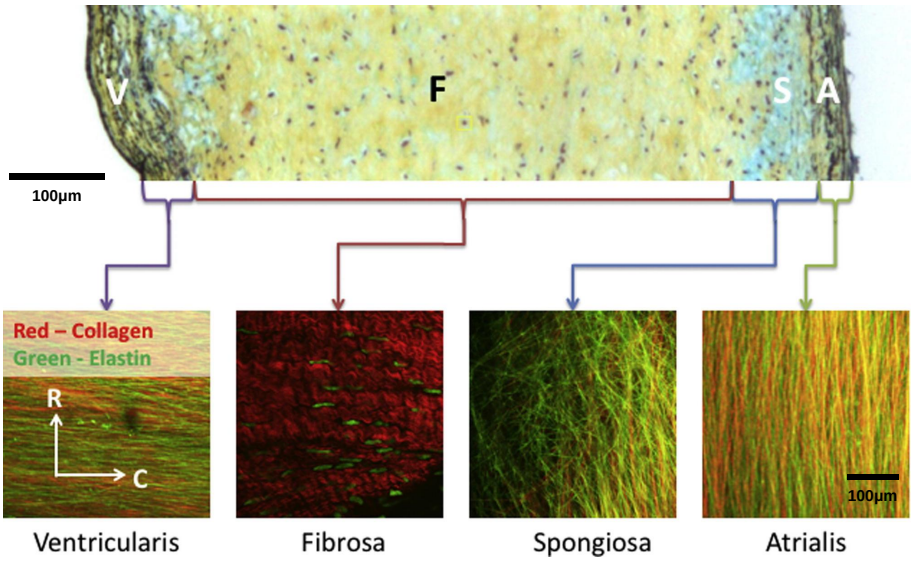

FIGURE 2.10 Second harmonic generation (SHG) images of the MV anterior leaflet stained with Movat's Pentachrome to identify the collagen (red) and elastin (green) fiber orientations in each layer. (Image adopted from [71])

Confocal laser-scanning microscopy (CLSM) is another conventional way to examine the microstructural constituents, capturing variations in refractive index or absorption through laser scanning. This approach allows for μm resolution in both the spatial and transmural directions, building high-fidelity resolution images of the leaflet microstructure [75–79]. Previous studies using CLSM have observed a circumferentially oriented microstructure in heart valve leaflets, although the extent of these observations is limited to the intrinsic properties of the specimens. These conventional modalities have provided a foundational understand of the collagen fiber architecture, but are largely limited by their increased resolution and lengthy data acquisition time which may not be ideal for performing bulk-tissue characterizations.

Structural quantification techniques rely predominantly on the birefringent and anisotropic light scattering properties exhibited by collagen fibers. Collagen fibers in particular display polarization dependent scattering, in which the back scattered intensity response is dependent on the in-plane light's polarization angle and the orientation of the fiber [80]. In short, these fibers transmit light preferentially along their axis of alignment. Polarized light microscopy (PLM) leverages the birefringence of the collagen fiber, quantifying the fiber structure over a large FOV. PLM has been used to distinguish the CFA from other constituents in HV leaflets, providing a method to quantify collagen fiber crimp across the entire specimen [16, 81–83]. However, PLM requires alterations to be made to the tissue, either through tissue sectioning or the use of optical clearing and staining solutions, which prohibits the evaluation of the functional load-dependent CFA.

These optical methods are commonly used in conjunction with small angle light scattering (SALS), allowing for collagen fiber orientation, alignment, and angular distribution to be extracted spatially across the sample. SALS uses laser transmission to capture the scattered and transmitted light profiles, where the subsequent scattered light angle can be attributed to the orientation of the collagen fiber structures [80]. In the last 20 years, SALS has been essential to understanding the role of the collagen-dominant microstructure in HV leaflets [49, 84–87], leading to significant advancements in structural constitutive models and computational simulations [88–90]. Recent studies have investigated the effects of pressure loading on HV leaflets, quantifying the changes in collagen fiber orientation and alignment (Fig. 2.11) [85–87]. Changes in the microstructure were captured by chemically fixing the cusps at specified loads using a glutraldehyde

solution, then performing SALS imaging across the fixed specimen. Under the applied loading, the AV and PV cusps presented a predominantly circumferential orientation and became more aligned throughout the tissue with increasing pressure (Fig. 2.11) [85, 87]. Although the SALS methodology provides an avenue to link the collagen microstructure to the tissue-level mechanics, the chemical treatment required inhibits the observation of the *same specimen* under varying mechanical loading protocols. Further, this technique is unable to resolve information transmurally through the sample, making layer-specific quantification unobtainable.

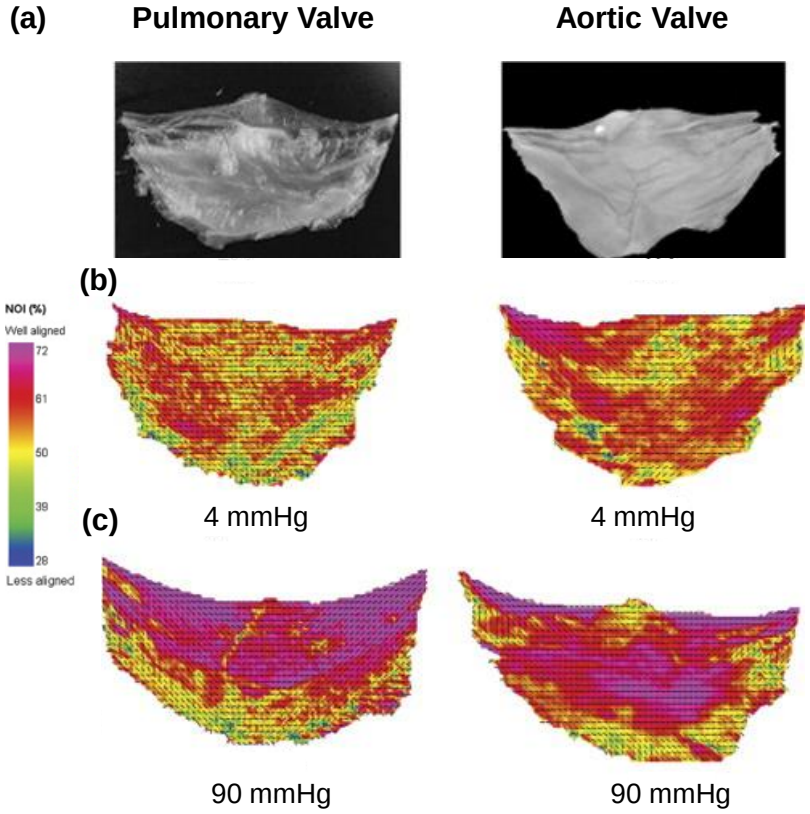

FIGURE 2.11 Quantifications of collagen fiber preferred orientation (dashed lines: –) and degree of local fiber alignment (colorbar) for the pulmonary and aortic valve leaflets: (a) raw images of the leaflets, (b) the collagen fiber architecture at a 4 mmHg pre-load, and (c) the fiber architecture under 90 mmHg transvalvular fixation pressure. (Images modified from [85]).

To addresses these limitations, polarized spatial frequency domain imaging (pSDFI), a recently developed optical imaging technique, has been used to observe the CFA of HV tissues on a millimeter-scale FOV, while removing the need for fixative solutions

[91, 92]. Using a combination of polarized light and spatial frequency domain imaging (SFDI), the birefringent response of the collagen fibers is captured as a function of modulated tissue depth contingent on the spatial frequency pattern applied. Goth *et al.* was the first to use this optical approach in AV cusps, finding distinct differences in collagen fiber orientation and alignment between the ventricularis and fibrosa tissue layers under zero force and zero deformation [92].

3 A PILOT STUDY ON LINKING TISSUE MECHANICS WITH LOAD-DEPENDENT COLLAGEN MICROSTRUCTURES IN PORCINE TRICUSPID VALVE LEAFLETS

3.1 Overview

In the previous literature, optical techniques, such as second harmonic generation (SHG) imaging [52, 93–95] and small-angle light scattering (SALS) [86] have been employed to provide valuable insight into the microstructure of the heart valve leaflets aas well as other soft tissues. However, these techniques are limited in their ability to capture the spatially varied, load-dependent collagen fiber architecture. For example, SHG has been used to obtain high-resolution images of the collagen fiber architecture of the mitral valve anterior leaflet at a biaxially-loaded state [69]. This investigation was limited to a ”micron-level” field of view (FOV), restricting the SHG modality to effectively examine the spatial variance in the collagen fiber architectures at a larger FOV. In contrast, the SALS modality can capture collagen fiber architectures of the entire tissue specimen, but this technique requires ”chemical fixation” due to lengthy imaging times (1-2 hours) [96, 97], limiting its capability to investigate the adaptive, load-dependent collagen fiber architectures (CFAs). To addresses these shortcomings, polarized spatial frequency domain imaging (pSDFI), a recently developed optical imaging technique, has been used to observe the CFA of the tissue on a millimeter-scale FOV, while removing the need for fixative solutions. Previously, Goth et al. [92] displayed the collagen microstructural quantification capabilities of pSFDI using ovine aortic heart valve leaflets at an unloaded state; however, they did not yet highlight the load-dependent architectural changes. Recently, our group has developed a combined instrument, which integrated an in-house pSFDI device with a commercial biaxial testing system, to investigate the load-dependent changes in the CFAs for bovine tendon tissues with highly-aligned CFAs and a representative porcine mitral valve anterior leaflet with more random CFAs [98].

The objective of this pilot study is to utilize the combined pSFDI and biaxial mechanical testing system to observe the load-dependent changes in the CFAs for three TV

leaflets from a representative porcine heart. This investigation will provide key insight into the microstructures and tissue-level mechanics of the TV, and aid in establishing a microstructure-mechanical pipeline for evaluating other HV soft tissue leaflets. The observed load-dependent changes in the CFAs at the microstructural level will aid in providing a better understanding of how the TV diseases influence the tissue mechanics and overall TV function, and in informing TV computational models for guiding clinical therapeutics such as feasibility or valve repair.

3.2 Methods

3.2.1 Porcine Heart Acquisition and Tissue Preparation

Three fresh, normal porcine hearts were obtained from a local USDA-approved abattoir (Country Home Meat Company, Edmond, OK), and dissected to retrieve the three TV leaflets (Fig. 3.1d): the anterior leaflet (TVAL), the posterior leaflet (TVPL), and the septal leaflet (TVSL) ($n = 3$ for each of the three TV leaflets). Excess chordae tissue was trimmed from the leaflets, and thickness measurements were made using a digital caliper (Westward Tools 1AAU4 – 0.01 mm resolution) at three different locations to determine an average leaflet thickness. Tissues were then stored in phosphate-buffered saline (PBS) at $4\,^\circ$ C prior to testing within 48 hrs.

3.2.2 Biaxial Mechanical Testing

The TV leaflet tissues were mounted to a commercial biaxial testing system (CellScale, Canada, 1.5 N load cells) using four BioRakes to facilitate a 10×10 mm effective testing region in the central portion of the leaflet specimens (Fig. 3.1b-c). During mounting, the tissues' circumferential (C) and radial (R) directions were aligned with the *X*- and *Y*-directions of the biaxial testing device. Following our previously developed displacement controlled protocols [9, 10, 50, 56] for investigating the atrioventricular heart valve tissue's nonlinear mechanical behaviors and material anisotropy, the specimen was next submerged in a PBS bath at $37\,^\circ$C for the entire duration of mechanical testing. Previous studies have highlighted that isotonic buffers, such as PBS, do not induce tissue swelling or affect the mechanical properties of the tissue compared other widely used buffer (e.g., DI water) [99]. A preconditioning protocol was utilized with six equib-

iaxial and non-equibiaxial loading/unloading cycles, targeting a membrane tension of 25 N/m to restore the leaflets to their in-vivo physiological configurations [46, 48]. After preconditioning, the tissues were subjected to displacement-controlled biaxial testing experiments, emulating biaxial tensions (T) at varying loading ratios (T_{C}:T_{R}=1:1, 1:0.5, 0.5:1, and 2:2) to capture a broad range of potential physiological deformation states [10, 51, 53]. These biaxial tension protocols were each applied for three loading/unloading cycles, and the forces and displacements were recorded at 5 Hz. The membrane tension-stretch data was extracted from the third loading cycle. Note that the membrane tension was computed from the recorded force divided by the effective edge length (10 N), and the tissue stretch (λ) was calculated using $d_{tine}^{load}/d_{tine}^{PPC}$ for both the circumferential and radial directions, where d_{tine}^{PPC} is the tine distance after preconditioning, and d_{tine}^{load} is the tine distance at the loading state.

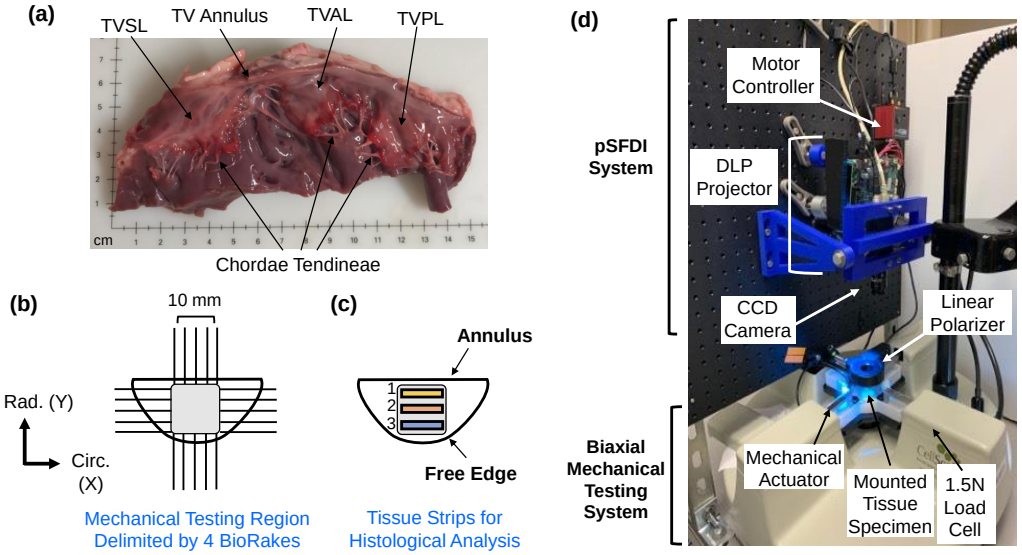

FIGURE 3.1 (a) The porcine TV was dissected to retrieve the three TV leaflets for use in (b) biaxial mechanical testing. (c) TV leaflet strips from the effective testing region were used for histological analyses. (d) A side view of the combined pSFDI-biaxial testing system, displaying optical components, mounted tissue specimen, and mechanical testing components.

3.2.3 pSFDI-Based Collagen Microstructure Quantifications

Following mechanical testing, the pSFDI system was integrated with the biaxial mechanical tester by vertical placement above the testing sample (Fig. 3.1b). Following

the procedure of pSFDI-based collagen fiber quantifications, the incident spatial frequency light patterns were produced from an LED projector (Texas Instruments, Dallas, TX) with a wavelength of 490 nm (cyan). A 5-megapixel CCD camera (Basler, Germany) was used to capture the reflected light intensity responses through a rotating linear polarizer (Thorlabs Inc., Newton, NJ) at 37 distinct polarization states (i.e., $0°$ to $180°$, $5°$ increments). The above imaging procedure was repeated for three linear phase shifts ($0°$, $120°$, and $240°$) of the spatial frequency pattern, based on spatial frequency domain imaging (SFDI) theory [100–102]. Image processing and data analyses were completed via custom MATLAB (MathWorks, Natick, MA) programs to examine the collagen fiber architecture of the tissue's region of interest (ROI), as defined by the BioRake tines. The quantified CFA information includes the collagen fiber orientation (θ_{fiber}) and the degree of optical anisotropy (DOA) at different loading states (i.e., post-preconditioning, and T_{C}:T_{R}=1:1, 1:0.5, 0.5:1). The DOA stems from the structural anisotropy of the collagen fibers, and therefore, we may attribute the optical anisotropy within the sample to the structural alignment of the CFA (DOA = 1, fully aligned case).

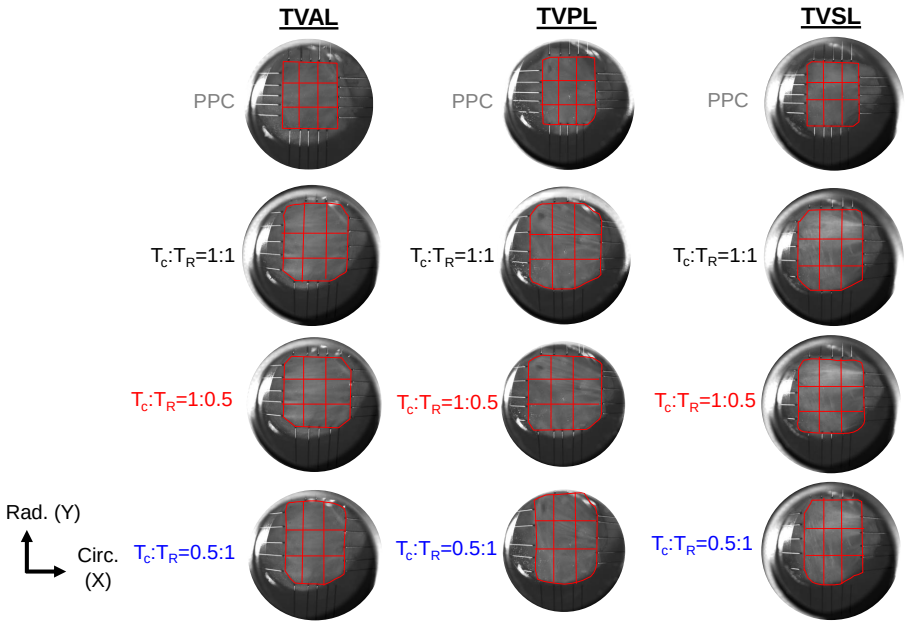

FIGURE 3.2 (a) 3x3 grid regions used for analyzing the spatial variations in the quantified load-dependent fiber orientation angle and DOA for the TVAL, TVPL, and TVSL tissue specimens. (T_{C}: circumferential tension, T_{R}: radial tension, PPC: post-preconditioning)

In addition to quantifying the load-dependent CFA's of the selected tissue's ROI, a 3×3 grid array as shown in Fig. 3.2 was used to further analyze the spatial variations of the changes in the collagen fiber architecture in response to mechanical loads. We developed a novel approach to capture the load-dependent changes of the CFA in HV leaflets by combining this optical technique with biaxial mechanical testing (Fig. 3.3) [98]. This opto-mechanical system permits the evaluation of the *same specimen* without chemical fixation, and has been used to observe the underlying CFA in other soft tissue structures [103–105].

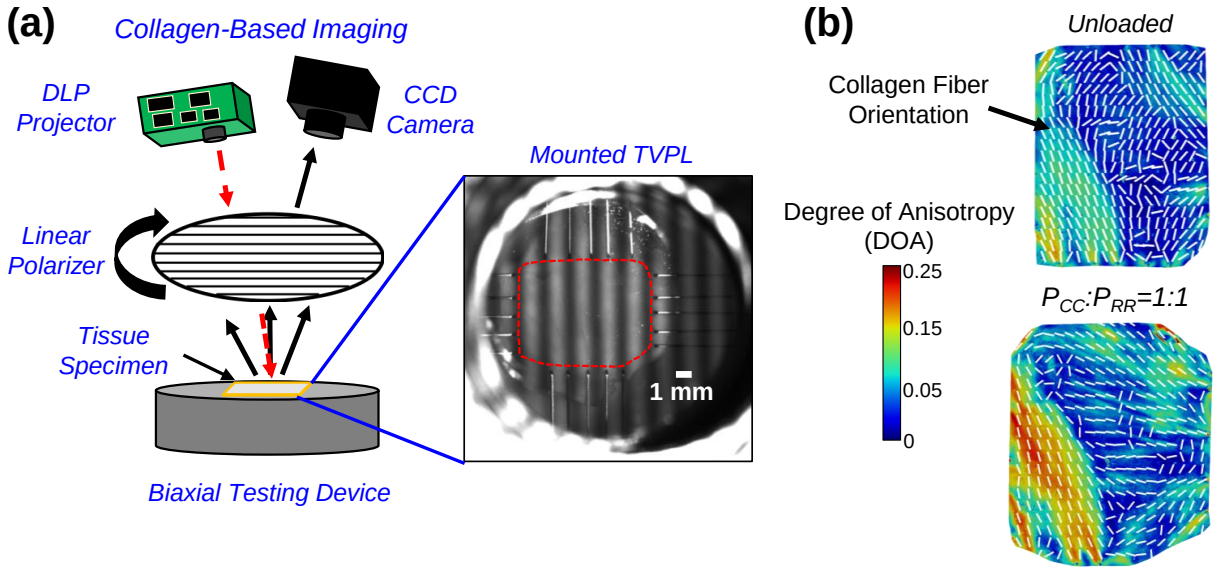

FIGURE 3.3 A novel approach combining (a) biaxial mechanical testing and a pSFDI collagen-based imaging device to quantify the (b) collagen fiber orientation (denoted by white dashed lines) and degree of optical anisotropy (colorbar) without the use of fixative methods.

The pSFDI imaging technique combines the ability of co-polarized imaging to quantify the birefringent fiber structures with the depth-discrimination capabilities of SFDI. During the polarized spatial frequency domain imaging procedure, polarization-state images (2560×2048 pixels) for each phase shift were obtained via pSFDI, and the acquired 37 images (i.e, $0°$ to $180°$ at a $5°$ increment) were then smoothed via an in-house MATLAB program using convolution with a 5×5 uniform kernel.

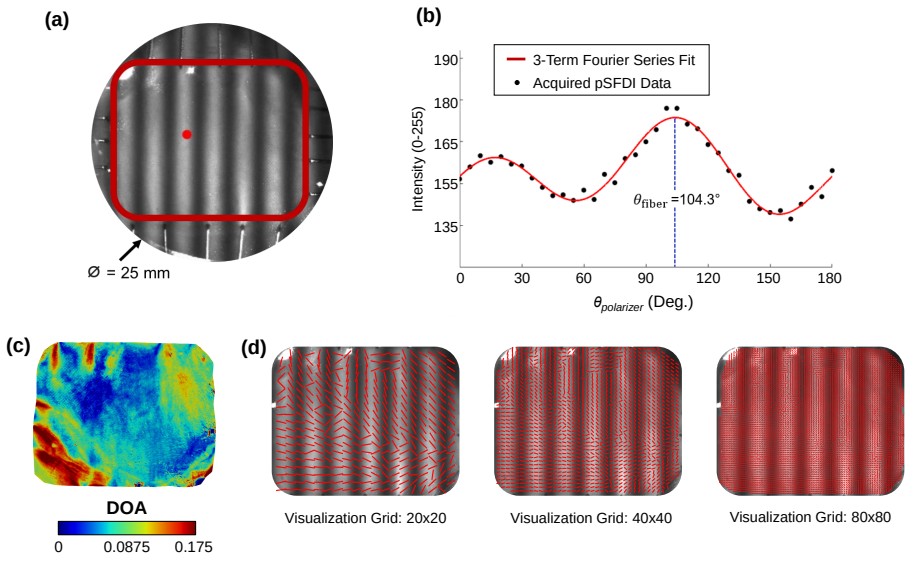

FIGURE 3.4 Demonstration of the pSFDI modality to capture the CFA: (a) an experimental photo of a representative TV leaflet specimen mounted to the BioTester system, with a defined region of interest as delimited by the red box, and (b) the quantified intensity-$\theta_{\text{polarizer}}$ relationship of a selected pixel point (see the red dot in (a)), together with the fitting of the 3-term Fourier series to the acquired data for predicting the collagen fiber orientation angle θ_{fiber}. (c) the quantified DOA throughout the ROI, and (d) vector plots of the quantified θ_{fiber} with an increasing level of visualization grid.

After smoothing, each image was then combined at each pixel to create the predicted birefringent reflected intensity, I_{out}:

$$I_{\text{out}} = \frac{1}{3}(I_{0^\circ} + I_{120^\circ} + I_{240^\circ}) \tag{3.1}$$

where I_{0°, I_{120°, and I_{240° are the pixel-wise intensities at each respective phase shift. The global maximum for each of these intensity functions occurs when the θ_{fiber} is both perpendicular and parallel with the polarizer's transmission axis, $\theta_{\text{polarizer}}$ (Fig. 3.4). The quantified birefringent reflected intensity is then approximated by a 3-term Fourier cosine series:

$$I_{\text{out}} = \left[\alpha_0 + \alpha_2[2(\theta_{\text{fiber}} - \theta_{\text{polarizer}})] + \alpha_4[4(\theta_{\text{fiber}} - \theta_{\text{polarizer}})]\right] \tag{3.2}$$

the three Fourier series terms: α_0, which represents the mean light intensity, and α_2 and α_4, which describe the sample's polarization dependent changes in intensity. Further, the optical anisotropy allows the examination of the local collagen fiber dispersion, which can be quantified through the Fourier series coefficient as the degree of optical anisotropy (DOA):

$$\mathrm{DOA} = 1 - \frac{\alpha_0}{\alpha_0 + \alpha_2 + \alpha_4} \tag{3.3}$$

When the collagen fibers have a greater structural alignment, the polarization-dependent intensity response has a greater influence on the back-scattered mean light intensity, and therefore, an increasing DOA.

3.2.4 Histological Analysis

To assess the distribution of extracellular matrix (ECM) constituents within each TV leaflet tissue, three rectangular samples (1×4 mm) were excised from each of the tested leaflets, with Region 1 defined as the strip near the TV annulus, and Region 3 defined as the strip close to the free edge (Fig. 3.1c). Dissected tissue strips were fixed in 10% formalin at room temperature ($23\,^{\circ}$C) for 48 hours, embedded in paraffin wax, and sectioned ($5-7\ \mu$m) for histological staining with Movat's Pentachrome. For all stained tissue samples, three microscopic images were acquired at a 10X objective lens (Olympus, Shinjuku, Tokyo, Japan), and the images were then analyzed using a color deconvolution plugin [106] in ImageJ (National Institute of Health, Bethesda, Maryland).

In brief, the color deconvolution method was used to separate the red/green/blue (RGB) images into various ECM components based upon the Movat's Pentachrome stain: (i) collagen fiber (yellow), (ii) elastin (dark purple), and (iii) non-fibrous ground substance (blue). The staining of these ECM constituents allowed for the determination of the four morphologically-distinct layers. The atrialis and ventricularis layers were identified by their outward surfaces towards the atrial and ventricular chambers. The spongiosa can be distinguished from the atrialis layer by the presence of hydrated GAGs and PGs (blue), whereas the fibrosa consists of primarily circumferentially-oriented collagen fibers (yellow). The ventricular was then defined by the presence of both elastin (dark purple) and collagen (yellow), located below the collagen-rich fibrosa layer [9, 10]. The

RGB-separated images were next made binary, and thresholding was applied to determine the integrated optical density (IOD) of each constituent. Mass fractions (ω_i) of the three morphological components were calculated using $\omega_i = \mathrm{IOD}_i/(\mathrm{IOD}_g + \mathrm{IOD}_c + \mathrm{IOD}_e)$, where the subscripts *g*, *c*, and *e* denote the non-fibrous ground substance, collagen fiber, and elastin, respectively, and the subscript *i* signifies the intact tissue, which carries *g*, *c*, and *e*. Additionally, the thicknesses of the whole leaflet and the different tissue layers (i.e., atrialis, spongiosa, fibrosa, and ventricularis, from the atrial to ventricular sides) were measured from each image at three random locations and reported as the mean.

3.2.5 Statistical Analysis

Statistical analysis was performed in Prism (GraphPad, San Diego, CA) for the TV leaflets of the representative heart #1. First, the mass fraction for the three regionally-varying tissue strips were compared within the same leaflet for each of the three TV leaflets. Secondly, the variations in the mass fractions for the different tissue strips in the same relative locations across different leaflets were compared. These observations were compared based on the null hypothesis that the mass fractions for all constituents are uniform across each TV leaflet and show no variance between any two TV leaflets. The two-way Analysis of Variance (ANOVA) was performed, and p-values <0.05 were considered as statistically significant, pointing towards constituent variations.

3.3 Results

3.3.1 Biaxial Mechanical Testing Results

J-shape, nonlinear membrane tension-stretch curves were observed for each TV leaflet in both the circumferential and radial tissue directions (see the left column in Fig. 3.5a-c). Under low tensions ($0-2$ N/m), there was a relatively linear and compliant response, where minor increases in the applied loading caused substantial increases in the tissue stretches (Fig. 3.5a-c). This low-force region of the membrane tension-stretch curve contrasted with the stiffer, nearly asymptotic portion of the mechanical behaviors observed under larger applied loads (>10 N/m). For all three TV leaflets from the representative heart #1, the tissue stretches changed minimally between the two equibiaxial load-

ing states (T_C:T_R=1:1, 2:2), yielding an increase of 2.09% in the circumferential stretch λ_C and a 4.43% increase in the radial stretch λ_R with those changes as the average over the TVAL, TVPL, and TVSL specimens (Table 3.1). Further, under non-equibiaxial loading (T_C:T_R=$1:0.5$ and T_C:T_R=0.5:1), the investigated TV leaflets exhibited a larger stretch in the radial direction, regardless of the direction with the dominant load. For example, in the TVAL specimen, a circumferential stretch λ_C of 1.42 was observed, together with a radial stretch λ_R of 1.51 under the circumferentially-dominant loading (i.e., T_C:T_R=1:0.5). Interestingly, the TVPL specimen displayed the most compliant mechanical behaviors among all the three TV leaflets in both the tissue's circumferential and radial directions (Table 3.1 and Fig. 3.5).

TABLE 3.1 The quantified tissue stretches for the TV specimens under various biaxial tension protocols, together with the pixels within the tissue's ROI corresponding to the pSFDI-quantified results of the load-dependent CFA. Values are reported as mean ± SEM ($n = 3$).

T_C:T_R	Circumferential Stretch λ_C			Radial Stretch λ_R			Pixels in the Tissue ROI (pSFDI)		
	TVAL	TVPL	TVSL	TVAL	TVPL	TVSL	TVAL	TVPL	TVSL
PPC	1.00	1.00	1.00	1.00	1.00	1.00	368,508	434,703	377,398
1:1†	1.35 ± 0.03	1.43 ± 0.02	1.39 ± 0.01	1.59 ± 0.06	1.71 ± 0.03	1.77 ± 0.04	536,726	624,611	541,161
0.5:1	1.25 ± 0.02	1.28 ± 0.01	1.24 ± 0.01	1.67 ± 0.05	1.81 ± 0.05	1.87 ± 0.04	550,747	626,641	533,910
1:0.5	1.35 ± 0.03	1.49 ± 0.02	1.43 ± 0.02	1.52 ± 0.01	1.55 ± 0.01	1.61 ± 0.05	505,182	567,840	545,645
2:2	1.40	1.50	1.38	1.75	1.87	1.81	584,990	697,596	625,324

†Note that the targeted membrane tension is 25 N/m with respect to the equibiaxial loading protocol, i.e., T_C:T_R=(25 N/m):(25 N/m).

The mean ± standard error of the mean (SEM) values of the tissue stretches from the three porcine hearts ($n = 3$) were determined and reported as follows: (i) greater extensibility in the radial direction under equibiaxial loading (TVAL: λ_C=1.35 ± 0.03, λ_R=1.59 ± 0.06; TVPL: λ_C=1.43 ± 0.02, λ_R=1.71 ± 0.03; TVSL: λ_C=1.39 ± 0.01, λ_R=1.77 ± 0.04); (ii) smaller changes in the circumferential extensibility under circumferentially-dominant loading (i.e., T_C:T_R=1:0.5) compared to the radial direction (i.e., TVAL: λ_C=1.35 ± 0.03, λ_R=1.52 ± 0.01; TVPL: λ_C=1.49 ± 0.02, λ_R=1.55 ± 0.01; TVSL: λ_C=1.43 ± 0.02, λ_R=1.61 ± 0.05); (iii) under radially-dominant loading (i.e., T_C:T_R=0.5:1), the TVSL displaying the greatest extensibility among the TV leaflets (TVAL: λ_C=1.25 ± 0.02, λ_R=1.67 ± 0.05; TVPL: λ_C=1.28 ± 0.01, λ_R=1.81 ± 0.05; TVSL: λ_C=1.24 ± 0.01, λ_R=1.87 ± 0.04). The greater equibiaxial loading protocol (i.e.,T_C:T_R=2:2) was only used for TV leaflets extracted from

heart #1, based on the observed minimal changes between protocol T_C:T_R=2:2 and protocol T_C:T_R=1:1.

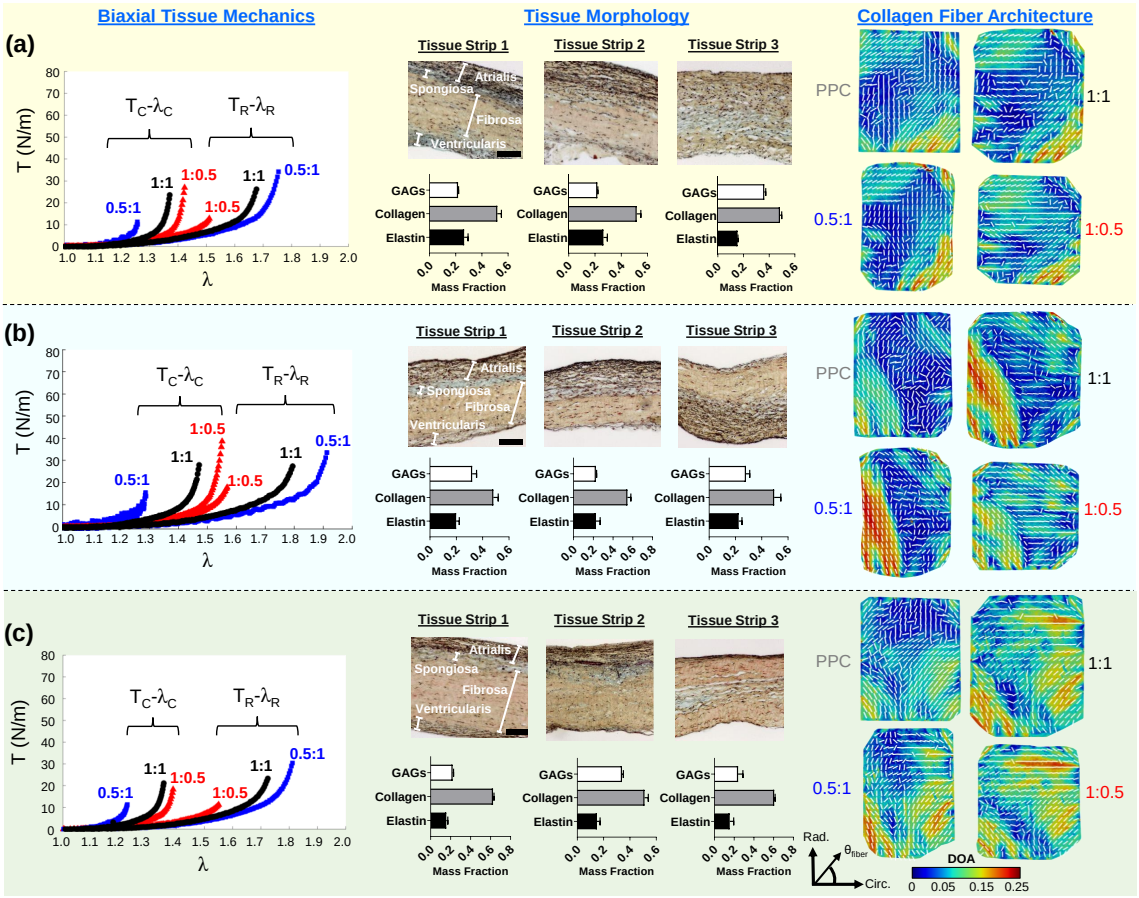

FIGURE 3.5 Representative heart #1 quantifications as follows: (Left) membrane tension (T) versus tissue stretch (λ) results of biaxial testing experiments (subscripts C and R stand for the circumferential and radial directions, respectively), (middle) histology-based evaluations of tissue's morphology and constituents, and (right) the pSFDI-quantified collagen fiber architecture for: (a) the TVAL, (b) the TVPL, and (c) the TVSL specimens. In the right column, the dash lines represent the predicted fiber orientation angle and the colormaps denote the DOA

3.3.2 Histological Results

The thicknesses and percent mass compositions for each tissue layer of the TV leaflets, as found by histological analysis, are summarized in Table 3.2. The TVSL was shown to be the thickest leaflet across all three hearts (783.1 ± 62.6 μm), while also contain-

ing the largest percent mass composition for the ventricularis layer (12.5%) and the greatest mean total thickness for the fibrosa ($363.3\pm41.1\ \mu\mathrm{m}$). The TVPL presented the greatest percent mass composition for both the atrialis and the fibrosa layers (A = 33.3%; F = 50.0%) among all leaflets, with the second largest overall mean total thickness ($705.4\pm22.2\ \mu\mathrm{m}$). Finally, the smallest mean total thickness across all leaflets occurred in the TVAL ($614.0\pm23.9\ \mu\mathrm{m}$). Quantifications of the TV leaflets' morphological constituents from the representative heart #1 showed that all three TV leaflets are composed primarily of collagen fibers (see the middle column in Fig. 3.5a-c.

First of all, by comparing the different regions within the same TV leaflet tissue (Table 3.3), significant regional variance in the elastin was noted between Regions 2 and Region 3 of the TVAL ($p = 0.023$). For the TVAL, the GAGs were also found to vary significantly between Region 1 and Region 3 ($p = 0.002$) and between Region 2 and Region 3 ($p = 0.001$). For the TVPL, significant differences were found in the GAG contents between Region 1 and Region 2 ($p = 0.025$). In contrast, the TVSL exhibited significant differences in both the collagen ($p = 0.029$) and the GAGs ($p = 0.004$) between Region 1 and Region 2, while only varying in the GAG contents between Region 2 and Region 3 ($p = 0.017$).

Secondly, by comparing similar regional tissue strips across all TV leaflets from heart #1 (Table 3.4), the TVAL and the TVPL deviated significantly only in the GAG contents for Region 1 ($p = 0.029$), whereas the TVAL and the TVSL differed significantly in both the elastin ($p = 0.018$) and the GAGs ($p = 0.004$) for Region 1, and in the collagen ($p = 0.019$) and the GAGs ($p = 0.004$) for Region 3. The TVSL showed significant differentiation when compared to TVPL in all the 3 regions, primarily for the collagen content ($p = 0.006$) and the GAG contents ($p = 0.016$) in Region 1, for the GAG contents ($p = 0.007$) in Region 2, and for the collagen content ($p = 0.034$) in Region 3.

TABLE 3.2 Histologically-quantified thickness and percent composition of four tissue layers (i.e., atrialis, spongiosa, fibrosa, and ventricularis) for TVAL, TVPL, and TVSL specimens. Values are reported as mean ± SEM (n=3).

Tissue Layer	Thickness (Respective %)		
	TVAL	TVPL	TVSL
Atrialis (A)	168.8±18.1 μm (27.5%)	235.1±6.3 μm(33.3%)	230.8±16.3 μm (29.5%)
Spongiosa (S)	77.6±12.4 μm (12.6%)	86.2±11.7 μm (12.2%)	90.8±13.8 μm (11.6%)
Fibrosa (F)	297.6±15.6 μm (48.5%)	289.1±15.4 μm (50.0%)	363.3±41.1 μm (46.4%)
Ventricularis (V)	69.7±4.5 μm (27.5%)	73.8±3.2 μm (10.5%)	98.2±14.9 μm (12.5%)
Total Thickness	614.0±23.9 μm	705.4±22.2 μm	783.1±62.6 μm

TABLE 3.3 Statistical comparisons (p-values) of the constituent mass fractions between any two regions within each of the three representative heart #1 TV leaflets (see Fig. 3.1c).

	Within the TVAL			Within the TVPL			Within the TVSL		
	Collagen	Elastin	GAGs	Collagen	Elastin	GAGs	Collagen	Elastin	GAGs
Region 1 vs. Region 2	0.593	0.377	0.933	0.266	0.720	0.025	0.029	0.983	0.004
Region 1 vs. Region 3	0.189	0.283	0.002	0.937	0.767	0.449	0.889	0.999	0.809
Region 2 vs. Region 3	0.686	0.023	0.001	0.429	0.997	0.244	0.073	0.989	0.017

TABLE 3.4 Statistical comparisons (p-values) of the constituent's mass fraction between any two TV leaflets regarding the three regions for the representative heart #1 (see Fig. 3.1c).

	Within Region 1			Within Region 2			Within Region 3		
	Collagen	Elastin	GAGs	Collagen	Elastin	GAGs	Collagen	Elastin	GAGs
TVAL vs. TVPL	0.166	0.924	0.029	0.769	0.604	0.964	0.963	0.169	0.054
TVAL vs. TVSL	0.253	0.311	0.952	0.981	0.018	0.004	0.019	0.999	0.004
TVPL vs. TVSL	0.006	0.510	0.016	0.659	0.121	0.007	0.034	0.176	0.441

3.3.3 Load-Dependent Collagen Fiber Architecture

For each TV leaflet, the load-dependent changes in both the DOA and the collagen fiber orientation were quantified throughout the entire tissue's region of interest (see the right column in Fig. 3.5a-c) with the representative specimen's histograms presented in Fig. 3.6, whereas the results of the regional analysis, based on the 3×3 grid array are shown in Fig. 3.7 at the unloaded state to highlight the TV leaflets intrinsic characteristics. Regional analysis regarding varying biaxial loading protocols can be found at the end of the chapter in Fig. 3.8, Fig. 3.9, and Fig. 3.10 for the TVAL, TVPL, and TVSL, respectively.

Four primary trends were observed in the quantification of the collagen fiber architecture of the three heart #1 representative TV leaflets, with an attempt to relate the collagen fiber spatial alignment and re-orientation to the direction of applied loading.

- First, for the non-equibiaxial loading protocols, the collagen fiber orientations θ_{fiber} displayed a shift towards the direction of the maximum applied loading (Fig. 3.6). Moreover, collagen fiber networks became more aligned, as evidenced by the increasing DOA within the central regions of the tissues (Fig. 3.8–Fig. 3.10).

- Secondly, the largest changes in the mean collagen fiber orientation θ_{fiber} were observed in the TVPL under equibiaxial and radially-dominant loading conditions (Table 3.5), with differences of 37.5% (T_{C}:T_{R}=1:1), 36.0% (T_{C}:T_{R}=2:2), and 42.2% (T_{C}:T_{R}=0.5:1), compared to the post-preconditioning (PPC) state, also referred as the "unloaded" state in the remaining discussion.

- Third, the largest percent change in the quantified DOA, as compared to the PPC state, occurred under the radially-dominant loading (T_{C}:T_{R}=0.5:1) with a 10.8% increase for the TVAL, a 39.1% increase for the TVPL, and a 47.4% increase for the TVSL, respectively (Table 3.5). Under circumferentially-dominant loading (T_{C}:T_{R}=1:0.5), a minimal change of 1.4% in DOA was seen for the TVAL, with a 27.3% and a 32.4% increase for the TVPL and TVSL, respectively (Table 3.5).

- Fourth, across all the loading protocols, the TVSL displayed the largest increase in the DOA (47.3%) under the radially-dominant loading, whereas the smallest change was found for the TVAL (1.4%) under equibiaxial and circumferentially-dominant loading (Table 3.5).

Changes in the predicted θ_{fiber} and DOA of the entire tissue's ROI for heart #2 and heart #3 can be found in Table 3.6 and Table 3.7, respectively.

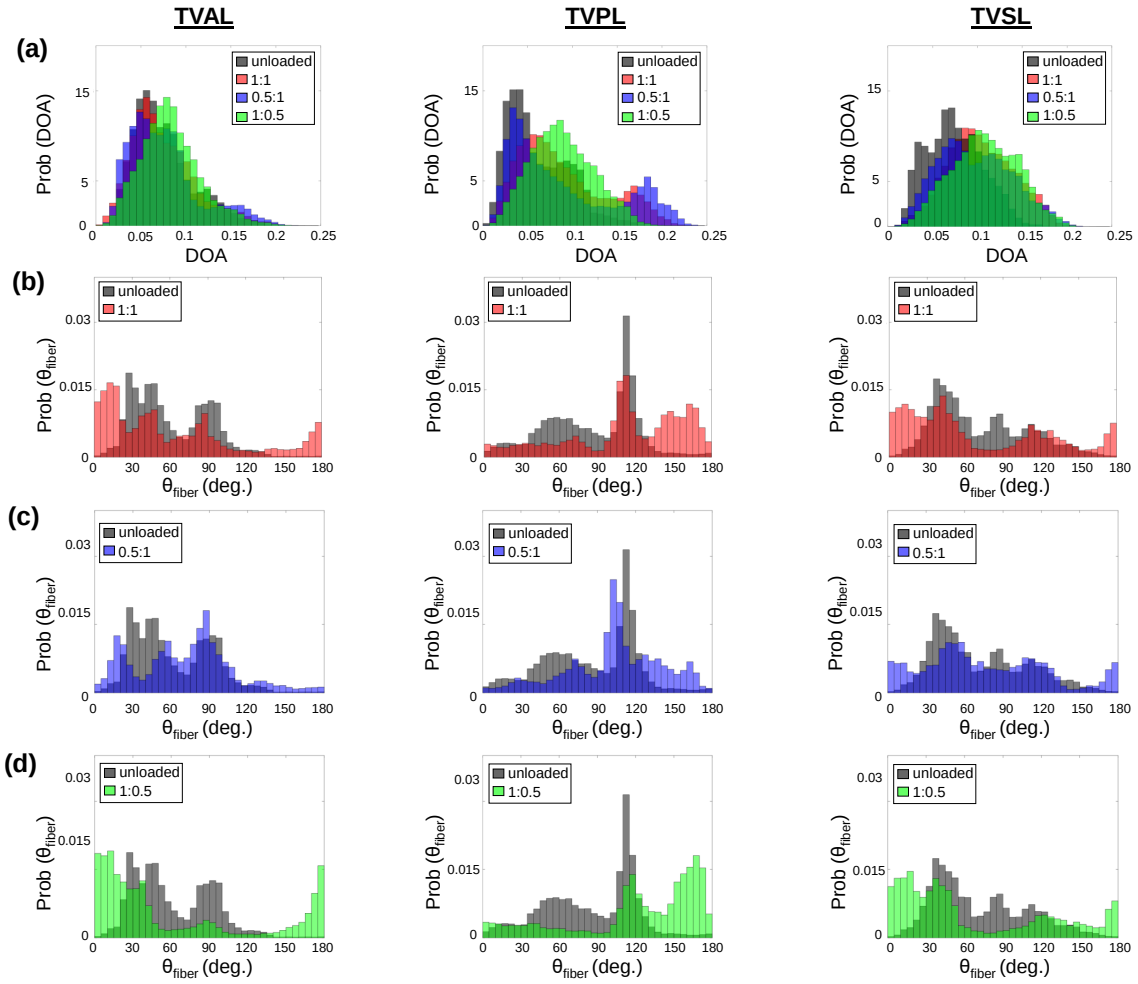

FIGURE 3.6 Comparisons of the load-dependent collagen fiber architecture for the entire tissue's ROI of the representative heart #1 (see the right column in Fig. 3.5a-c): (a) the predicted DOA, (b) the predicted θ_{fiber} between unloaded and equibiaxial loading (T_{C}:T_{R}=1:1), (c) the predicted θ_{fiber} between unloaded and radially-dominate loading (T_{C}:T_{R}=0.5:1), and (d) the predicted θ_{fiber} between unloaded and circumferentially-dominate loading (TT_{C}:T_{R}=1:0.5).

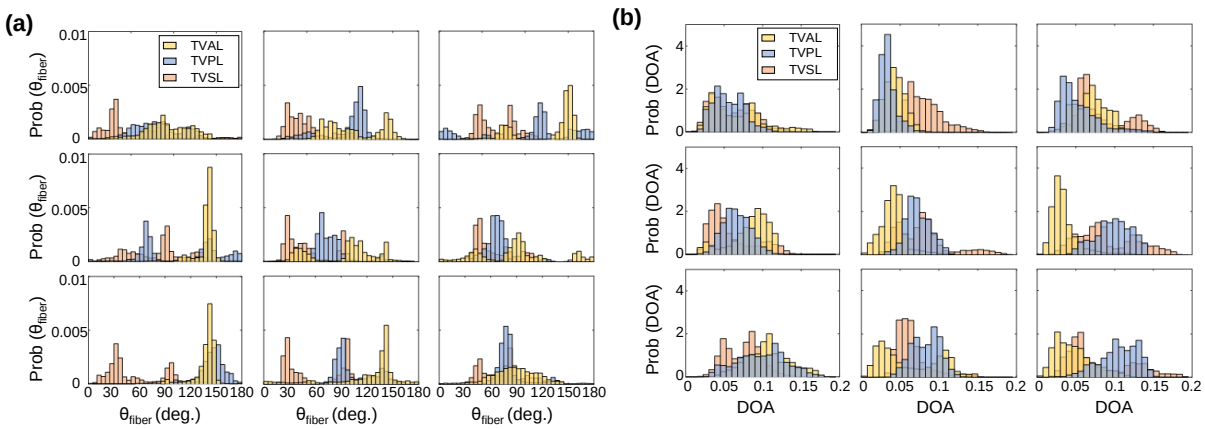

FIGURE 3.7 3x3 grid comparisons of (a) the predicted θ_{fiber}, and (b) the predicted DOA in the unloaded state for the TVAL, TVPL, and TVSL specimens from heart #1.

TABLE 3.5 Mean, skewness, and standard deviation (SD) for the predicted θ_{fiber} and the DOA of the entire tissue's ROI (see right column in Fig. 3.5a-c) for the TVAL, TVPL, and TVSL specimens from heart #1, considering various biaxial tension loading conditions

	DOA (TVAL)			DOA (TVPL)			DOA (TVSL)		
T_{C}:T_{R}	Mean	Skewness	SD	Mean	Skewness	SD	Mean	Skewness	SD
PPC	0.074	0.873	0.033	0.064	0.708	0.036	0.074	0.314	0.031
1:1	0.075	0.879	0.035	0.089	0.654	0.048	0.104	0.155	0.036
1:0.5	0.073	1.264	0.038	0.088	0.730	0.059	0.098	0.317	0.041
0.5:1	0.082	0.564	0.032	0.089	0.257	0.034	0.109	-0.012	0.036
2:2	0.072	0.930	0.034	0.087	0.700	0.048	0.102	0.142	0.037
	θ_{fiber} (TVAL)			θ_{fiber} (TVPL)			θ_{fiber} (TVSL)		
T_{C}:T_{R}	Mean	Skewness	SD	Mean	Skewness	SD	Mean	Skewness	SD
PPC	61.6°	0.588	30.8°	85.9°	-0.377	34.6°	70.9°	0.621	36.3°
1:1	60.6°	0.906	52.3°	112.4°	-0.698	46.3°	67.2°	0.655	53.5°
1:0.5	69.7°	0.348	38.3°	103.3°	-0.462	37.2°	77.1°	0.398	46.9°
0.5:1	61.6°	0.889	63.4°	122.3°	-1.042	49.3°	63.6°	0.799	56.8°
2:2	60.1°	0.928	52.5°	111.1°	-0.665	47.2°	66.8°	0.655	53.6°

TABLE 3.6 The percent changes in mean, skewness, and standard deviation (SD) for the predicted θ_{fiber} and the DOA of the entire tissue's ROI for the TVAL, TVPL, and TVSL specimens of heart #2

	DOA (TVAL)			DOA (TVPL)			DOA (TVSL)		
T_{C}:T_{R}	Mean	Skewness	SD	Mean	Skewness	SD	Mean	Skewness	SD
PPC	0.069	0.791	0.025	0.071	1.377	0.029	0.062	0.410	0.026
1:1	-1.6	12.4	9.5	-5.3	-10.0	27.0	14.3	-23.1	12.2
1:0.5	12.2	-5.2	41.1	6.1	-8.1	39.9	43.5	-47.6	13.5
0.5:1	-3.3	-18.0	-0.6	-7.4	-12.8	6.7	15.0	-16.4	19.2
	θ_{fiber} (TVAL)			θ_{fiber} (TVPL)			θ_{fiber} (TVSL)		
T_{C}:T_{R}	Mean	Skewness	SD	Mean	Skewness	SD	Mean	Skewness	SD
PPC	93.4°	-0.365	30.0°	105.3°	-0.891	26.3°	106.0°	-0.462	31.9°
1:1	-1.4	-18.6	15.2	6.5	-19.4	47.1	0.3	27.9	54.1
1:0.5	5.5	12.5	-2.1	14.3	-16.5	2.6	11.5	54.0	3.4
0.5:1	-9.9	-130.9	25.6	-3.5	-46.5	78.4	-13.8	-94.0	68.9

TABLE 3.7 The percent changes in mean, skewness, and standard deviation (SD) for the predicted θ_{fiber} and the DOA of the entire tissue's ROI for the TVAL, TVPL, and TVSL specimens of heart #3

	DOA (TVAL)			DOA (TVPL)			DOA (TVSL)		
T_{C}:T_{R}	Mean	Skewness	SD	Mean	Skewness	SD	Mean	Skewness	SD
PPC	0.069	0.791	0.025	0.071	1.377	0.029	0.062	0.410	0.026
1:1	-1.6	12.4	9.5	-5.3	-10.0	27.0	14.3	-23.1	12.2
1:0.5	12.2	-5.2	41.1	6.1	-8.1	39.9	43.5	-47.6	13.5
0.5:1	-3.3	-18.0	-0.6	-7.4	-12.8	6.7	15.0	-16.4	19.2
	θ_{fiber} (TVAL)			θ_{fiber} (TVPL)			θ_{fiber} (TVSL)		
T_{C}:T_{R}	Mean	Skewness	SD	Mean	Skewness	SD	Mean	Skewness	SD
PPC	93.4°	-0.365	30.0°	105.3°	-0.891	26.3°	106.0°	-0.462	31.9°
1:1	-1.4	-18.6	15.2	6.5	-19.4	47.1	0.3	27.9	54.1
1:0.5	5.5	12.5	-2.1	14.3	-16.5	2.6	11.5	54.0	3.4
0.5:1	-9.9	-130.9	25.6	-3.5	-46.5	78.4	-13.8	-94.0	68.9

3.3.4 Changes in the CFA Associated with the Equibiaxial Loading States

The TVAL specimen displayed minimal changes in θ_{fiber} from $61.6°$ in the PPC state to $60.6°$ and $60.1°$ under T_C:T_R=1:1 and T_C:T_R=2:2, respectively. Similar trends were observed for the spatial alignment of the fibers (i.e., DOA), varying from 0.074 in the PPC state to 0.075 under T_C:T_R=1:1 and to 0.072 under T_C:T_R=2:2. In contrast, the TVPL showed profound changes in θ_{fiber}, yielding a 30.8% difference from the PPC state (85.9◦) to the T_C:T_R=1:1 loading protocol ($112.4°$) and a 29.3% difference when compared to the T_C:T_R=2:2 loading state ($111.1\,°$). Similarly, the quantified DOA for the PPC state displayed increases of 37.5% and 36.0% compared to T_C:T_R=1:1 and T_C:T_R=2:2 loading protocols, respectively. For the TVSL, θ_{fiber} varied from the PPC state ($70.9°$) by 5.5% for the T_C:T_R=1:1 state ($67.2°$) and 5.8% for the T_C:T_R=2:2 state ($66.8°$C), whereas the DOA increased by 40.5% and 37.8% under T_C:T_R=1:1 and T_C:T_R=2:2, respectively, when compared to the PPC state.

3.3.5 Changes in the CFA Associated with the Circumferentially-Dominant Loading (T_C:T_R=1:0.5)

For all TV leaflets, θ_{fiber} shifted towards the tissue's circumferential direction with an increased DOA under circumferentially-dominant loading (Fig. 3.5a-c). Specifically, the TVAL displayed a 13.1% difference in θ_{fiber} between the PPC state ($61.6°$) and the circumferentially-loaded state ($69.7°$), together with a negligible change in the DOA (unloaded=0.074 versus loaded=0.073). For the TVPL, a 20.3% change in θ_{fiber} was observed, along with a 27.3% increase in the DOA, whereas the TVSL displayed a shift in θ_{fiber} from $70.9°$ (PPC) to $77.1°$ (circumferentially-dominant loaded) and a greater change in the quantified DOA (32.4%).

3.3.6 Changes in the CFA Associated with the Radially-Dominant Loading (T_C:T_R=0.5:1)

When radially-dominant loading was considered, the CFAs of the TV leaflet specimens tended to reorient towards the tissue's radial direction, with greater changes in the quan-

tified DOA throughout the tissue compared to other loading protocols. Specifically, the TVAL showed a minimal change in θ_{fiber} under radially-dominant loading conditions, but a 10.8% increase in the DOA was observed between the PPC (0.074) and radially-dominant loaded states (0.082). In contrast, the TVPL's collagen fibers reoriented towards the radial direction ($122.3°$) with a 42.4% change between the PPC and loaded state, while the DOA increased by 39.1%. For the TVSL, the quantified θ_{fiber} varied from $70.9°$ (PPC) to $63.6°$ (loaded), together with a 47.4% increase in quantified DOA.

3.4 Discussion

3.4.1 Mechanics-Related Observations

The non-linear stress-strain response for each TV leaflet was consistent with the findings from the previous studies [47, 48, 53]. In the present study, for all three TV leaflets, the radial direction of the tissues displayed greater stretches than that of the circumferential direction under both equibiaxial and non-equibiaxial tensions. This anisotropic tissue mechanical response has also been observed by Pokutta-Paskaleva *et al.* [51] and Mathur *et al.* [107] through similar biaxial testing method among others [10, 48]. Essential behaviors of soft collagenous tissues, such as heart valve leaflets, have been further characterized through various fiber re-orientation theories and rheological constitutive models. Lanir *et al.* and Fung *et al.* have contributed to these models for various fibrous soft tissues, taking into consideration the structure of the tissues' constituents and their mechanical properties [108–110], yet further experimentation is needed to quantify the complex mechanical interactions between constituents that yields this stress-strain response. The anisotropic responses of the TV leaflets, although well documented, have not yet been examined within the context of the pSFDI-based collagen microstructural quantification as shown in the current pilot study. Supplementing these well-known biomechanical trends within the TV leaflets, together with such novel microstructural quantifications ultimately, will lead to an improved understanding of collagen fiber alignment and reorientation in response to mechanical loading.

3.4.2 Collagen Fiber Architecture-Related Observations

We found in this pilot study that the CFA of each TV leaflet tissue is related to the directional-dependence of the tissue-level mechanics. As previously discussed, each tissue showed a greater extensibility in the radial direction (Table 3.1), which may be correlated to the collagen fiber's initial circumferential orientation (see the right column in Fig. 3.5a-c). As increasing tension was applied to the tissue, the asymptotic region of the membrane tension-stretch curve is associated with the rotation of crimped collagen fibers towards the radial direction. These fibers were then straightened, exhibiting the low-force linear region of the curve. The collagen fibers' ability to reorient in response to the applied loading was also shown to result in the higher spatial alignment. This increased alignment of the collagen fibers is exemplified under the radially-dominant loading conditions, where the largest changes in DOA values were found in comparison with to the PPC (unloaded) state (Table 3.5). Similar trends in the load-dependent changes in the CFAs were also observed under non-equiaxial loading. Specifically, for all three TV leaflets, the collagen fibers were found to shift towards the direction of dominant loading (see the right column in Fig. 3.5a-c), yielding an increase in the quantified DOAs after fiber reorientation. In contrast, when circumferentially-dominant loading was considered, the quantified θ_{fiber} became more closely aligned with the tissue's circumferential direction (Fig. 3.6). These observations in our pilot study are in a good agreement with those findings from the previous studies on the other heart valve leaflets and the TV leaflets with chemical fixation [81, 89]. By employing our combined experimental approach, the collagen fiber architecture of the same TV leaflet can be quantified at different equibiaxial and non-equibiaxial loading states without the use of chemical fixation. This improvement on the previous collagen-microstructure observations [86, 93] permits further investigations into how the constituent compositions of each TV leaflet tissue contributes to the respective mechanical-microstructure responses under varying loads.

Apart from examining the load-dependent changes among the CFAs for all three TV leaflets, each specimen was also observed in the "unloaded", or PPC state. The ROI for each TV leaflet was divided into 9 sub-regions (Fig. 3.2), and the collagen fiber orientation and DOA of the tissue was extracted to further investigate the intrinsic characteristics of the TV leaflets. The TVAL and TVSL leaflets each displayed primarily

circumferentially-dominant CFAs throughout all region of the tissue, with some variation towards in radially-oriented collagen fibers in the belly portion of the tissue and near the annulus (Fig. 3.7). The TVPL, on the other hand, exhibited a predominantly radially-oriented CFA throughout the entirety of the tissue, with θ_{fiber} closely aligned with 90°. The DOA of the TV leaflets remained consistent throughout each section of the tissue (Fig. 3.5), with no statistically-significant change in spatial alignment between the collagen fibers. This assertion can be connected to the collagen fiber's naturally crimped state, where with greater load, the CFA will straighten and recruit multiple fiber families to compensate for the induced stress on the tissue. Observing the natural CFA and spatial alignment in TV leaflets can be used to further explain the mechanics-microstructure relationship that has been shown to vary regionally across TV anterior leaflet specimens [56].

To further investigate the spatial heterogeneity of the collagen fiber architecture for each TV leaflet, the 9 sub-regions were observed at varying biaxial protocols. Variations in the fiber orientation angle were observed across different sub-regions of the tissue, as some sub-regions of the tissue showed a significant shift in the fiber orientation angle in response to the mechanical loads, while other sub-regions remained unchanged (Fig. 3.8–Fig. 3.10). For example, the TVAL exhibited circumferentially-oriented fibers in the unloaded state, but when radially loaded, the fibers in the center sub-region of the tissue shifted more towards the radial direction compared to the upper portion of the tissue (Fig. 3.8b). The differences in collagen fiber reorientation in response to loading throughout these sub-regions can be connected to the regional variations in biaxial mechanical response previously observed in TV leaflets [56]. The coupling of both the regionally diverse mechanical and microstructural responses can be used to validate affine kinematic theories regarding this relationship. As for the regional variations in the alignment of collagen fibers for each TV leaflet tissue, the belly portion, along with the rough zone (i.e., tissue strip 3, see Fig. 3.1c), showed higher DOA values than the upper portion of the tissue. To supplement these findings, histological analysis for each TV leaflet displayed differences in the constituent mass fraction across the tissue domain, further highlighting potential underlying mechanisms that contribute to collagen fiber reorientation in response to applied loading. The connection between the collagen fiber alignment and the histomorphological compositions has yet to be observed within literature. For example, previous studies are largely limited by optical clearing solutions

and a more confined FOV [93], and, therefore, regional analysis of the load-dependent CFAs may not be feasible. Our observations, presented in this article, provide unique, spatially-varying collagen fiber architectural information that can be implemented into current rheological models for accurate representation of the bulk tissue response.

3.4.3 Study Limitations and Future Work

Throughout this pilot study, we encountered difficulty in determining an average thickness for each sample, primarily due to non-uniformity and other regions across the tissue, by using a contact-based caliper measurement technique. This limitation was moderately alleviated by measuring the thickness across the leaflet in three different regions and averaging the observed thicknesses. Another limitation of this pilot study is the tine-based biaxial loading technique used. When observing the collagen fiber microstructure via the pSFDI-based technique, the tines inserted in the tissue were captured in the images associated with each phase shift, producing edge artifacts on the CFA map (e.g., see the right column in Fig. 3.5a-c). An extension of this limitation is the displacement-controlled biaxial testing methods used to emulate the target membrane tensions similar to the force-controlled biaxial mechanical tests. This was done by performing displacement-controlled loading to the specimen size associated with the peak loading stress, but due to the stress relaxation of the tissue when determining the peak specimen size, there was a reduction in the target stress values. In regards to the histological limitations presented in this pilot study, we attempted to excise the 3 tissue strips within the observed ROI, but our calculations did not account for the possibility of the strips including parts of the tissue outside of the ROI which could alter the observed trends. Another limitation of this work is the examination of only three representative porcine hearts ($n = 3$). Definite conclusions and trends cannot be drawn regarding the TV leaflets without including a much larger sample size.

Despite these restrictions, our pilot study provides a first look into the investigations of the mechanical-microstructural relationships within TV leaflets. Subsequent studies may warrant a more in-depth examination of the TV with a larger sample size to draw statistically supported conclusions. Regarding other potential future extensions, the microstructural-mechanical relationship in collagenous heart valve leaflet tissue can also be examined under various mechanical tests to quantify behaviors such as the

preconditioning effect, the stress-relaxation effect, and the creep effect, informing fiber kinematic models such as the previous ones developed for the mitral valve and the aortic valve [13, 65, 69, 111]. This combined experimental approach could also be used to investigate other collagenous tissues, utilizing its unique capability to elucidate the microstructural-mechanical relationship and inform high-fidelity constitutive models.

3.5 Concluding Remarks

In this pilot study, we have presented a novel systematic framework for characterizing collagenous tissues that utilizes both the histology-based morphological assessment and the pSFDI modality in conjunction with biaxial mechanical testing, allowing for a direction examination of the interrelationship between tissue mechanics and collagen microstructures in response to mechanical loads. In the case of the TV leaflets, observing these load-dependent microstructural changes will lead to further developments of improved computational models. Such enhanced computational modeling tools could not only aid in a better understanding of TV function as well as its associated abnormalities/diseases, but they could also be used for patient-specific surgical planning and treatment options. Preoperative guidance in assessing the achievability of a successful tricuspid valve repair, thereby avoiding a less desirable valve replacement, would be of great benefit. The application of this experimental approach is readily applicable to other cardiovascular collagenous tissues (e.g., the aortic valve cusps, and the pulmonary valve cusps) to complement the current understanding in the field. The proposed systematic experimental framework also provides new frontiers and understanding within the field of cardiovascular biomechanics, offering a potential to advance the development of novel clinical therapeutics for TV diseases.

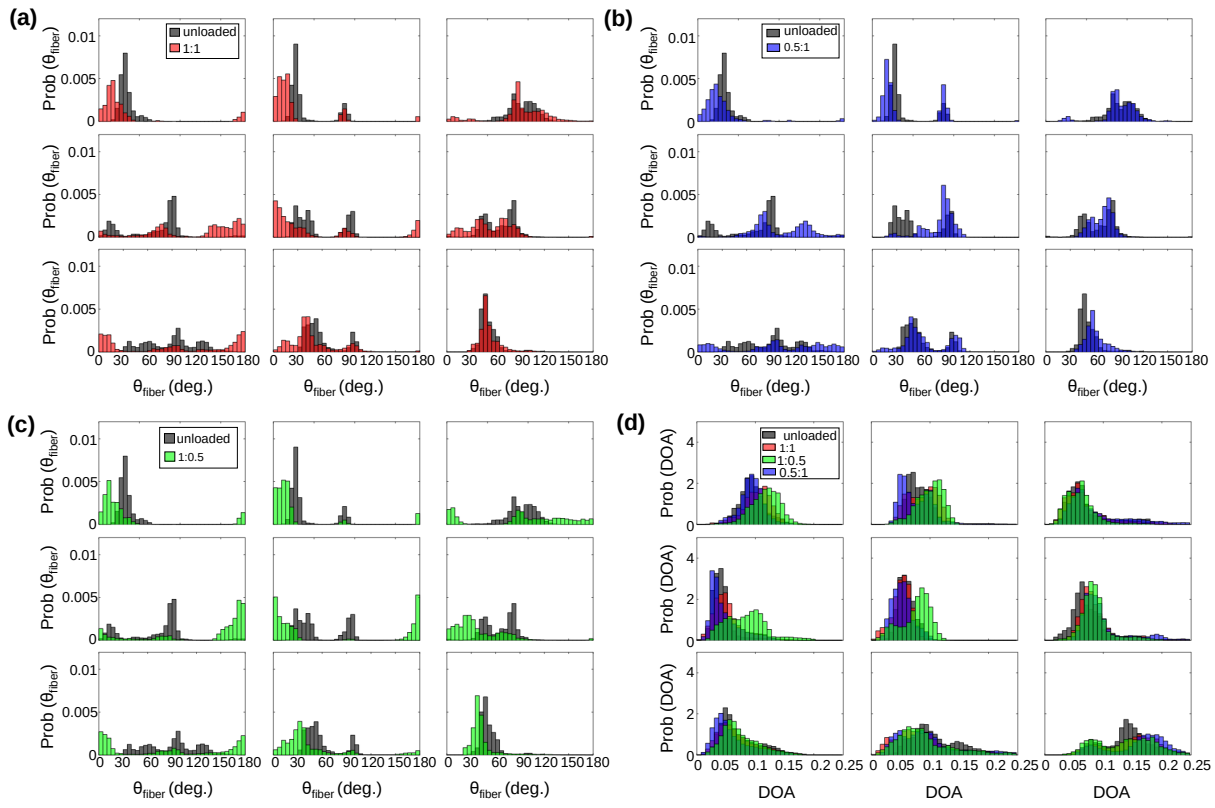

FIGURE 3.8 3x3 grid comparisons of the predicted θ_{fiber}: (a) between unloaded and equibiaxial loading, (b) between unloaded and radially-dominate loading, and (c) between unloaded and circumferentially-dominate loading. (d) Comparison of the predicted DOA among all the states for the TVAL specimen of heart #1.

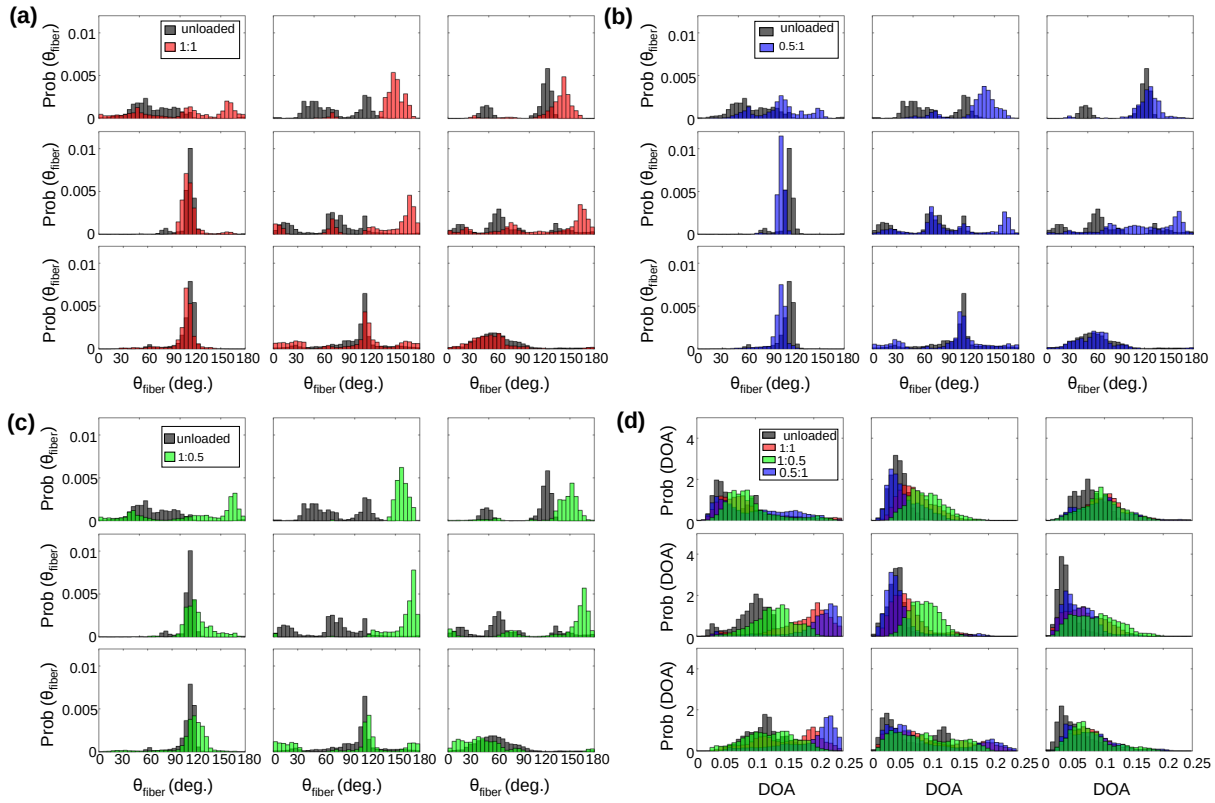

FIGURE 3.9 3x3 grid comparisons of the predicted θ_{fiber}: (a) between unloaded and equibiaxial loading, (b) between unloaded and radially-dominate loading, and (c) between unloaded and circumferentially-dominate loading. (d) Comparison of the predicted DOA among all the states for the TVPL specimen of heart #1.

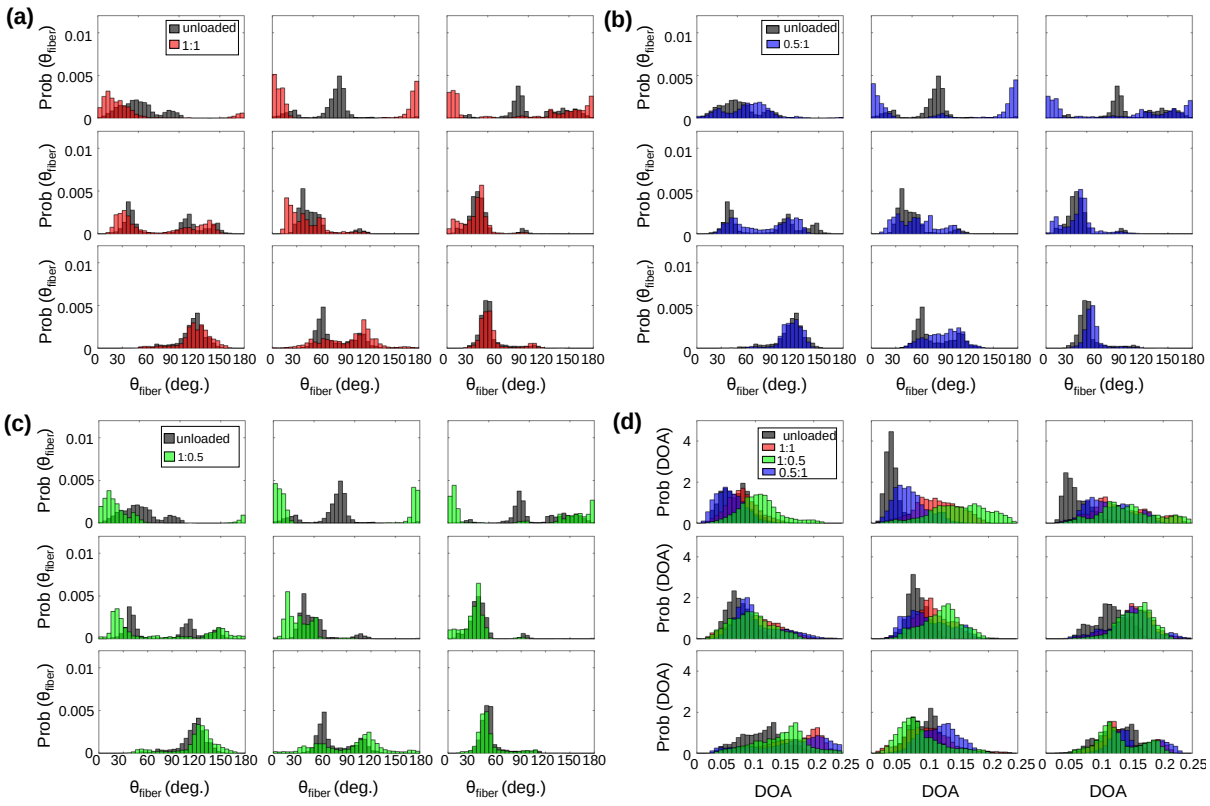

FIGURE 3.10 3x3 grid comparisons of the predicted θ_{fiber}: (a) between unloaded and equibiaxial loading, (b) between unloaded and radially-dominate loading, and (c) between unloaded and circumferentially-dominate loading. (d) Comparison of the predicted DOA among all the states for the TVSL specimen of heart #1.

4 QUANTIFICATION OF THE LOAD DEPENDENT COLLAGEN FIBER ARCHITECTURE IN MITRAL VALVE LEAFLETS

4.1 Overview

Despite the efforts placed on developing structural-based constitutive models for the mitral valve (MV), the load-dependent collagen fiber behavior has largely under studied in the context of organ-level function. These studies have primarily used small angle light scattering (SALS) to evaluate the changes in collagen fiber splay and orientation, but require the optical clearing which has been shown to damage the structural constituents (i.e., collagen) within the tissue [49, 70, 111]. Furthermore, glutaraldehyde fixation is needed to capture the microstructure at a deformed states due to extensive imaging times, inhibiting the evaluation of the collagen fiber architecture (CFA) *within the same tissue*. Second harmonic generation (SHG) has also been essential for understanding the individual collagen fiber kinematics, such as the intrinsic crimped state of the fibers, but can only resolve microstructural information at a micron-scale field of view (FOV) [51, 69]. Using an in-house opto-mechanical system, we previously demonstrated that the CFA in tricuspid valve leaflets varied across different porcine hearts, highlighting the importance of evaluating the effects of various mechanical loads within the same tissue [98, 103]. To overcome these shortcomings, polarized spatial frequency domain imaging (pSFDI) was integrated with a commercial biaxial testing system to non-destructively examine the CFA at physiological loads.

The objective of this study is to utilize the combined pSFDI and biaxial mechanical testing system to observe the load-dependent changes in the CFAs for the two MV leaflets. Elucidating the microstructural-mechanical relationship for these leaflets is important for informing multiscale models, and assessing the validity of fiber kinematic theories that greatly simplify the modeling efforts. These computational models will aid clinicians in further understanding the pathologies of MV disease and improve the current clinical therapeutics, such as replacement heart valves and annuloplasty rings [34, 38].

4.2 Methods

4.2.1 Tissue Acquisition and Preparation

Healthy porcine hearts ($n = 6$) were obtained from a local USDA-approved slaughterhouse (Chickasha Meat Company, Chickasha, OK). Each heart was dissected within 12 hours postmortem, and the mitral valve anterior (MVAL) and posterior (MVPL) leaflets were excised from valvular orifice. The MV leaflets were then stored at $-20\,^{\circ}$C for 12 hours prior to mechanical testing. This storage procedure was utilized based on previous investigations in our lab that suggest freezing-based storage methods do not significantly impact the observed mechanical properties of HV leaflet [112].

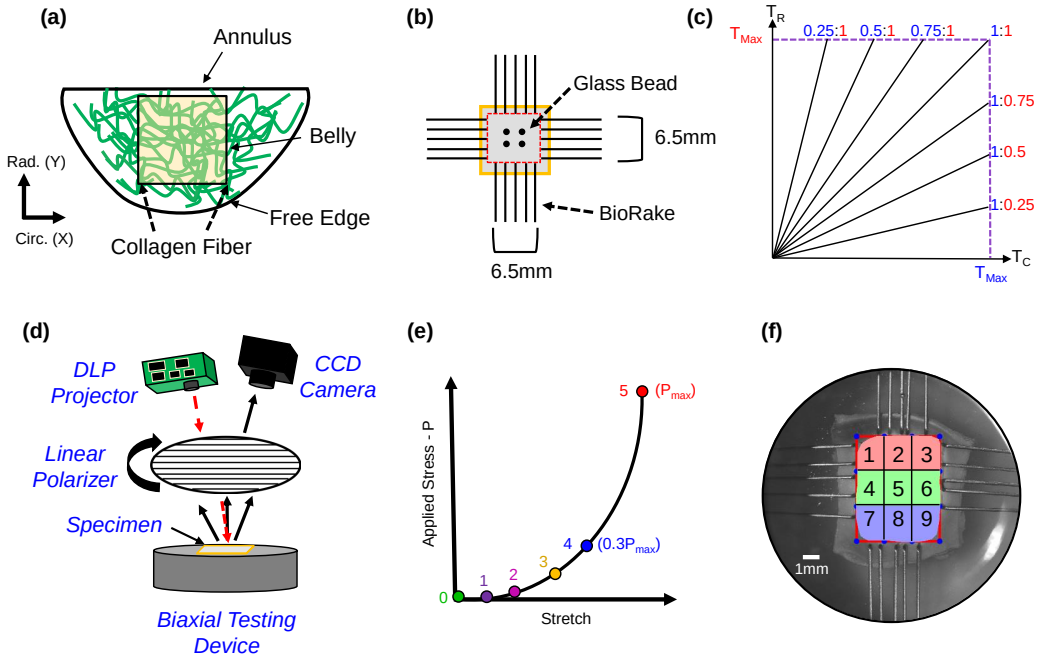

FIGURE 4.1 (a) A square specimen extracted from the center portion of the MV leaflet and (b) mounted to a commercial BioTester. (c) Biaxial testing was performed at equibiaxial tension and other relevant non-equibiaxial tension protocols. (d) Schematic of the combined pSFDI-biaxial instrument for quantification of tissue's collagen fiber architecture and resultant θ_{fiber} extraction at (e) the six loading points along the stress-stretch curve. (f) The entire ROI was separated into 9 sub-regions that correspond to the annulus (Regions 1-3), belly (Regions 4-6), and free edge regions (Regions 7-9).

4.2.2 Biaxial Mechanical Testing

The excised MV leaflets were thawed prior to biaxial testing in an in-house phosphate-buffered saline (PBS) at room temperature. After the specimen was thawed, the center portion of the leaflet was removed (Fig. 4.1a) and a non-contact laser displacement sensor (Keyence IL-030, Itaska, IL) was used to measure the thickness across three locations of the specimen to determine the average tissue thickness. The square specimen was then mounted to a commercial biaxial testing system (BioTester, CellScale, Canada, 1.5 N load cells) via BioRake tines that penetrate the tissue (Fig. 4.1b). An effective testing region of 6.5×6.5 mm and the tissue's circumferential (C) and radial (R) directions were aligned with the *X*- and *Y*-axes of the biaxial testing system. Glass beads ($300 - 500\,\mu$m) were placed in a 2×2 configuration on the center region of each specimen to serve as fiducial markers for quantifying the in-plane tissue strains using an data image correlation (DIC) technique provided by our biaxial testing software (Fig. 4.1b) [10]. Prior to mechanical testing, the specimen was submerged in a PBS bath at $37\,^{\circ}$C to maintain hydration throughout the duration of the test. Pre-conditioning, consisting of 10 loading/unloading cycles, was applied to the tissue with a target membrane tension of 150 N/m, correlating to the peak transvalvular pressure experienced by the MV leaflets during systole [113]. After pre-conditioning, displacement-controlled loading at varying physiologicially relevant tension protocols (T_{C}:T_{R}=1:0.75, 1:0.5, 1:0.25, 0.75:1, 0.5:1, 0.25:1) was used to capture a broad range of *in vivo* deformations (Fig. 4.1c). All protocols were repeated for three load/unloading cycles, and the load cell force readings and CCD images (15 Hz) were acquired throughout each biaxial testing procedure.

4.2.3 pSFDI-Based Collagen Fiber Microstructural Quantification

Following biaxial mechanical testing, the pSFDI system was integrated with the biaxial tester via vertical placement to capture the load-dependent changes in the collagen fiber orientation (θ_{fiber}) and alignment (DOA) throughout the specimen (Fig. 4.1d) [98, 103–105]. This reflectance-based technique relies on the birefringent optical response of collagen fibers, which alters the intensity of the back-scattered light dependent on the polarization and propagation of incident light [91, 92]. Following our previously established pSFDI-based imaging procedure, the incident cyan light (490 nm) with spatial frequency patterns was projected onto the tissue through an LED projector (Texas, In-

struments, Dallas, TX). A 5-megapixel CCD camera (Basler, Germany) was used to image each specimen, and the back-scattered intensity response was captured through a rotating linear polarizer (Thorlabs, Inc., Newton, NJ) at 37 distinct polarization states (i.e., 0° to 180°, 5° increments). This procedure was repeated for three linear phase shifts (0°, 120°, and 240°), corresponding to each spatial frequency pattern, and allows the rejection of diffusely scattered photons [100, 101]. Each MV leaflet was first evaluated using the pSFDI system at the deformation related to peak loading for all the biaxial tension protocols. In addition, six loading points of the stretch-stress curve from the last loading cycle of the equibiaxial tension protocol (T_{C}:T_{R}=1:1) were included in the collagen fiber architectural analysis (Fig. 4.1e):

(i) Loading Point 0: Tissue mounting configuration, Ω_0 (i.e., zero force and zero deformation)

(ii) Loading Points $1-3$: Three evenly spaced intermediate points between Loading Points 0 and 4.

(iii) Loading Point 4: 30% of the peak stension ($T_{\max}$)

(iv) Loading Point 5: Peak tension ($T_{\max}$)

The six loading points were determined through an intersection method, allowing the θ_{fiber} and DOA to be captured at equally distributed stress states prior to the transition point.

4.2.4 Statistical Analysis

Statistical analysis was performed in the R programming language (R Core Team, Toulouse, France) to determine the significance in the variation in the quantified collagen fiber orientation (θ_{fiber}) and DOA at the mounting and peak loading configurations for all biaxial testing protocols between the two MV leaflets. A non-parametric Mann-Whitney U test was used to compare the two MV leaflets to establish the presence of inter-valve variations. Comparisons were deemed significant when p-value < 0.05, inferring differences in the intrinisc and load-dependent microstrucural heavior between the two leaflets. Collagen fiber architecture results are reported as median$\pm$0.5$\times$IQR (Interquartile Range), whereas the tissue thickness and biaxial stretches are described as mean$\pm$SEM (Standard Error of the Mean).

4.3 Results

4.3.1 Tissue Thickness and Biaxial Mechanical Testing Results

The tissue thicknesses, measured prior to biaxial mechanical testing, were found as 0.74 ± 0.05 mm and 0.97 ± 0.04 mm for the MVAL and MVPL, respectively, with significant differences ($p = 0.007$) in thickness between the two leaflets. After preconditioning, the MVPL exhibited slightly larger post-preconditioning deformations in the both tissue directions ($\lambda_C : \lambda_R$=1.13 ± 0.02:1.31 ± 0.03) compared to the MVAL ($\lambda_C : \lambda_R$=1.09 ± 0.03:1.18 ± 0.03), however significant differences ($p = 0.016$) were observed between the two leaflets in the radial direction (Fig. 4.2a).

An anisotropic, non-linear membrane tension-stretch response was observed in both the tissue circumferential and radial directions for the MV leaflets (Fig. 4.2). In the low tension regime, each leaflet exhibited a near-linear compliant response before reaching a transition point at $0.3T_{\max}$, where increased tension yielded minimal tissue stretch. Several key findings regarding the biaxial mechanical response are reported as follows: (i) greater extensibility in the radial direction under equibiaxial tension (MVAL: λ_C=1.17 ± 0.03, λ_R=1.58 ± 0.06; MVPL: λ_C=1.28 ± 0.03, λ_R=1.74 ± 0.10, Fig. 4.2b); (ii) under non-equibiaxial loading (T_C:T_R=1:0.75, 1:0.5, 1:0.25, 0.75:1, 0.5:1, 0.25:1), the investigated MV leaflets exhibited a larger stretch in the radial direction, regardless of the direction with the dominant load; (iii) directional coupling was present between the two tissue directions. For example, under circumferentially-dominant loading (T_C:T_R=1:0.75, 1:0.5, 1:0.25), a decrease in radial tension resulted in an increase in circumferential tissue stretch (Fig. 4.2c); (iv) radially dominant loading (T_C:T_R=0.75:1, 0.5:1, 0.25:1) resulted in the largest radial tissue stretches among all loading protocols (Fig. 4.2d); (V) Finally, under all biaxial tension protocols, the MVPL was the most compliant in the circumferential and radial directions compared to its MVAL counterpart.

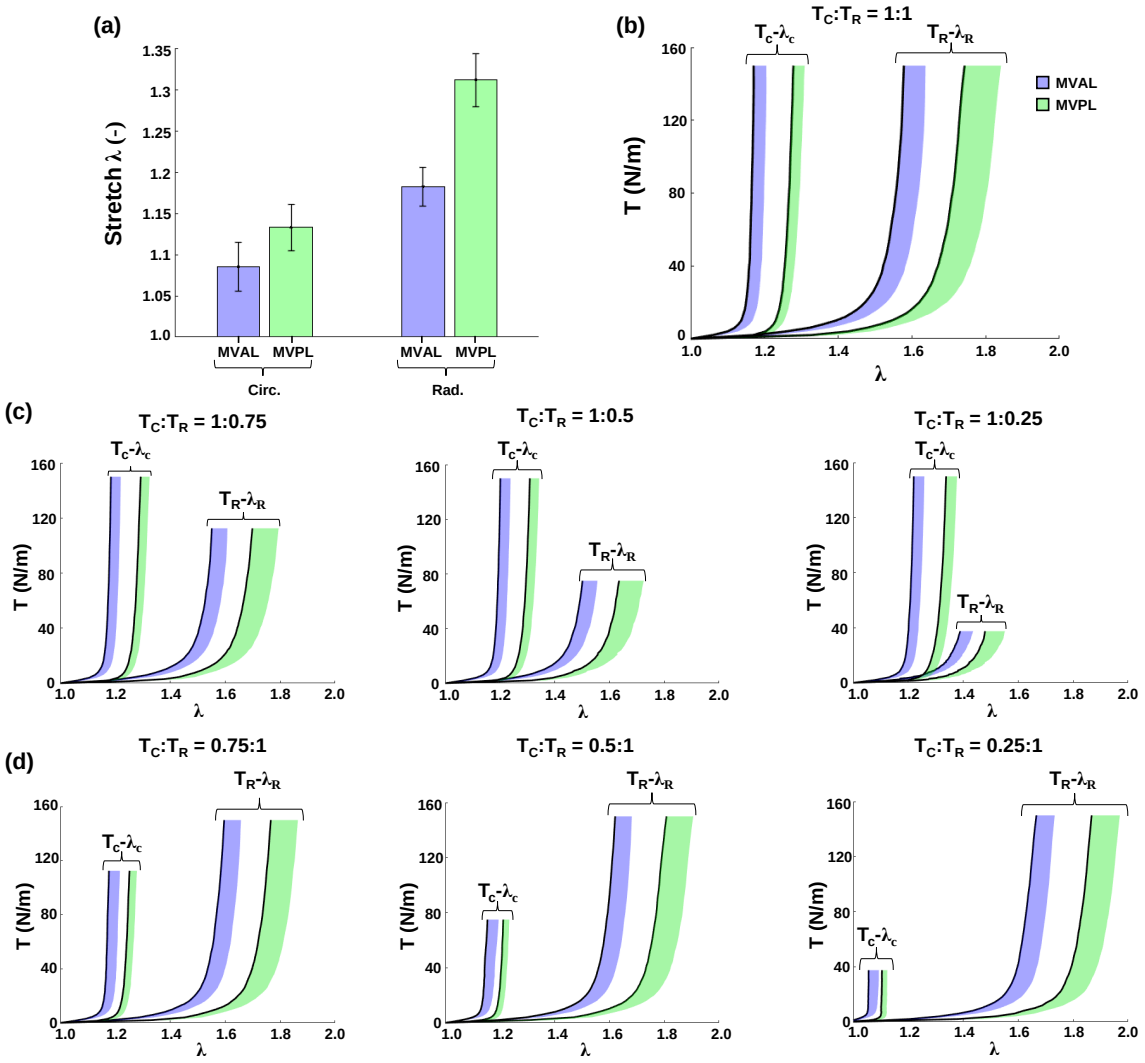

FIGURE 4.2 (a) PPC deformations and membrane tension (T) versus tissue stretch (λ) at (b) equibiaxial loading, (c) circumferentially-dominant loading protocols, and (d) radially-dominant loading protocols for each MV leaflet.

4.3.2 Local and Bulk-Tissue Collagen Fiber Architecture Quantifications

The MV leaflets displayed a circumferentially-oriented collagen fiber architecture prior to biaxial testing, consistent with previously reported results from Lee *et al.* and Liao *et al.* (Table 4.1). The MVAL and MVPL also shared a relatively similar collagen fiber orientation at the mounting configuration, although the MVPL had slightly more collagen

fiber alignment. A 3×3 regional analysis of the MV leaflet microstructure corroborated the bulk tissue findings, where the three distinct region of the MV leaflets (i.e., Annulus, Belly, and Free Edge) showed a preferred fiber direction in the circumferential direction (Table 4.1). The greatest degree of fiber alignment was observed in the belly regions of each leaflet (Region 6 for MVAL, Region 5 for MVPL), whereas the smallest DOA values were found in Region 7, near the free edge, for both the MVAL and MVPL. See Fig. 4.1f for more information regarding the 3×3 regional analysis for each MV specimen.

TABLE 4.1 Baseline values for the collagen fiber orientation (θ_{fiber}) and DOA prior to pre-conditioning and biaxial testing for the entire ROI and each 3x3 grid regions. Values are reported as median±0.5*IQR.

	MVAL		MVPL	
Region	θ_{fiber}	DOA	θ_{fiber}	DOA
Entire ROI	171.8°±6.4°	0.071±0.003	175.2°±12.4°	0.072±0.003
1	6.2°±15.1°	0.058±0.007	165.8°±28.2°	0.058±0.010
2	178.7°±10.8°	0.068±0.014	3.0°±11.7°	0.075±0.006
3	172.4°±8.6°	0.071±0.006	150.1°±30.6°	0.068±0.008
4	5.5°±17.5°	0.058±0.003	0.9°±24.9°	0.061±0.008
5	176.1°±8.9°	0.070±0.008	158.5°±27.8°	0.082±0.008
6	159.8°±8.2°	0.079±0.008	143.4°±15.7°	0.075±0.009
7	4.6°±14.8°	0.056±0.001	9.0°±35.3°	0.046±0.007
8	173.5°±13.6°	0.068±0.005	138.6°±23.6°	0.066±0.007
9	170.5°±6.2°	0.071±0.003	173.9°±14.3°	0.080±0.003

Across all biaxial testing protocols, there were no significant differences in collagen fiber orientation between the MVAL and MVPL specimens. At equibiaxial tension, the MV leaflets maintained a predominantly circumferentially aligned CFA with respect to the mounting configuration, although the quantified DOA increased by 14.1% and 19.4% for the MVAL and MVPL, respectively. For circumferentially-dominant loading protocols, decreasing the radial tension led to further reorientation of the CFA towards the circumferential axis (Table 4.2). Although this preferred fiber orientation was maintained, the collagen fibers became more aligned with each 25% reduction in radial tension and reached a maximum DOA (MVAL: 0.084 ± 0.012; MVPL:0.095 ± 0.006) at the most dominant circumferential load (T_{C}:T_{R}=1:0.25). A similar trend was found for

radially-dominant loading, where each 25% reduction in circumferential tension led to an incremental increase in DOA and the greatest alignment (MVAL: 0.083 ± 0.009; MVPL:0.090 ± 0.005) at the most dominant radial loading protocol (T_C:T_R=0.25:1). Furthermore, with each reduction in circumferential tension, the MV leaflets' CFA reoriented towards the radial axis, the direction of greatest applied loading (Table 4.2). The MVPL exhibited the largest changes in θ_{fiber} and greater DOA values for all biaxial testing protocols, although there were no significant differences in fiber alignment between the two MV leaflets.

TABLE 4.2 The quantified collagen fiber orientation (θ_{fiber}) and DOA at peaking loading for all biaxial testing protocols. Values are reported as median±0.5*IQR.

	MVAL		MVPL	
Loading Ratio	θ_{fiber}	DOA	θ_{fiber}	DOA
$T_C : T_R$=1:1	14.2°±5.5°	0.081±0.009	152.8°±44.7°	0.086±0.003
$T_C : T_R$=1:0.75	16.2°±6.2°	0.079±0.011	66.9°±53.7°	0.087±0.004
$T_C : T_R$=1:0.5	18.5°±5.4°	0.080±0.012	56.6°±54.7°	0.090±0.006
$T_C : T_R$=1:0.25	18.2°±5.4°	0.084±0.012	25.7°±14.5°	0.095±0.006
$T_C : T_R$=0.75:1	10.7°±5.8°	0.079±0.011	143.6°±39.2°	0.086±0.002
$T_C : T_R$=0.5:1	12.5°±52.1°	0.081±0.010	139.3°±49.5°	0.087±0.003
$T_C : T_R$=0.25:1	145.8°±12.1°	0.083±0.009	134.5°±9.3°	0.090±0.005

Representative pSFDI-quantified CFA results from individual MVAL and MVPL specimens are shown at the end of the chapter in Fig. 4.5 and Fig. 4.6, respectively. For the representative MVAL specimen, a preferred circumferential orientation ($140.4°\pm42.3°$) was maintained under equibiaxial tension, however there were discrete differences in the 9 regions of the leaflet. For example, the median θ_{fiber} of the three belly regions indicated fibers with a preferred circumferential orientation ($143.3°\pm3.4°$), whereas the annulus ($133.0°\pm14.0°$) and free edge regions ($132.6°\pm15.2°$) were comprised of more radially oriented collagen fibers (Fig. 4.5a, Middle Row). The also DOA varied across the specimen and was the highest in the free edge regions (0.084 ± 0.014), compared to the belly (0.070 ± 0.005) and annulus (0.066 ± 0.010) regions under equibiaxial loading (Fig. 4.5a, Bottom Row). Both non-equibiaixal protocols showed similar differences in the 9 regions in the quantified collagen fiber orientation and the DOA metrics (Fig. 4.5b,c). For all MV specimens, the collagen fiber orientation varied spatially across the tissue and each

region showed CFA reorientation towards the direction of greatest applied loading (Table 4.3). Additionally, the DOA in each region was dependent on the loading protocol, evident of greater alignment in the annulus and belly regions under circumferentially-dominant loading versus the greatest alignment in the free edge regions under radially-dominant loading (Table 4.3). The free edge contained the most consistently aligned regions (DOA=0.078-0.091) for each biaxial protocol, followed by the annulus (DOA=0.062-0.096) and belly regions (DOA=0.060-0.098) for all MV specimens (Table 4.3).

TABLE 4.3 3x3 Regionally quantified collagen fiber orientation (θ_{fiber}) and DOA at various biaxial testing protocols for the MVAL specimens. Values are reported as Median±0.5*IQR

	MVAL					
	T_C:T_R=1:1		T_C:T_R=1:0.25		T_C:T_R=0.25:1	
Region	θ_{fiber}	DOA	θ_{fiber}	DOA	θ_{fiber}	DOA
1	27.8°±7.4°	0.065±0.009	33.4°±7.8°	0.070±0.015	14.2°±42.3°	0.062±0.011
2	16.7°±12.5°	0.077±0.014	21.6°±6.2°	0.088±0.022	132.8°±56.1°	0.082±0.012
3	20.4°±4.5°	0.096±0.025	27.8°±6.3°	0.096±0.029	160.3°±14.4°	0.086±0.011
4	84.5°±61.9°	0.060±0.004	28.3°±10.0°	0.069±0.004	132.1°±53.8°	0.061±0.017
5	12.9°±6.2°	0.084±0.007	14.9°±3.0°	0.098±0.015	140.9°±54.6°	0.081±0.011
6	11.2°±50.5°	0.073±0.003	13.0°±2.4°	0.078±0.008	161.3°±13.8°	0.077±0.009
7	80.9°±60.7°	0.087±0.012	23.9°±50.7°	0.086±0.005	144.0°±14.4°	0.088±0.018
8	76.5°±77.8°	0.089±0.007	15.5°±53.7°	0.088±0.014	148.1°±23.9°	0.089±0.004
9	159.8°±29.8°	0.083±0.008	134.6°±46.5°	0.078±0.007	118.1°±17.6°	0.091±0.013

We noticed similar variations in collagen fiber orientation across the 9 sub-regions for the MVPL representative specimen (Fig. 4.6a). More importantly, the CFA reoriented towards the direction of greatest applied loading for the two non-equibiaxial protocols (Fig. 4.6b,c). This observation was consistent for all MVPL specimens, where deviation towards the dominant loading axis was consistent throughout all 9 regions (Table 4.4). For instance, under circumferenially-dominant load the annulus and belly regions were well aligned with the tissue circumferential direction (θ_{fiber}= $20.6°-38.0°$), and rotated towards the radial direction after reduced circumferential tension (θ_{fiber}= $114.0°$-$139.2°$). Similar to their MVAL counterpart, the annulus and belly regions had the highest degree of fiber alignment under circumferentially-dominant loading (DOA=0.087-0.106), while the free edge was the most aligned under radially-dominant loading (DOA=0.087-0.089). In contrast, the annulus regions had the largest quantified collagen fiber align-

ment (DOA=0.081-0.103) within the specimen followed by the belly (DOA=0.065-0.106) and free edge regions (DOA=0.069-0.089) for all biaxial testing protocols (Table 4.4).

TABLE 4.4 3x3 Regionally quantified collagen fiber orientation (θ_{fiber}) and DOA at various biaxial testing protocols for the MVPL specimens. Values are reported as Median±0.5*IQR

	MVPL					
	T_C:T_R=1:1		T_C:T_R=1:0.25		T_C:T_R=0.25:1	
Region	θ_{fiber}	DOA	θ_{fiber}	DOA	θ_{fiber}	DOA
1	110.0°±44.4°	0.081±0.014	23.9°±22.9°	0.094±0.011	115.9°±18.3°	0.081±0.010
2	64.1°±38.1°	0.083±0.007	37.1°±12.3°	0.101±0.015	114.0°±21.5°	0.093±0.007
3	54.9°±60.5°	0.093±0.006	38.0°±61.4°	0.103±0.013	139.2°±12.7°	0.095±0.019
4	50.8°±29.4°	0.065±0.007	29.7°±11.0°	0.087±0.010	133.3°±17.2°	0.076±0.004
5	45.5°±48.3°	0.088±0.010	20.6°±9.5°	0.104±0.007	133.7°±11.6°	0.091±0.007
6	63.1°±59.9°	0.088±0.012	32.4°±58.3°	0.106±0.012	136.1°±9.0°	0.087±0.017
7	78.4°±64.1°	0.069±0.019	87.7°±72.4°	0.082±0.018	140.0°±2.3°	0.089±0.011
8	137.2°±52.9°	0.073±0.010	76.3°±63.8°	0.075±0.012	132.6°±2.9°	0.085±0.016
9	119.2°±9.9°	0.077±0.006	116.8°±21.0°	0.068±0.004	121.7°±4.7°	0.087±0.015

4.3.3 Loading-Dependent Changes in the Collagen Fiber Architecture

Representative pSFDI-quantified load-dependent CFA results from individual MVAL and MVPL specimens are shown in Fig. 4.3 and Fig. 4.4, respectively. We noticed that each specimen had a preferred collagen fiber orientation in the circumferential direction within the toe region (Loading Point 1) of the equibiaxial tension vs. stretch curve see the schematic definition in Fig. 4.1c. Minimal changes in θ_{fiber} occurred between the toe region and the transition (Loading Point 4) and high-tension regions (Loading Point 5), although substantial changes in collagen fiber alignment were observed. In the toe region, the collagen fibers were slightly aligned in the MV specimens (MVAL: 0.076 ± 0.017; MVPL: 0.073 ± 0.014), however there was substantial realignment at the transition region (MVAL: 0.092 ± 0.028; MVPL: 0.087 ± 0.022) of the membrane tension vs. stretch curve. Within the high-tension region, the CFA became more aligned (MVAL: 0.094 ± 0.028; MVPL: 0.089 ± 0.022) compared to the transition region, reaching maximum alignment at peak equibiaxial loading.

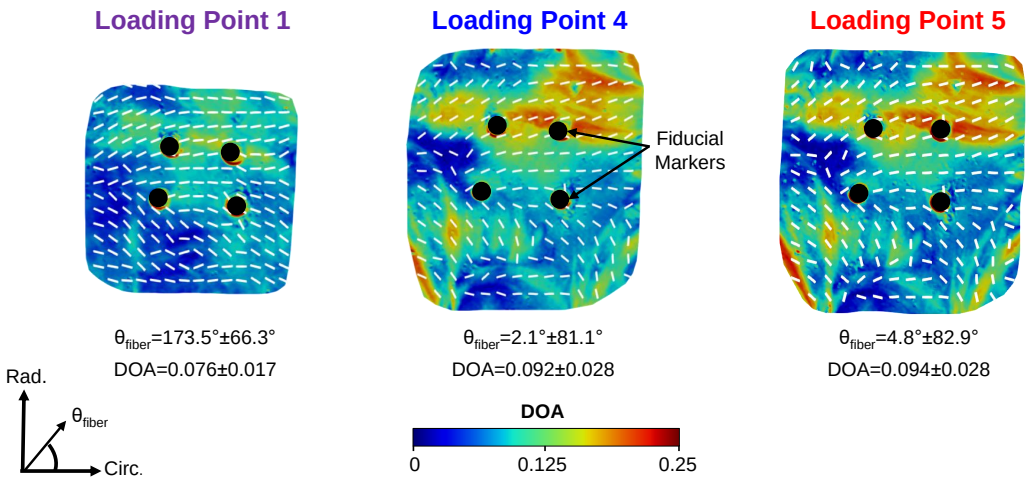

FIGURE 4.3 Incremental changes in the collagen fiber orientation and DOA were examined for an MVAL specimen at the toe, transition, and high-tension regions of the tension vs. stretch curve for equibiaxial loading. Collagen fiber orientation and DOA are reported as median$\pm 0.5\times$IQR.

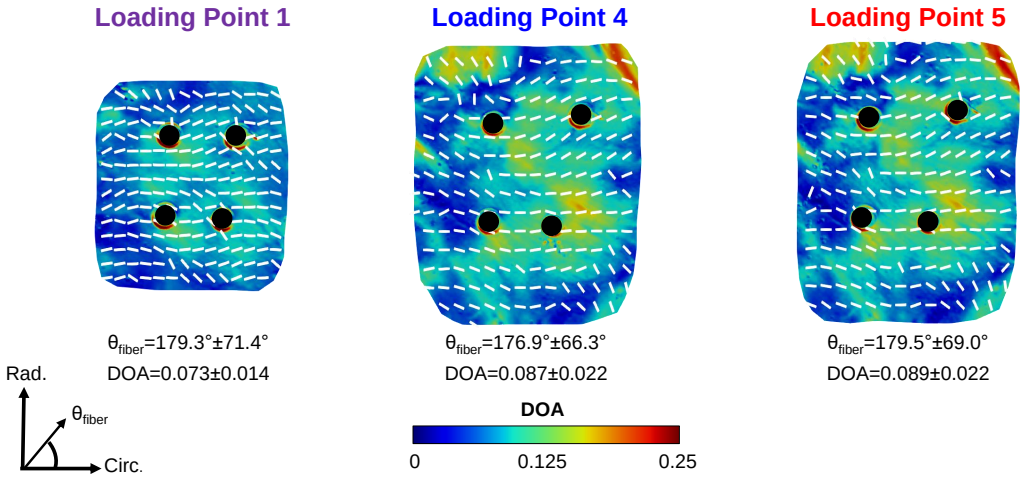

FIGURE 4.4 Incremental changes in the collagen fiber orientation and DOA were examined for an MVPL specimen at the toe, transition, and high-tension regions of the tension vs. stretch curve for equibiaxial loading. Collagen fiber orientation and DOA are reported as median$\pm 0.5^*$IQR.

At Loading Point 0, the MVAL and MVPL specimens had predominantly circumferential collagen fiber networks (MVAL: $171.8°\pm 6.4°$, MVPL: $175.2°\pm 12.4°$). Notable changes in the quantified θ_{fiber} and DOA were observed with incremental loading, with several

key findings summarized as follows. First, when comparing sequential loading points, we found the CFAs in the MV leaflet to reorient towards the radial axis (CCW) until Loading Point 5 (Table 4.5). The difference in θ_{fiber} for sequential loading points was the largest between Loading Point 2 and Loading Point 3 for the MVAL ($+2.9°\pm3.1°$), and between Loading Point 4 and Loading Point 5 for the MVPL ($+2.9°\pm3.14°$). Second, the difference in θ_{fiber} when comparing non-sequential loading points was between Loading Point 0 and Loading Point 5 for both the MVAL ($+8.9°\pm7.4°$) and MVPL ($+11.1°\pm9.8°$) specimens.

TABLE 4.5 Difference in the quantified collagen fiber orientation (θ_{fiber}) between two equibiaxial tension states of the 5 loading points for the MV leaflets. Values are reported as mean±SEM

Loading Point	Loading Point as reference (baseline)				
	0	1	2	3	4
MVAL					
1	0.5°±0.9°	-	-	-	-
2	3.1°±3.4°	2.6°±2.8°	-	-	-
3	6.0°±6.3°	5.5°±5.7°	2.9°±3.1°	-	-
4	8.1°±6.9°	7.6°±6.3°	5.0°±3.8°	2.1°±1.0°	-
5	8.9°±7.4°	8.4°±6.8°	5.8°±4.4°	2.9°±1.6°	0.9°±0.6°
MVPL					
1	1.4°±1.9°	-	-	-	-
2	0.7°±2.7°	0.5°±1.6°	-	-	-
3	4.5°±6.0°	3.1°±5.7°	3.7°±4.4°	-	-
4	8.4°±8.4°	7.0°±8.1°	7.7°±7.1°	4.0°±4.1°	-
5	11.1°±9.8°	9.9°±9.6°	10.9°±9.9°	11.1°±9.6°	8.3°±8.9°

†The positive changes in the fiber orientation (θ_{fiber}) denote the counterclockwise reorientation,whereas the negative changes represent the clockwise reorientation.

Third, between each sequential loading point, the CFA became more aligned and followed similar percent changes between each loading point for both the MVAL and MVPL specimens (Table 4.6). Although the changes in DOA were within similar range, the MVAL had the largest percent change between Loading Point 1 and Loading Point 2 ($7.5\%\pm1.9\%$), with similar changes between Loading Point 2 and Loading Point 3 for the MVPL ($7.5\%\pm2.0\%$). Finally, for all non-sequential loading points, the greatest changes in DOA occurred between Loading Point 0 and Loading Point 3 for the

MVAL ($19.0\%\pm5.4\%$), and between Loading Point 0 and Loading Point 4 for the MVPL ($20.4\%\pm4.4\%$).

TABLE 4.6 Percent change in the quantified DOA between two equibiaxial tension states of the 5 loading points for the MV leaflets. Values are reported as mean±SEM

Loading Point	Loading Point as reference (baseline)				
	0	1	2	3	4
MVAL					
1	3.1±1.7%	-	-	-	-
2	11.0±3.2%	7.5±1.9%	-	-	-
3	19.0±5.4%	15.3±4.1%	7.0±2.0%	-	-
4	16.8±4.9%	13.9±3.8%	5.8±2.4%	1.4±1.8%	-
5	16.4±4.9%	12.8±3.6%	4.8±2.4%	0.4±2.1%	0.02±1.0%
MVPL					
1	2.6±1.9%	-	-	-	-
2	9.3±3.2%	6.4±1.4%	-	-	-
3	17.5±4.5%	14.4±3.2%	7.5±2.0%	-	-
4	20.4±4.4%	17.3±3.4%	10.1±2.3%	2.5±0.5%	-
5	18.3±5.2%	15.2±4.3%	8.2±3.2%	0.6±1.3%	0.05±0.07%

4.4 Discussion

4.4.1 Biomechanical Observations

We found that the MVAL and MVPL specimens exhibited a non-linear, anisotropic mechanical response and were more compliant in the tissue radial direction under all biaxial loading protocols, consistent with investigations from Grashow *et al.* and May-Newman *et al.* [46, 54]. Peak circumferential tissue stretches for the MVAL at equibiaxial loading were found to be in good agreement with biaxial testing studies emulating the same membrane tension (150 N/m), however slightly larger peak radial stretches were observed within the present study [114, 115]. In comparison, the peak stretches for the MVPL were larger than those reported by Jett *et al.*, however the peak load at equibiaxial tension was lower then targeted tension in our biaxial testing framework [10]. Jett *et al.* also reported larger tissue stretches for the MVPL compared to the MVPL in the

radial direction for various loading protocols (T_C:T_R=1:1, 1:0.5, 0.5:1), whereas our findings revealed the MVPL to be more extensible in both tissue directions for equibiaxial and all non-equibiaxial tension. Furthermore, a larger focus has been placed on characterizing the mechanical properties of the MVAL compared to the MVPL, primarily due to its conveniently larger belly region, limiting comparisons with previous studies [46, 54, 55, 70, 81, 111]. Overall, these findings corroborate the current understanding of tissue-level mechanics in the MV leaflets, yet connecting these macroscopic tissue behaviors to the local and bulk-tissue microstructural changes has yet to performed through pSFDI-based collagen microstructural imaging. Relating these biomechanical trends to the CFA orientation and realignment will aid in elucidating the load-dependence of the collagenous microstructure of MV leaflets when subjected to *in vivo* loading conditions.

4.4.2 Collagen Fiber Architecture Changes

From the pSFDI-based collagen microstructural quantifications, we examined load dependent changes in the CFA for each MV leaflet. At the mounting configuration, it was revealed that the collagen fiber orientation within the MV leaflets was spatially-varied, but had a preferred bulk-tissue collagen fiber orientation near the circumferential axis (Table 4.1). This slight deviation from the preferred axis of orientation may be explained by the splay or the dispersion of the collagen fibers, which has been previously observed in MV leaflets [49, 69]. When subjected to biaxial tension, the CFA orientation and alignment changed heterogeneously throughout the tissue, dependent on the direction of dominant loading (Fig. 4.2, Fig. 4.5). Biaxial loading along the preferred fiber direction led to the greatest degree of fiber alignment and miniscule changes in θ_{fiber}, owing to the intrinsic circumferential orientation. This increase in fiber alignment is primarily due to the circumferential lengthening of the collagen fibers from their crimped configuration, a well-known phenomenon that occurs in collagenous soft tissues [49]. Preferential loading in the radial direction resulted in slight radial reorientation, although a predominantly circumferential orientation was maintained for both leaflets (Table 4.2). Overall, these findings are consistent with our previous investigations of the load-dependent CFA in tricuspid valve leaflets, as well as characterizations of the MV leaflets using micro-scale imaging techniques [98, 103].

4.4.3 Relating Tissue Biomechanics to Collagen Fiber Kinematics

The tissue-level mechanical behavior observed in the HV leaflets, such as material anisotropy, non-linearity, and spatial variations, has attempted to be explained through various collagen fiber kinematic theories [69, 116, 117]. Moreover, each region of the membrane tension-stretch curve is a direct reflection of the underlying load-dependent changes in the collagen microstructure [118, 119]. Prior to loading (Loading Point 0), the MV leaflets had a preferred fiber orientation along the circufmerential axis and miniscule alignment, which can be explained by the intrinsic collagen fiber crimp [49, 69]. As applied tension increased in the toe region of the biaxial curve (Loading Points 1-3), the collagen fibers were recruited and circumferentially lengthened, reducing the dispersion throughout the specimen. This reduction in dispersion for the toe region was evident from the greatest changes in DOA, which occurred between Loading Point 1 and Loading Point 2 for the MVAL ($7.5\% \pm 1.9\%$), and Loading Point 2 and Loading Point 3 for the MVPL ($7.5\% \pm 2.0\%$). The collagen fiber alignment continued to increase up until the transition region (Loading Point 4), nearing full recruitment after circumferential lengthening takes place. Beyond this transition zone at $0.3T_{\max}$, the CFA remained relatively unchanged, corresponding to the rapid stiffening and non-linear mechanical behavior in the high-tension regime (Loading Points 4-5). Furthermore, the abrupt non-linear transition and higher circumferential stiffness in the mechanical response of the MV leaflets can be explained by the CFA's preferred fiber direction throughout each loading protocol, contributing to the tissue's mechanical anisotropy [78, 120]. This mechanical anisotropy decreased with each reduction in radial tension, reducing the radial extensibility as fewer fibers are recruited towards the perpendicular axis. A reduction in circumferential tension, however, led to greater anisotropy within the tissue, as a greater fiber recruitment and reorientation is needed to overcome the radially-dominant loading. These assertions regarding the collagen fiber kinematics are in good agreement with other microstructural-mechanical studies for heart valve leaflets [51, 52], and identifying these key load-dependent changes in the MV leaflet CFA can help provide microstructural context to the tissue mechanical behavior. Further, a deeper comprehension of these complex interactions are essential for improving the current understanding of MV disease and informing computational models that simulate *in vivo* function.

4.4.4 Study Limitations and Future Work

Although this integrated opto-mechanical approach overcomes many of the limitations exhibited by other optical imaging techniques, there exists several limitations within the current study. First, displacement-controlled biaxial testing methods were used emulate the physiological loading environment experienced *in vivo*. This was performed by determining the displacement of each specimen at the targeted membrane tensions, but due to the stress relaxation of the tissue when determining the peak specimen size, there were slight reductions in target membrane tension values. Second, the BioRake tine-based biaxial testing approach may create shear deformations in each specimen. Therefore, this limitation was overcome by aligning the tissue circumferential and radial axes with the x- and y-axis of the biaxial testing system to mitigate the potential of shear-induced changes. Third, for pSFDI-based imaging the specimens were displaced to the deformation that corresponded to each loading point. Although the quantified θ_{fiber} and DOA may be close to the expected CFA behavior at the relative target tension, stress-relaxation of the tissue prohibited the definitive quantification of these parameters at each loading point. Fourth, in some cases there were small mispredictons in the collagen fiber orientation and DOA across the specimen due to surface defects (i.e., bubbles) and tissue folding. However, in this work, each MV leaflet was mounted to the biaxial testing system and these surface defects were removed from the PBS path. Likewise, pSFDI quantifications were made at each individual pixel, therefore mispredictions may not influence the bulk tissue orientation and alignment extracted for each leaflet. Finally, the DOA metric is a good indicator of CFA alignment, although it does not capture the collagen fiber crimp periods or structural alignment typically derived from other collagen-based imaging modalities.

The most immediate extension of this work is the validation of the affine fiber kinematic theory. Existing structural constitutive models typically aim to relate the local collagen fiber changes to the macroscopic tissue deformation, in what is known as the ”affine” assumption. This assumption greatly simplifies the computational efforts in predicting the collagen fiber reorientation with respect to the deformation gradient tensor, and has been evaluated for MVAL specimens, except using micro-scale imaging techniques [69, 116]. The bulk-tissue and pixel-wise quantifications using the pSFDI-based approach shows potential in more accurately evaluating this theory for the MV

leaflets, but also for other heart valve specimens where further understanding of the microstructural-mechanical relationship is needed. Further investigations would also benefit from employing the SFDI portion of the pSFDI-based system to evaluate the *transmural* changes in collagen fiber orientation and alignment, as it has previously been shown that the layer-specific mechanical properties contribute to the bulk tissue response in other heart valve leaflets [9, 71]. Therein, these layer-specific quantifications would further improve the accuracy of current structural-based models, which may oversimplify the contribution of the collagen fiber architecture to the macroscopic mechanical response. Incorporation of both of these factors into current models not only warrants future *in silico* investigations of the complex collagen microstructure, but can be used in surgical planning and evaluation of current therapeutics in the case of mitral valve regurgitation [121, 122].

4.5 Conclusion

This study effectively quantified the local and bulk-tissue collagen fiber orientation and alignment within the MV specimens, *for the first time*, using an integrated non-destructive opto-mechanical system. Overall, the MV leaflets exhibited a spatially-varied microstructure that dynamically reorients and realigns heterogenously in response to applied loading. Linking the tissue-level mechanics to the load-dependent CFA changes in the MV leaflets is essential for developing high fidelity constitutive models that accurately capture the complex interactions within the tissue. These enhancements in current modeling frameworks would elucidate the individual organ-level function and disease pathologies associated with MV, but could be used for patient-specific surgical planning and evluation of therapeautic options. Preoperative guidance to ensure the efficacy of MV repair would be of great benefit, mitigating the risk of potential re intervention in the future. As part of our future investigations, we plan to evaluate the affine fiber kinematic theory for the MV leaflets, and develop a structural-constitutive models to capture the unique interaction between physiological loading and collagen fiber remodeling.

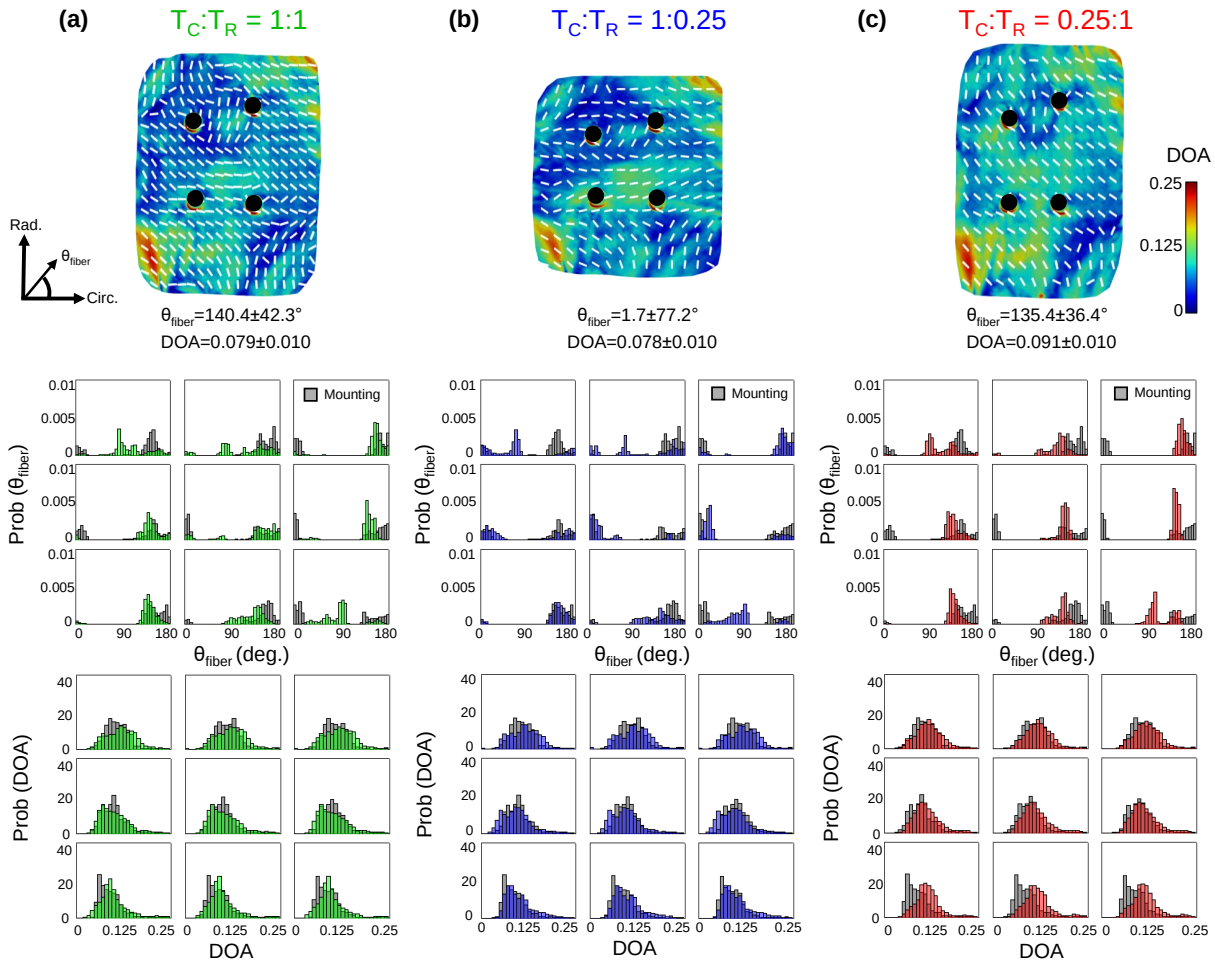

FIGURE 4.5 Bulk tissue characterizations and 3x3 grid comparisons of the predicted θ_{fiber} and DOA for a representative MVAL specimen: (a) between unloaded and equibiaxial loading, (b) between unloaded and circumferentially-dominate loading, and (c) between unloaded and radially-dominate loading. Collagen fiber orientation and DOA are reported as median$\pm 0.5^{*}$IQR.

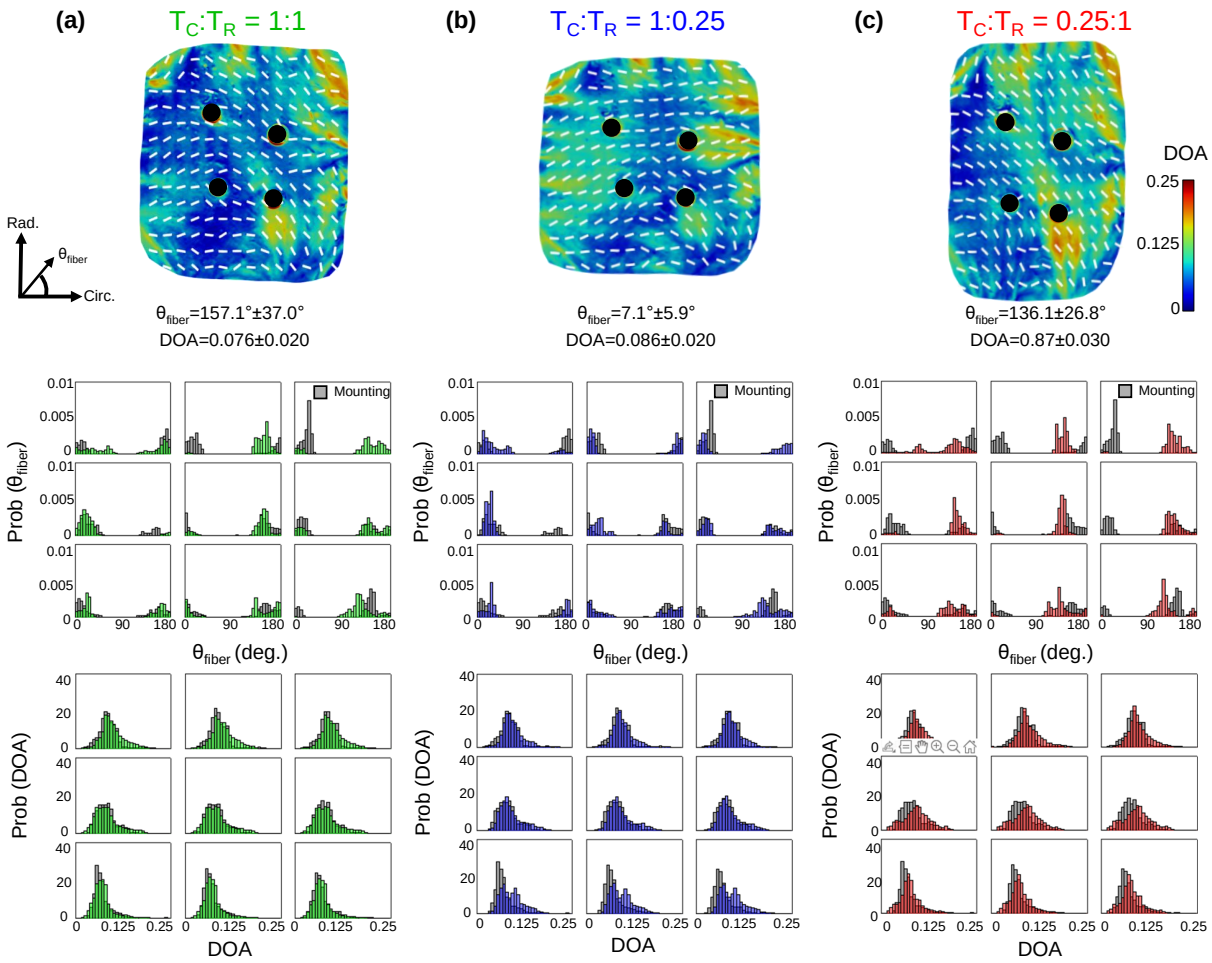

FIGURE 4.6 Bulk tissue characterizations and 3x3 grid comparisons of the predicted θ_{fiber} and DOA for a representative MVPL specimen: (a) between unloaded and equibiaxial loading, (b) between unloaded and circumferentially-dominant loading, and (c) between unloaded and radially-dominate loading. Collagen fiber orientation and DOA are reported as median$\pm 0.5^*$IQR.

5 AN INVESTIGATION OF THE MECHANICAL AND MICROSTRUCTURAL PROPERTIES OF PORCINE SEMILUNAR HEART VALVE CUSPS

5.1 Overview

Research efforts have been made over the past 30 years to characterize the tissue mechanics and collagen fiber architecture of the AV and PV cusps [13, 15, 58–66, 83, 85, 87]. These studies have shown that the SHV cusps exhibit anisotropic material properties, with uniquely distinct collagen fiber distributions between the two valves. Although valuable insight has been provided into the collagen fiber architectural changes under applied stresses, these experimental observations were made using *destructive* imaging techniques, such as small-angle light scattering (SALS) that requires tissue fixation to evaluate the microstructure along with a long acquisition time (1-2 hrs) [85, 87]. Chemical fixation of the tissue specimen with a glutaraldehyde solution at peak loading induces cross-linking of the collagen fiber network, inhibiting the evaluation of the dynamic changes in the collagen microstructure within the same specimen in response to different mechanical loads [61]. High-fidelity computational models rely on the experimental data collected, and, therefore, the ability to connect tissue-level mechanics to the microstructural collagen fiber changes within the same specimen is of a great importance. These quantification studies can eliminate the discrepancies between the valves of different microstructural compositions, instead of assuming uniformity in characteristics for all tested specimens. To address these shortcomings, polarized spatial frequency domain imaging (pSFDI) was used to quantify the collagen fiber architectural changes with a larger field of view (FOV) and faster imaging times (< 1 min), without the need for using chemical fixatives or tissue modifications.

Thus, the objective of this work is to characterize the changes in the collagen fiber architecture under various physiologically relevant loading conditions for both the AV and the PV cusps. Comparisons in the observed mechanical properties and the orientation and alignment of the collagen fibers will be made between the two SHVs to assess their distinct differences, reflecting their different anatomical positioning and physiolog-

ical loading environment. Our findings not only can aid in the refinement of the current microstructure-informed computational models, but also can provide potential insight into the efficacy of the Ross procedure as widely used in patients with AV failures [90]. In addition, the obtained tissue mechanics-microstructure relationship, together with our experimental approach, can improve the development of tissue-engineered constructs as a potential alternative for pediatric patients with congenital heart defects and related valvular abnormalities.

5.2 Methods

5.2.1 Tissue Preparation

Twelve porcine hearts ($n = 12$, 80-140 kg of weight, 1-1.5 years of age) were obtained from a local USDA-approved abattoir (Chickasha Meat Company, Chickasha, OK). Each heart was dissected, and the three AV cusps (LCC: left coronary cusp, NCC: non-coronary cusp, and RCC: right coronary cusp) and the three PV cusps (LC: left cusp, AC: anterior cusp, and RC: right cusp) were extracted from the aortas and pulmonary arteries, respectively. The AV and PV cusps were then briefly stored at $-20\,^{\circ}$C prior to mechanical testing within 6-12 hrs.

5.2.2 Biaxial Mechanical Testing

Prior to biaxial mechanical testing, the excised SHV specimens thawed in an in-house phosphate-buffered saline (PBS) solution at room temperature. Once thawed, the belly region of the tissue was dissected from the cusp (Fig. 5.1a), and thickness measurements were made using a non-contact laser displacement sensor (Keyence IL-030, Itaska, IL) at three different locations of each cusp specimen to determine the average tissue thickness. Then, the tissue specimens were mounted to a commercial biaxial testing system (BioTester, CellScale, Canada, 1.5 N load cells) via BioRake tines, resulting in an effective testing region of 6.5×6.5 mm (Fig. 5.1b). During mounting, the tissue's circumferential (C) and radial (R) directions were aligned with the X- and Y-directions of the biaxial testing system. Glass beads (with a diameter of 300-$500\,\mu$m) were placed on the center region of each specimen to serve as fiducial markers for quantifying the in-plane strains using a non-contact image-based technique as discussed in Section 2.4.

In this study, we employed the displacement-controlled protocols developed in our lab that are designated for the BioTester system to investigate the mechanical anisotropy and nonlinear mechanical responses of soft collagenous tissues.

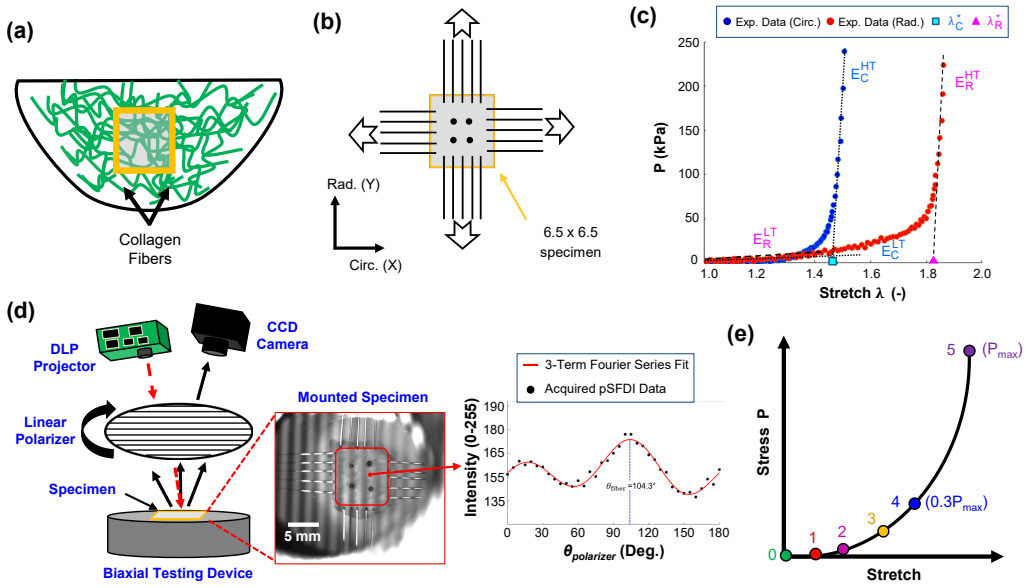

FIGURE 5.1 (a) A square specimen extracted from the center portion of each AV/PV cusp and (b) mounted to a commercial BioTester system. (c) Representative biaxial mechanical testing data, illustrating how the derived mechanics-derived parameters were determined. (d) Schematic of the combined pSFDI-biaxial instrument for quantification of tissue's collagen fiber architecture and resultant θ_{fiber} extraction at (e) the six loading points along the stress-stretch curve.

5.2.3 Biaxial Mechanical Characterizations

In brief, the specimen was submerged in a 37 °C PBS bath during the testing. A preconditioning protocol, consisting of six loading/unloading cycles at a target first Piola-Kirchhoff peak stress $P_{\max}$ of 240 kPa, was first applied to restore the tissue to its *in vivo* functional configuration [13, 61]. After preconditioning, displacement-controlled mechanical testing was conducted, which consists of varying biaxial stress ratios (P_{CC}:P_{RR}=1:1, 1:0.75, 1:0.5, 1:0.25, 0.75:1, 0.5:1, and 0.25:1), for capturing a broad range of physiologically relevant *in vivo* deformations. Each protocol was repeated for three loading/unloading cycles, and force readings from the load cells and CCD camera images were recorded at 15 Hz throughout the test. The data from the final

loading cycle were then used in tissue strain and stress calculations. Note that each specimen was submerged in a 32 °C PBS bath during the entire duration of mechanical testing as well as the subsequent pSFDI imaging. A temperature slightly lower than the body temperature (37 °C) was used to mitigate fogging on the polarizer lens during pSFDI microstructural quantification.

5.2.4 Tissue Stress and Strain Calculations

Digital image correlation (DIC) techniques have been used in previous studies to quantify the in-plane stress and strain for atrioventricular heart valve leaflets [10]. Boundary conditions and different specimen attachment methods have shown to vary the mechanical observations within the same tissue, therefore four fiducial markers (glass beads) were placed in the central region (3×3 mm) of each mounted SHV cusp (Fig. 5.1b). Images were captured throughout mechanical testing by a high-resolution CCD camera at 15 Hz intervals, and the time-dependent positions of the four fiducial markers were analyzed using a built-in DIC technique in the LabJoy software of the BioTester system:

$$\mathbf{x}_I(t) = \mathbf{X}_I + \mathbf{d}_I(t), \quad I = 1 \sim 4, \tag{5.1}$$

where $\mathbf{X}_I$ and $\mathbf{x}_I(t)$ are the marker positions at the undeformed configuration Ω_0 and the deformed (loaded) configuration Ω_t, respectively, and $\mathbf{d}_I(t) = [u_I(t), v_I(t)]^T$ is the displacement vector of marker I, and $u_I(t)$ and $v_I(t)$ are the X- and Y-marker displacements.

The in-plane strains of the tissue were computed using a four-node bi-linear finite element based on the time-varying displacements of the four fiducial markers, during which the deformation gradient $\mathbf{F}$ was determined in an in-house MATLAB program (R2020a, The MathWorks, Natick, MA) based on previously developed strain-calculation techniques [10]:

$$\mathbf{F} = \mathbf{F}(\mathbf{X}, t) = \frac{\partial \mathbf{x}}{\partial \mathbf{X}} = \mathbf{I} + \begin{bmatrix} \sum_{I=1}^{4} B_{X,I} u_I(t) & \sum_{I=1}^{4} B_{Y,I} u_I(t) \\ \sum_{I=1}^{4} B_{X,I} v_I(t) & \sum_{I=1}^{4} B_{Y,I} v_I(t) \end{bmatrix}, \tag{5.2}$$

where $B_{X,I}$ and $B_{Y,I}$ are the shape function derivatives associated for fiducial marker I with respect to the X- and Y-coordinates, respectively, and $\mathbf{I}$ is the 2nd-order identity

tensor. Then, the right Cauchy-Green deformation $\mathbf{C}$ and the Green-Lagrange strain $\mathbf{E}$ can be determined:

$$\mathbf{C} = \mathbf{F}^T\mathbf{F} \text{ and } \mathbf{E} = \frac{1}{2}(\mathbf{C} - \mathbf{I}). \tag{5.3}$$

Note that we utilized a tine-based approach in our biaxial mechanical testing, and, thus, the shear stress was negligible in the tested specimens with proper orientation of each cusp and the inherent rigidity of the BioRake tines [50]. Next, the principal values of $\mathbf{C}$ were used to determine the circumferential stretch λ_{C} and radial stretch λ_{R}. Afterwards, the anisotropy index was computed: $\mathrm{AI} = \lambda_{\mathrm{C}}/\lambda_{\mathrm{R}}$. Finally, the first Piola-Kirchhoff (1^{st} PK) stress $\mathbf{P}$ was calculated from the targeted forces F_C and F_R, the effective edge length of the specimen L, and the average tissue thickness t:

$$\mathbf{P} = \mathrm{diag}[P_{\mathrm{CC}}, P_{\mathrm{RR}}] = \frac{1}{tL}\begin{bmatrix} F_C & 0 \\ 0 & F_R \end{bmatrix}. \tag{5.4}$$

In addition, for the equibiaxial and all other non-equibiaxial biaxial stress protocols two regimes of the stress-stretch curve were identified: (i) the low-stress pre-transitional regime, and (ii) the high-stress post-transitional regime. The low-stress modulus E^{LT}, high-stress modulus E^{HT}, and index of extensibility λ^* of each specimen were then determined for both tissue directions (Fig. 5.1c). Briefly, utilizing an in-house MATLAB program, the stress-strain data points within each region were fitted via least-squares regression, where the slope of the fitted line yields the modulus within each regime, whereas λ^* is the X-intercept of the fitted line (Fig. 5.1c).

5.2.5 pSFDI-Based Quantification of Collagen Fiber Architecture

Following our previously developed procedure for characterizing the collagen fiber microstructure of other heart valve structure and intracranial human aneurysms [98, 103–105], the pSFDI system was integrated with the biaxial mechanical tester (Fig. 5.1d) to evaluate the *load-dependent* collagen fiber architecture (CFA) of the tested specimen, i.e., the fiber orientation angle θ_{fiber} and the degree of optical alignment (DOA). In brief, each specimen was imaged via a 5-megapixel CCD camera (Basler, Germany) for capturing the back-scattered intensity response through a rotating linear polarizer (Thorlabs, Inc., Newton, NJ). The incidental light with spatial frequency patterns were

produced from an LED projector (Texas Instruments, Dallas, TX), with a wavelength of 490 nm equivalent to a cyan light.

The pSFDI imaging technique relies on the birefringent optical response of collagen fibers, where the intensity of the back scattered light is dependent on the polarization and propagation of the incident light from the DLP projector [91, 92]. The back-scattered intensity response of the tissue's collagen microstructure was captured at 37 distinct polarization states (i.e, $0°$ to $180°$ at a $5°$ increment), and the same procedure was repeated for the three linear phase shifts ($0°$, $120°$, $240°$) associated with the projected spatial frequency pattern. Each image from the 37 polarization states was then imported into a custom MATLAB pipeline, where the grey-scale intensity is quantified within each pixel (Fig. 5.1d).

Each cusp was first evaluated using the pSFDI system at the deformation related to peak loading for all the biaxial tension protocols (see Section 2.3). In addition, six loading points of the stretch-stress curve from the last loading cycle of the equibiaxial tension protocol (P_{CC}:P_{RR}=1:1) were included in the collagen fiber architectural analysis (Fig. 5.1e):

(i) Loading Point 0: Tissue mounting configuration, Ω_0 (i.e., zero force and zero deformation)

(ii) Loading Points 1-3: Three evenly spaced intermediate points between Loading Points 0 and 4.

(iii) Loading Point 4: 30% of the peak stress (P_{max})

(iv) Loading Point 5: Peak stress (P_{max})

The six loading points in Fig. 5.1e were determined through an intersection method, allowing θ_{fiber} and DOA to be captured at equally distributed stress intervals prior to the transition point (i.e., Loading Point 4).

5.2.6 Statistical Analysis

Statistical analysis was performed in the R programming language (R Core Team, Toulouse, France) to determine the significance in the variations in both the measured physical quantities (e.g., tissue thickness, preconditioning extensibility), and the derived

parameters (E^{LT}, E^{HT}, λ^{*}, and the AI). The collagen fiber orientation θ_{fiber} and DOA at the mounting configuration were also compared across cusps from the same valve to assess differences in their intrinsic properties. To mitigate the influence of outliers on the determined significance of our data, a non-parametric Kruskal-Wallis test was used to compare the three cusps from the same valve to establish the presence of inter-valve variations. If significant variation were found between any two leaflet groups, a post-hoc Dunn's multiple comparison test was performed to identify which groups were statistically significant. Comparisons that yield a p-value < 0.05 were deemed significant, inferring differences in the intrinsic microstructure or the anisotropic tissue response between any two cusps. Collagen fiber architectural results (i.e., θ_{fiber} and DOA) from the pSFDI experiment are reported as median$\pm 0.5\times$IQR (interquartile range), whereas other physical and derived parameters from the biaxial testing are described as the mean$\pm$SEM (standard error of the mean).

5.3 Results

5.3.1 Biaxial Mechanical Testing Results - Equibiaxial Tension Protocol

A typical J-shaped, anisotropic stress-stretch response was observed in both the tissue's circumferential and radial directions for the cusps of both semilunar valves (Fig. 5.2a,b). Under low stresses, the specimens exhibited a nearly-linear and more compliant response, whereas the AV and PV cusps reached a transition point at $0.3P_{\mathrm{max}}$ where increased stress yielded a stiffer mechanical response. For the AV cusps, the AV-NCC was the most compliant in the circumferential direction ($\lambda_{\mathrm{C}} = 1.43 \pm 0.04$), followed by the AV-RCC and AV-LCC with stretches of $\lambda_{\mathrm{C}} = 1.31 \pm 0.05$ and $\lambda_{\mathrm{C}} = 1.25 \pm 0.03$, respectively, and there were significant differences between the peak circumferential stretch for the AV-LCC when compared to the AV-NCC (p=0.025) (Fig. 5.2a). In contrast, the AV-NCC was the least-compliant in the radial direction ($\lambda_{\mathrm{R}} = 1.63 \pm 0.03$), whereas the AV-LCC exhibits the greatest radial stretch ($\lambda_{\mathrm{R}} = 1.71 \pm 0.05$) among all the three AV cusps (Fig. 5.2a). The PV cusps followed a similar direction-dependent stress-stretch responses, with minimal extensibility in the circumferential direction and large tissue radial stretches for all the three cusps (Fig. 5.2b). There were small variations in the circumferential tissue-stretch among all specimens, although the PV-LC

($\lambda_C = 1.29 \pm 0.04$) and PV-AC ($\lambda_C = 1.30 \pm 0.05$) were slightly more compliant than the PV-RC ($\lambda_C = 1.23 \pm 0.02$). Further, the PV-AC was considerably more responsive in the radial direction ($\lambda_R = 2.01 \pm 0.04$) compared to the other two PV cusps.

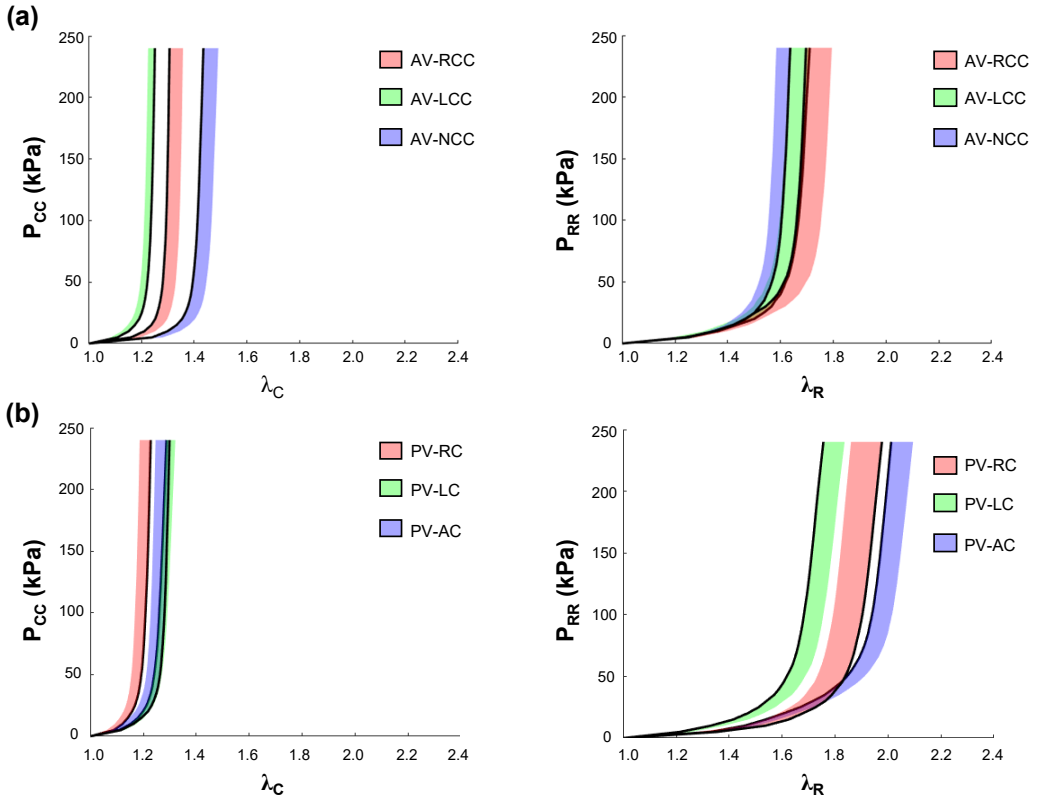

FIGURE 5.2 1st PK stress vs. stretch responses of (a) the aortic valve (AV) cusps, and (b) the pulmonary valve (PV) cusps under equibiaxial tensions. Results are reported as mean (solid lines) ±SEM (one-sided shared areas).

5.3.2 Biaxial Mechanical Testing Results - Non-Equibiaxial Protocols

Under non-equibiaxial loading, the AV and PV cusps exhibited a similar J-shaped mechanical response for both tissue directions, with an initial near-linear response that transitions into a non-linear region (Fig. 5.3). When subjected to circumferentially dominant loading (P_{CC}:P_{RR}=1:0.25, 1:0.5, 1:0.75), the AV cusps generally yielded larger tissue stretches in the radial direction compared to the circumferential direction (see the left column of Fig. 5.3). The largest circumferential deformation occurred in all specimens under the minimum radial stress (P_{CC}:P_{RR}=1:0.25), where the AV-NCC was the

most extensible (λ_C=1.41 ± 0.02) compared to the AV-RCC (λ_C=1.34 ± 0.02) and AV-LCC (λ_C=1.28 ± 0.02). Interestingly, the AV-LCC and AV-RCC specimens still had a greater radial deformation under the same load (AV-LCC: λ_R=1.54 ± 0.02; AV-RCC: λ_R=1.51 ± 0.02), but the AV-NCC was more isotropic (λ_R=1.52 ± 0.02) in comparison. Under radially dominant loading (P_{CC}:P_{RR}=0.25:1, 0.5:1, 0.75:1) the cusps became more stiff in the circumferential direction with a decrease in circumferential stress, allowing the tissue deformation to the governed by the radial stress component (Fig. 5.3). With the greatest reduction in circumferential stress (P_{CC}:P_{RR}=0.25:1), the AV-LCC and AV-RCC had similar radial deformations of λ_R=1.78 ± 0.05 and λ_R=1.79 ± 0.05, respectively, When comparing the peak stretches in the circumferential directions, significant differences were seen between the AV-LCC and AV-NCC specimens for circumferential and radially dominant loading.

More specifically, all biaxial protocols with preferential circumferential stress had significantly different circumferential stretches ($p = 0.024$ for P_{CC}:P_{RR}=1:0.75, $p = 0.042$ for P_{CC}:P_{RR}=1:0.50, and $p = 0.024$ for P_{CC}:P_{RR}=1:0.25, with similar significance found in the radially dominant protocols ($p = 0.029$ for P_{CC}:P_{RR}=0.75:1, and $p = 0.032$ for P_{CC}:P_{RR}=0.5:1). In addition, the AV-NCC had the smallest radial stretch ($\lambda_R = 1.67 \pm 0.02$) under the same loading protocol (P_{CC}:P_{RR}=0.25:1), but interestingly, the AV-NCC specimens were also the least extensible in the radial direction regardless of the stress state. This *non-monotonic* directional coupling between the two tissue directions can be seen for the other AV cusps (e.g., the AV-LCC), where a minimal circumferential deformation for all loading protocols resulted largest radial tissue stretches.

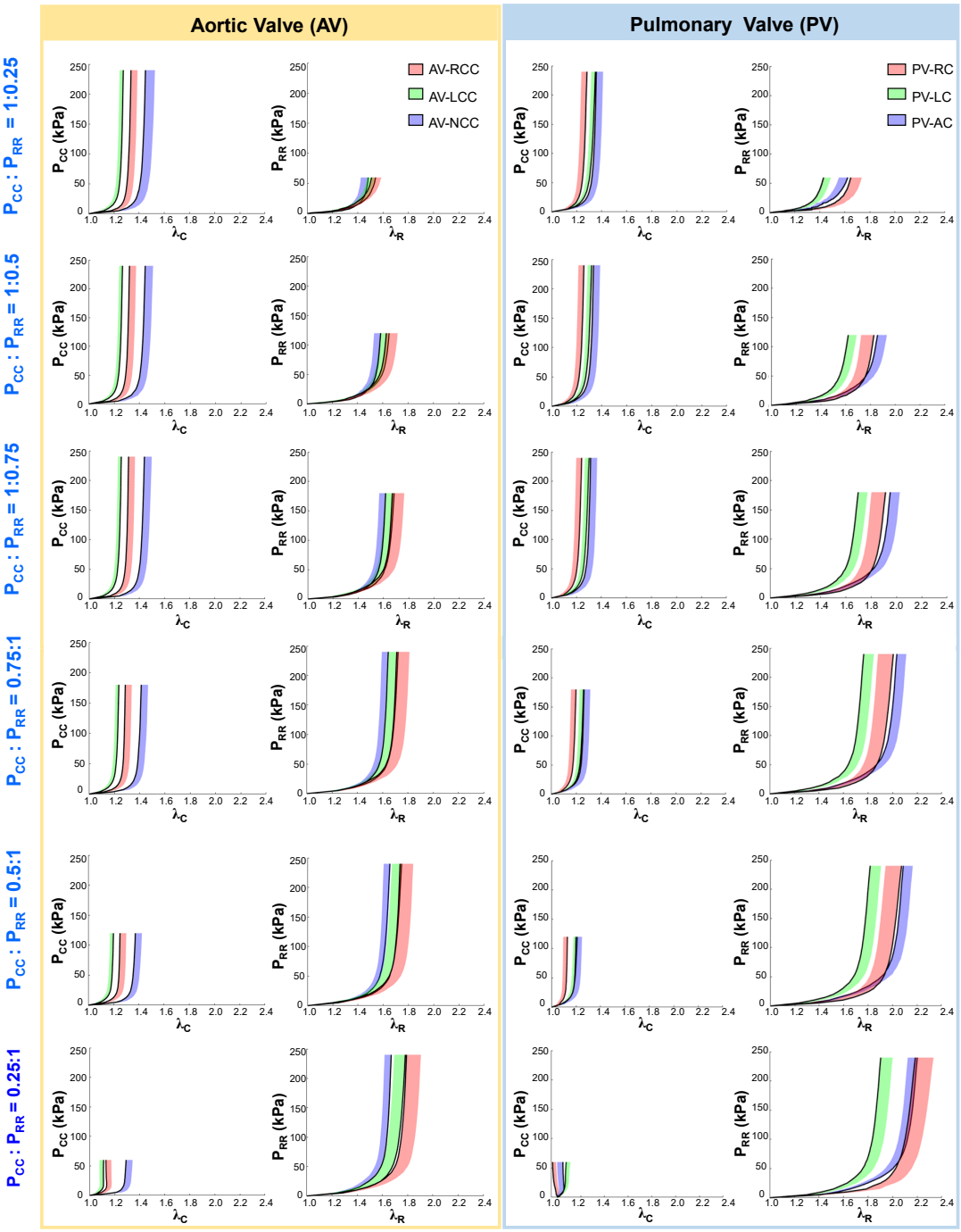

FIGURE 5.3 1st PK stress vs. stretch responses of the aortic valve (AV) cusps (left column), and the pulmonary valve (PV) cusps (right column) under various non-equibiaxial tensions. Results are reported as mean (solid lines) ±SEM (one-sided shared areas).

On the other hand, all the three PV cusps displayed greater similarities in circumferential stretch under circumferential loading (see the right column of Fig. 5.3). However, the PV-AC was more extensible for all the circumferential biaxial protocols, especially at the greatest reduction in the radial stress (P_{CC}:P_{RR}=1:0.25), where the largest circumferential deformations were observe in the PV-AC (λ_C=1.36 ± 0.03) and the PV-LC (λ_C=1.35 ± 0.03) in comparison to the PV-RC (λ_C=1.26 ± 0.03). Despite this large reduction in the radial stress, the PV-AC (λ_R=1.62 ± 0.03) and the PV-RC (λ_R=1.65 ± 0.03) had greater extensibility in the radial direction, while the PV-LC was only slightly more compliant (λ_R=1.43 ± 0.03). For the remaining circumferentially dominant loading protocols, the PV-AC had the largest deformations in both the circumferential and radial directions, whereas radially dominant loading yielded comparable trends in the mechanical responses of the AV specimens. Interestingly, the largest magnitude of tissue stretches was found under P_{CC}:P_{RR}=0.25:1 protocol, during which the PV-AC reached a peak λ_R of 2.20 ± 0.03, followed by the PV-RC (λ_R=2.19 ± 0.03) and the PV-LC (λ_R=1.90 ± 0.03). Theses larger tissue deformation in the radial direction resulted in minimal changes in the circumferential stretches for the PV-AC (λ_R=1.08 ± 0.03) and PV-LC (λ_R=1.09 ± 0.03) and a compression in the PV-RC (λ_R=0.98 ± 0.03) due to the higher radial stretches among all the PV cusps.

5.3.3 Tissue Thickness, Post-Preconditioning Deformation, and Material Anisotropy

Tissue thicknesses, measured prior to biaxial mechanical testing, were found to be 0.33 ± 0.03, 0.34 ± 0.02, and 0.35 ± 0.03 mm for the AV-LCC, AC-RCC, and AV-NCC, respectively (Fig. 5.4a). For the PV cusps (Fig. 5.5a), the thicknesses were found for the PV-LC (0.27 ± 0.02 mm), PV-AC (0.28 ± 0.02 mm), and PV-RC (0.26 ± 0.03 mm). When comparing between the two semilunar valves, the three AV cusps had larger numerical values of tissue thickness than the three PV cusps. Regarding preconditioning, the AV-LCC experienced the smallest post-preconditioning (PPC) deformation in the circumferential direction ($\lambda_C = 1.08 \pm 0.02$), with significant differences found between the AV-NCC and the AV-RCC ($\lambda_C = 1.16 \pm 0.02$ vs. 1.09 ± 0.03, $p = 0.022$, Fig. 5.4b). Similarly, the circumferential PPC deformations were found to be significantly different between the PV-RC and the PV-AC ($\lambda_C = 1.12 \pm 0.02$ vs. 1.03 ± 0.01, $p = 0.048$, Fig. 5.5b). All

the specimens exhibited a greater compliance in the tissue's radial direction than the circumferential direction (Fig. 5.4b & Fig. 5.5b).

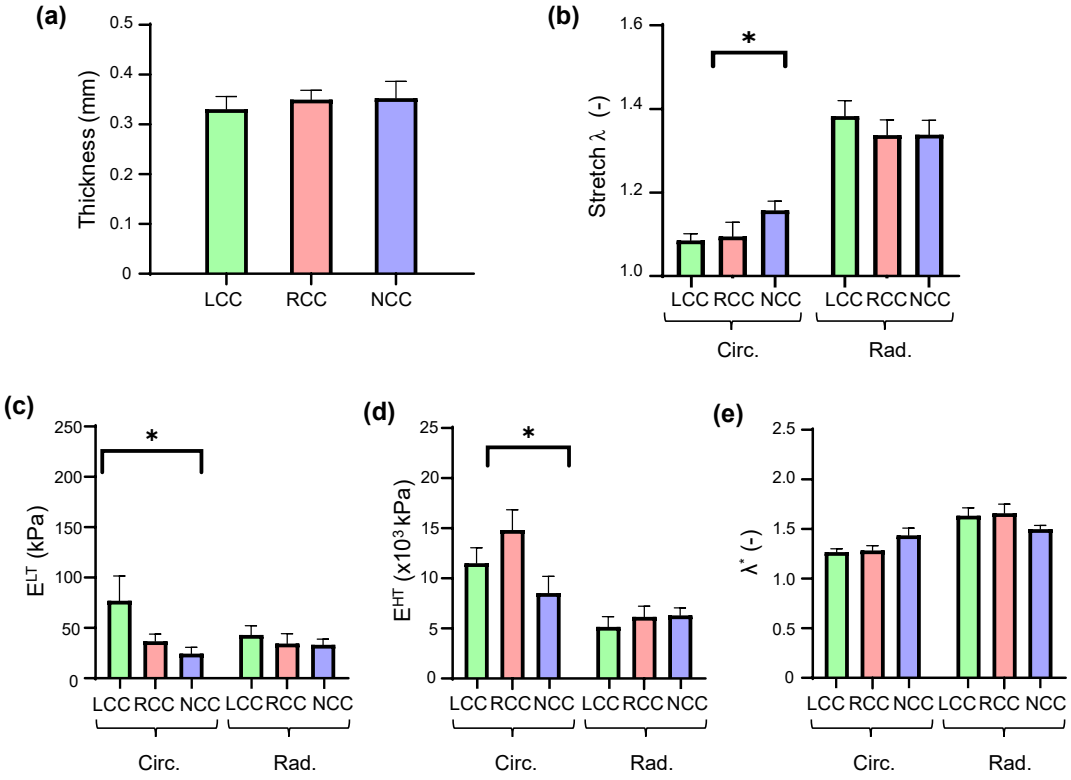

FIGURE 5.4 (a) Tissue thickness, and (b) post-preconditioning deformations for each cusp of the aortic valve (AV). The derived mechanics parameters under equibiaxial loading: (c) low-tension moduli, (d) high-tension elastic moduli, and (e) the index of extensibility . Values are reported as mean±SEM (* denotes $p < 0.05$).

The AI was used to assess the mechanical behavior of the specimens at any given stress state, where values greater than or smaller than 1.0 indicate material anisotropy in the tissue (i.e., $\mathrm{AI} = 1.0$ indicates perfectly isotropic). Under equibiaxial loading, the AV-LCC was the most anisotropic specimen (0.74 ± 0.03), followed by the AV-RCC (0.79 ± 0.04) and the AV-NCC (0.88 ± 0.02). There were significant differences ($p = 0.033$) in the AI between the AV-LCC and the AV-NCC groups, indicating disparities in their material properties. Greater anisotropic tissue behavior was also observed in the PV-RC (0.64 ± 0.04) and PV-AC (0.66 ± 0.03), but the PV-LC (0.76 ± 0.04) presented similar values to the AV cusps.

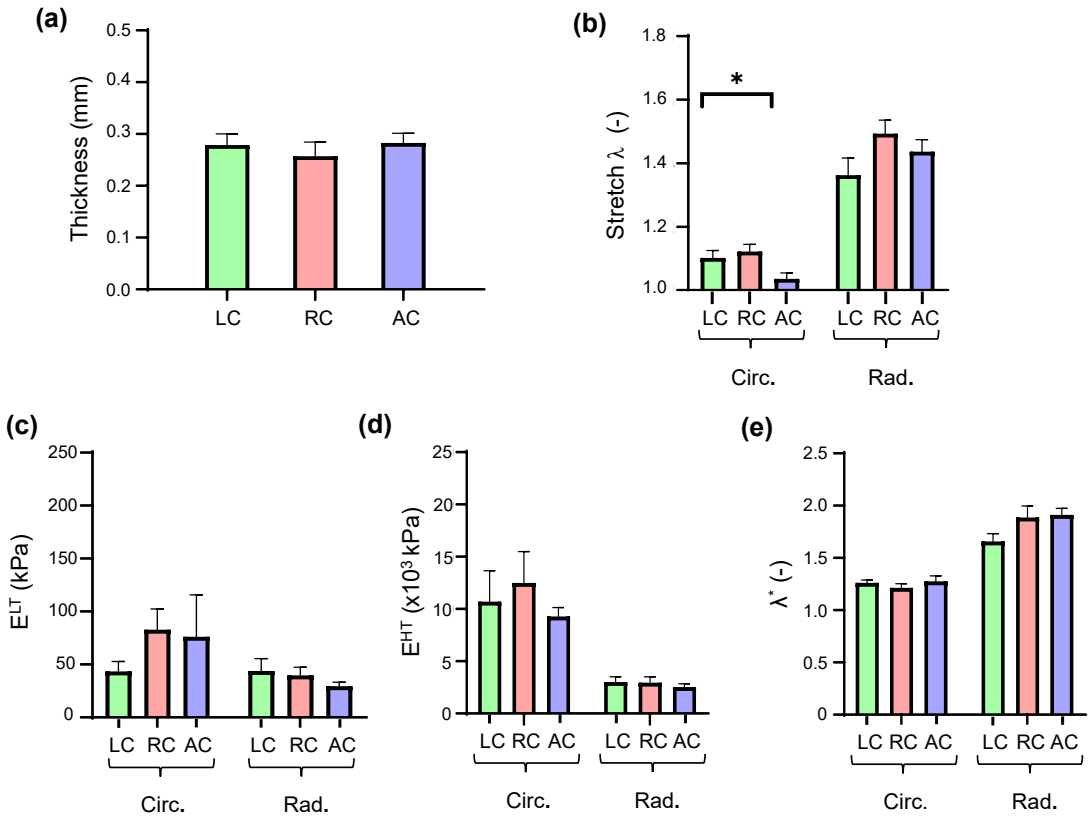

FIGURE 5.5 (a) Tissue thickness, and (b) post-preconditioning deformations for each cusp of the pulmonary valve (PV). The derived mechanics parameters under equibiaxial loading: (c) low-tension moduli, (d) high-tension elastic moduli, and (e) the index of extensibility . Values are reported as mean±SEM (* denotes $p < 0.05$)

When the AI was measured for all the non-equibiaxial loading protocols, there were two distinct trends: (i) as radial stress decreases (P_{CC}:P_{RR}=1:0.75, 1:0.5, 1:0.25), each AV and PV cusp became more isotropic; and (ii) as circumferential stress decreases (P_{CC}:P_{RR}=0.75:1, 0.5:1, 0.25:1), the specimens became more anisotropic with the greatest amount of anisotropy occurring under the peak radially dominant loading (i.e., P_{CC}:P_{RR}=0.25:1). Significant differences were found in the AI between the AV-LCC and AV-NCC for both circumferentially dominant loading (P_{CC}:P_{RR}=1:0.75, $p = 0.033$; P_{CC}:P_{RR}=1:0.25, $p = 0.01$) and radially dominant loading (P_{CC}:P_{RR}=0.75:1, $p = 0.032$; P_{CC}:P_{RR}=0.5:1, $p = 0.046$) protocols; however, no significant differences were found for the PV cusps.

5.3.4 Other Derived Mechanics Parameters

At low equibiaxial stresses, the AV-LCC was the most stiff with the highest circumferential low-stress modulus (62.3 ± 16.4 kPa), followed by the AV-RCC ($E_{\mathrm{C}}^{\mathrm{LT}}$=$36.8 \pm 7.14$ kPa) and AV-NCC ($E_{\mathrm{C}}^{\mathrm{LT}}$=$24.5 \pm 6.2$ kPa) (Fig. 5.4c). Significant differences ($p = 0.033$) were found in the circumferential low-stress modulus between the AV-LCC and the AV-NCC tissues (Fig. 5.4c). For the PV specimens (Fig. 5.5c), the PV-RC displayed greater material stiffness ($E_{\mathrm{C}}^{\mathrm{LT}}$=$82.7 \pm 19.7$ kPa) compared to the PVAC ($E_{\mathrm{C}}^{\mathrm{LT}}$=$76.2 \pm 39.4$ kPa) and the PV-LC ($E_{\mathrm{C}}^{\mathrm{LT}}$=$43.5 \pm 9.3$ kPa). At the higher-stress regime, the elastic moduli of the AV cusps increased, where the AV-RCC specimens became the most stiff ($E_{\mathrm{C}}^{\mathrm{HT}}$=$14.8 \pm 2.0$ MPa) and the AV-NCC and AV-LCC specimens were within a similar range (Fig. 5.4d). Significant differences ($p = 0.035$) were found in the circumferential high-stress modulus between the AV-RCC and the AV-NCC (Fig. 5.4d). The most substantial tissue stiffening was observed in the PV-RC specimens ($E_{\mathrm{C}}^{\mathrm{HT}}$=$12.5 \pm 3.0$ MPa) for the PV cusps, along with comparable increases in the PV-LC and the PV-AC counterparts (Fig. 5.5d).

On the other hand, the radial low-stress modulus of the AV-LCC specimens ($E_{\mathrm{R}}^{\mathrm{LT}}$=$43.0 \pm 9.2$ kPa) had the largest value compared to the AV-NCC ($E_{\mathrm{R}}^{\mathrm{LT}}$=$33.3 \pm 5.5$ kPa) and AV-RCC ($E_{\mathrm{R}}^{\mathrm{LT}}$=$34.5 \pm 9.7$ kPa) specimens under low stresses, although there were no significant differences found among the three cusps (Fig. 5.4c). Smaller radial low-stress moduli were observed for the PV-LC ($E_{\mathrm{R}}^{\mathrm{LT}}$=$43.9 \pm 11.6$ kPa), PV-AC ($E_{\mathrm{R}}^{\mathrm{LT}}$=$29.6 \pm 3.7$ kPa), and PV-RC ($\mathrm{E}_{\mathrm{R}}^{\mathrm{LT}}$=$39.75 \pm 7.8$ kPa) in comparison to the circumferential direction (Fig. 5.5c). In the high-stress regime, the elastic modulus in the radial direction for the AV-NCC ($E_{\mathrm{R}}^{\mathrm{HT}}$=$6.3 \pm 6.2$ MPa) had smaller variations with respect to the circumferential direction, whereas the AV-LCC ($E_{\mathrm{R}}^{\mathrm{HT}}$=$5.2 \pm 1.0$ MPa) and AV-RCC ($E_{\mathrm{R}}^{\mathrm{HT}}$=$6.2 \pm 1.1$ MPa) showed larger decreases in the tissue stiffness (Fig. 5.4d). The difference in the elastic modulus was greater between the circumferential and the radial directions for the PV cusps (PV-LC: $E_{\mathrm{R}}^{\mathrm{HT}}$=$3.0 \pm 0.5$ kPa, PV-RC: $E_{\mathrm{R}}^{\mathrm{HT}}$=$2.9 \pm 0.6$ MPa; PV-AC: $E_{\mathrm{R}}^{\mathrm{HT}}$=$2.5 \pm 0.3$ MPa), with no statistically significant variations between the cusps (Fig. 5.5d).

TABLE 5.1 Derived mechanics parameters for the AV cusps under non-equibiaxial loading protocols. Values are reported as mean±SEM.

AV-LCC							
Loading Ratio	AI	E_C^{LT} (kPa)	E_R^{LT} (kPa)	E_C^{HT} (MPa)	E_R^{HT} (MPa)	$\lambda^*(-)_C$	$\lambda^*(-)_R$
$T_C:T_R$=1:0.25	0.84±0.03	68.9±30.0	66.8±20.3	9.8±0.8	0.7±0.4	1.31±0.03	1.45±0.07
$T_C:T_R$=1:0.5	0.78±0.03	65.9±24.6	45.6±9.6	10.1±1.1	3.1±0.7	1.29±0.03	1.57±0.08
$T_C:T_R$=1:0.75	0.76±0.03	75.9±31.2	51.0±12.4	10.8±1.5	4.2±0.8	1.28±0.03	1.61±0.08
$T_C:T_R$=0.25:1	0.65±0.04	43.4±9.1	38.8±7.2	-1.7±3.2	4.4±0.6	1.11±0.03	1.71±0.09
$T_C:T_R$=0.5:1	0.70±0.03	80.4±26.1	63.7±19.9	9.8±1.9	5.1±0.9	1.21±0.03	1.67±0.08
$T_C:T_R$=0.75:1	0.73±0.03	96.9±39.9	67.6±22.8	9.7±1.4	5.7±1.1	1.25±0.03	1.65±0.08
AV-RCC							
Loading Ratio	AI	E_C^{LT} (kPa)	E_R^{LT} (kPa)	E_C^{HT} (MPa)	E_R^{HT} (MPa)	$\lambda^*(-)_C$	$\lambda^*(-)_R$
$T_C:T_R$=1:0.25	0.90±0.05	48.4±13.4	61.5±25.6	14.1±2.7	0.7±0.6	1.31±0.05	1.46±0.07
$T_C:T_R$=1:0.5	0.83±0.05	53.2±17.1	45.7±13.3	12.8±1.7	4.2±1.2	1.30±0.05	1.59±0.08
$T_C:T_R$=1:0.75	0.81±0.04	39.3±10.4	35.9±8.6	14.9±2.0	5.4±1.0	1.29±0.05	1.64±0.09
$T_C:T_R$=0.25:1	0.68±0.05	82.6±28.6	34.8±9.6	-0.8±1.8	5.7±0.8	1.15±0.05	1.74±0.11
$T_C:T_R$=0.5:1	0.75±0.05	60.4±19.8	39.7±10.5	6.4±2.3	5.9±0.8	1.30±0.05	1.70±0.10
$T_C:T_R$=0.75:1	0.78±0.05	59.5±18.4	46.1±14.0	16.2±3.2	6.6±0.9	1.27±0.05	1.68±0.09
AV-NCC							
Loading Ratio	AI	E_C^{LT} (kPa)	E_R^{LT} (kPa)	E_C^{HT} (MPa)	E_R^{HT} (MPa)	$\lambda^*(-)_C$	$\lambda^*(-)_R$
$T_C:T_R$=1:0.25	1.10±0.08	18.3±2.9	37.9±7.1	7.7±1.2	1.2±0.7	1.52±0.08	1.38±0.02
$T_C:T_R$=1:0.5	0.92±0.04	29.8±14.0	34.3±4.5	8.9±1.5	4.3±0.8	1.50±0.07	1.47±0.03
$T_C:T_R$=1:0.75	0.89±0.03	21.5±4.9	28.9±3.1	8.0±1.3	5.8±0.8	1.47±0.07	1.52±0.04
$T_C:T_R$=0.25:1	0.77±0.03	51.6±23.2	27.9±4.8	-0.1±2.8	8.1±2.2	1.29±0.06	1.58±0.06
$T_C:T_R$=0.5:1	0.83±0.02	40.9±17.4	42.6±13.2	6.5±1.5	8.1±1.9	1.39±0.06	1.55±0.06
$T_C:T_R$=0.75:1	0.86±0.02	35.5±15.8	31.7±5.3	8.6±1.8	7.9±1.6	1.45±0.07	1.53±0.06

Moreover, the transition in the biaxial mechanical curves was captured by the index of extensibility λ^*. All of the AV and PV cusps were found to have a greater λ^* in the radial direction, signifying a longer ”toe” region of the stress-stretch tissue response. The extensibility of the AV-RCC (λ_C^*:λ_R^*=1.28:1.66) and AV-LCC (λ_C^*:λ_R^*=1.27:1.63) groups varied greatly from their circumferential counterparts, whereas the AV-NCC shared a similar values between the two direction (λ_C^*:λ_R^*=1.45:1.49) (Fig. 5.4e). Greater variations between the two directions were observed for the PV specimens, owing to their large radial deformations. The PV-AC had the largest index of extensibility in both tissue directions (λ_C^*:λ_R^*=1.28:1.91), compared to the PV-RC (λ_C^*:λ_R^*=1.21:1.89) and the PV-LC (λ_C^*:λ_R^*=1.26:1.67) (Fig. 5.5e). The values of the derived quantities for all the non-

equibiaxial loading protocols can be found in Table 5.1 & Table 5.2 for the AV and the PV, respectively.

TABLE 5.2 Derived mechanics parameters for the AV cusps under non-equibiaxial loading protocols. Values are reported as mean±SEM.

PV-LC							
Loading Ratio	AI	E_C^{LT} (kPa)	E_R^{LT} (kPa)	E_C^{HT} (MPa)	E_R^{HT} (MPa)	$\lambda^*(-)_C$	$\lambda^*(-)_R$
$T_C:T_R$=1:0.25	0.97±0.06	45.0±9.8	48.8±6.7	7.6±1.1	1.4±0.4	1.33±0.03	1.37±0.06
$T_C:T_R$=1:0.5	0.84±0.05	52.9±15.3	45.0±7.6	8.1±1.3	2.0±0.4	1.30±0.03	1.54±0.07
$T_C:T_R$=1:0.75	0.79±0.05	55.9±19.9	37.3±4.9	8.7±1.6	2.7±0.5	1.28±0.03	1.62±0.07
$T_C:T_R$=0.25:1	0.60±0.05	42.3±10.2	33.9±6.4	-1.7±1.0	3.0±0.4	1.07±0.03	1.81±0.09
$T_C:T_R$=0.5:1	0.70±0.05	70.0±18.7	42.4±6.4	3.5±2.1	3.2±0.5	1.20±0.03	1.74±0.08
$T_C:T_R$=0.75:1	0.74±0.05	72.9±20.3	51.9±11.5	7.5±1.5	3.3±0.5	1.25±0.03	1.70±0.08
PV-RC							
Loading Ratio	AI	E_C^{LT} (kPa)	E_R^{LT} (kPa)	E_C^{HT} (MPa)	E_R^{HT} (MPa)	$\lambda^*(-)_C$	$\lambda^*(-)_R$
$T_C:T_R$=1:0.25	0.78±0.04	101.3±32.8	38.9±7.3	8.5±1.3	1.0±0.2	1.27±0.04	1.59±0.08
$T_C:T_R$=1:0.5	0.71±0.04	110.8±31.4	49.2±9.1	9.36±1.9	2.1±0.7	1.25±0.04	1.76±0.09
$T_C:T_R$=1:0.75	0.67±0.04	117.9±38.9	38.2±7.4	10.9±12.4	2.6±0.7	1.25±0.04	1.82±0.10
$T_C:T_R$=0.25:1	0.48±0.04	80.7±20.3	31.3±3.6	-0.1±1.3	3.3±1.0	0.99±0.03	2.06±0.13
$T_C:T_R$=0.5:1	0.57±0.04	79.1±14.7	33.9±6.8	5.2±4.1	2.9±0.7	1.12±0.03	1.98±0.12
$T_C:T_R$=0.75:1	0.62±0.04	124.8±45.4	31.8±5.7	7.3±4.0	3.1±0.7	1.19±0.04	1.93±0.12
PV-AC							
Loading Ratio	AI	E_C^{LT} (kPa)	E_R^{LT} (kPa)	E_C^{HT} (MPa)	E_R^{HT} (MPa)	$\lambda^*(-)_C$	$\lambda^*(-)_R$
$T_C:T_R$=1:0.25	0.85±0.05	84.5±31.1	77.7±38.6	9.2±1.0	0.9±0.2	1.34±0.05	1.54±0.06
$T_C:T_R$=1:0.5	0.73±0.04	85.4±43.4	38.5±5.6	12.1±2.0	1.5±0.2	1.32±0.05	1.78±0.07
$T_C:T_R$=1:0.75	0.68±0.03	95.3±46.6	54.3±23.4	12.1±1.9	2.5±0.3	1.30±0.05	1.88±0.07
$T_C:T_R$=0.25:1	0.50±0.03	106.6±59.9	23.5±2.6	-6.9±13.4	2.5±0.3	1.06±0.05	2.10±0.07
$T_C:T_R$=0.5:1	0.58±0.03	110.8±45.3	31.6±4.6	7.5±2.2	2.8±0.3	1.19±0.05	2.02±0.07
$T_C:T_R$=0.75:1	0.63±0.03	110.9±54.8	43.4±8.8	9.5±1.8	3.0±0.3	1.25±0.05	1.97±0.07

5.4 Collagen Fiber Architecture Results

Representative pSFDI-quantified CFA results from individual AV and PV cusps specimens are shown in Fig. 5.6 & Fig. 5.8, respectively. For the AV cusps, the collagen fibers were oriented in the circumferential direction after mounting to the biaxial tester, and maintained a circumferential orientation after a pre-conditioning protocol was employed (Fig. 5.6). Interestingly, the collagen fiber architecture became slightly more

aligned with increasing DOA between the mounting and PPC configurations. Under equibiaxial loading (P_{CC}:P_{RR}=1:1) each specimen aligned with the circumferential axis, with the largest change in collagen fiber orientation presented by the AV-LCC specimen ($9.6 \pm 19.0\%$). Under the same loading protocol, the collagen fibers became more aligned with increasing DOA (i.e., up to 40.8% between the PPC configuration and peak equibiaxial loading).

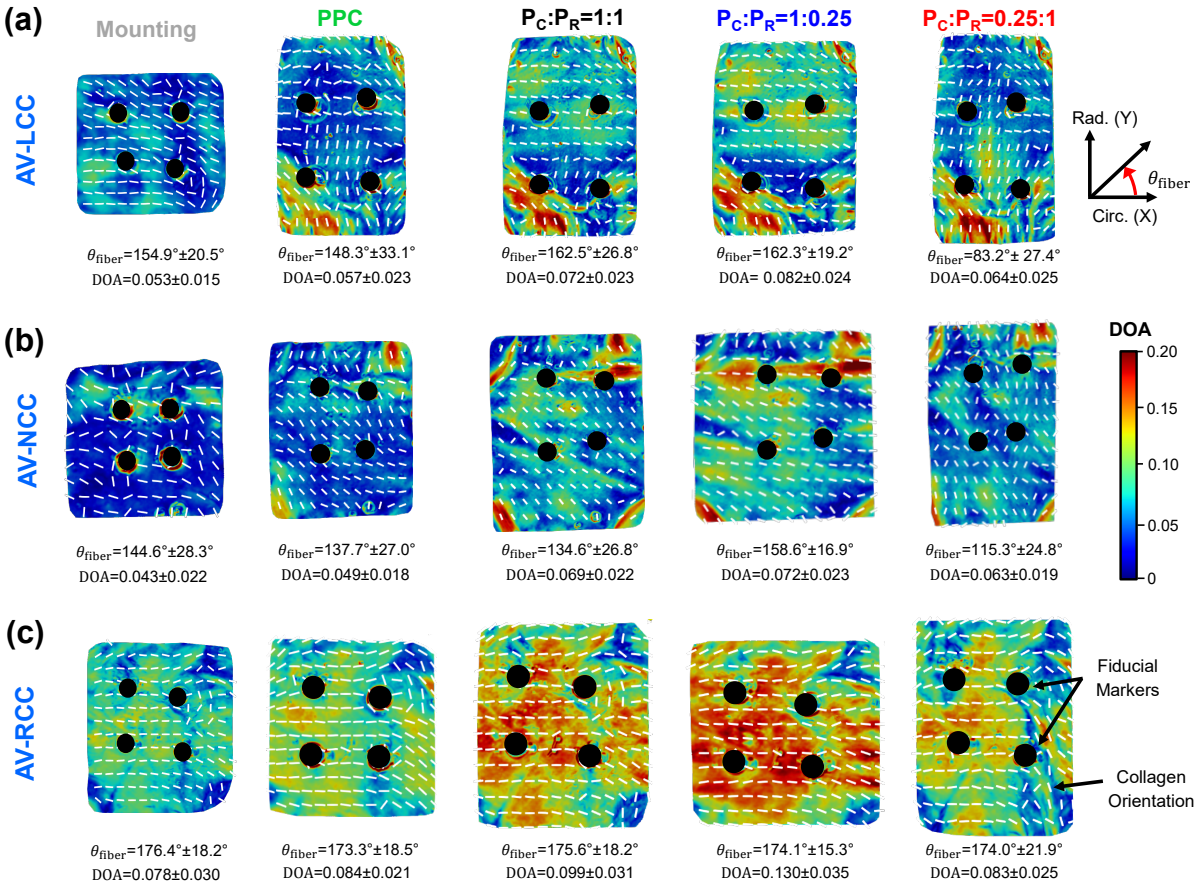

FIGURE 5.6 Collagen fiber architecture quantifications for represenative (i) AV-LCC (*top row*), (ii) AV-NCC (*middle row)*, and (iii) AV-RCC (*bottom row*) specimens. Collagen fiber orientation and DOA are reported as median$\pm 0.5^{*}$IQR.

Furthermore, under circumferentially dominant loading (P_C:P_R=1:0.25), the collagen fibers became even more aligned with the circumferential axis, whereas the largest increase in the quantified DOA was found $43.9 \pm 4.3\%$ (AV-LCC), $46.9 \pm 27.8\%$ (AV-NCC) and $54.8 \pm 66.7\%$ (AV-RCC) compared to the PPC configuration. Radially dominant load-

ing ($P_C : P_R$=0.25:1) resulted in fiber reorientation towards the radial direction for the AV-LCC (θ_{fiber}=83.24° ±27.4°) and AV-NCC (θ_{fiber}=115.5°±24.8°) representative specimens, while the AV-RCC remained circumferentially oriented (θ_{fiber}=174.0°±21.9°) with the greatest fiber alignment (DOA=0.083±0.25) than the other AV cusps.

In addition, an anisotropic stress-stretch response for the representative AV specimens was shown in Fig. 5.7. The greatest tissue extensibility was seen under radially dominant loading for the AV-LCC and AV-NCC specimens, which also led to the greatest fiber reorientation. In contrast, the AV-RCC specimen had the greatest tissue extensibility under equibiaxial loading where the greatest change in fiber reorientation was observed for this specimen Fig. 5.6c. Overall, the collagen fiber architecture was shown to reorient towards the direction of the greatest applied loading for all the AV specimens.

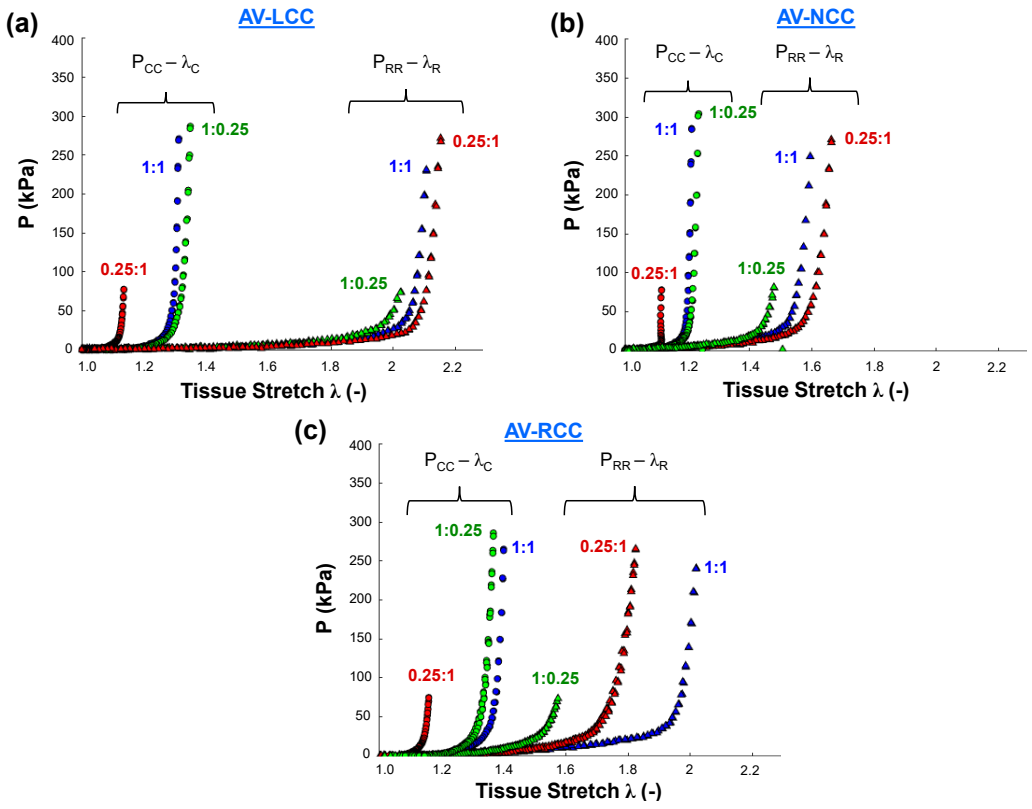

FIGURE 5.7 Equibiaxial and non-equibiaxial mechanical testing results for the (a) AV-LCC, (b) AV-NCC, and (c) AV-RCC representative specimens found in Figure 5.5

For the representative PV cusps, pSFDI results showed greater random collagen fiber orientation after mounting was, with predominantly radially-oriented fibers for the PV-LC (θ_{fiber}=91.81° ± 11.5°) and PV-AC (θ_{fiber}=113.5° ± 24.5°) and circumferentially oriented fibers for the PV-RC (θ_{fiber}=23.0° ± 73.1°) shown in Fig. 5.8. After preconditioning, there were slight changes in the collagen fiber orientation for each cusp, although each tissue remained aligned with their original orientation axis. Equibiaxial loading led to reorientation towards the circumferential direction for the PV-LC (θ_{fiber}=147.4° ± 29.1°) and PV-RC (θ_{fiber}=23.6° ± 14.2°) tissues, while the PV-AC remained virtually unchanged (θ_{fiber} =113.8° ± 9.4°).

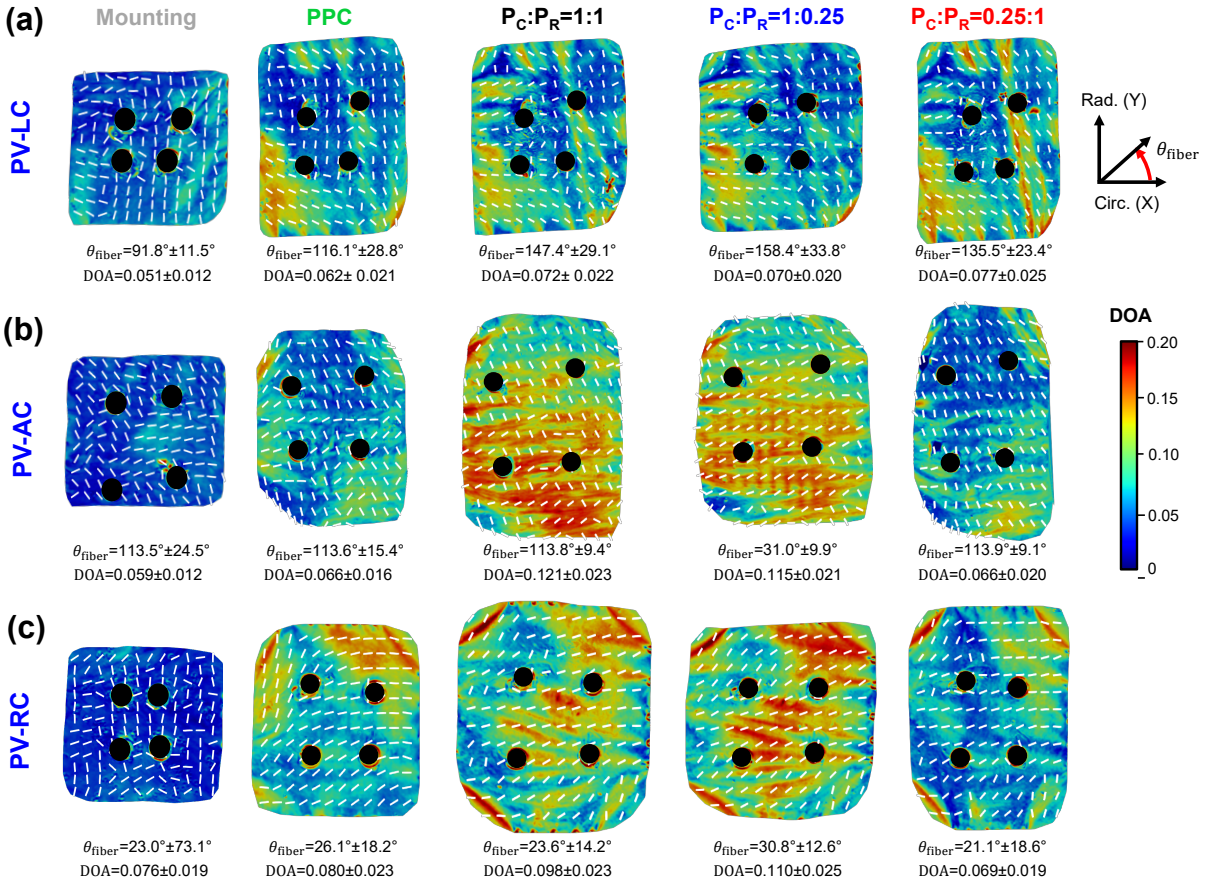

FIGURE 5.8 Collagen fiber architecture quantifications for represenative (i) PV-LC (*top row*), (ii) PV-AC (*middle row)*, and (iii) PV-RC (*bottom row*) specimens. Collagen fiber orientation and DOA are reported as median±0.5*IQR.

Each PV cusp experienced different fiber recruitment and degree of alignment under biaxial testing protocols, with no distinct trend observed. More specifically, the PV-LC had the greatest collagen fiber alignment under radially dominant loading (DOA=0.077 ± 0.025), whereas the PV-AC was most aligned under equibiaxial loading (DOA=0.121 ± 0.023). The PV-RC specimen yielded the largest DOA values when compared to the PV-LC and PV-AC under circumferentially dominant loading (DOA=0.110 ± 0.025). Similar trends in direction-dependent collagen fiber reorientation were seen for the PV cusps, where the PV-LC and PV-AC revealed collagen fiber shifts towards the direction of greatest applied loading, while the PV-RC remained unchanged (Fig. 5.8).

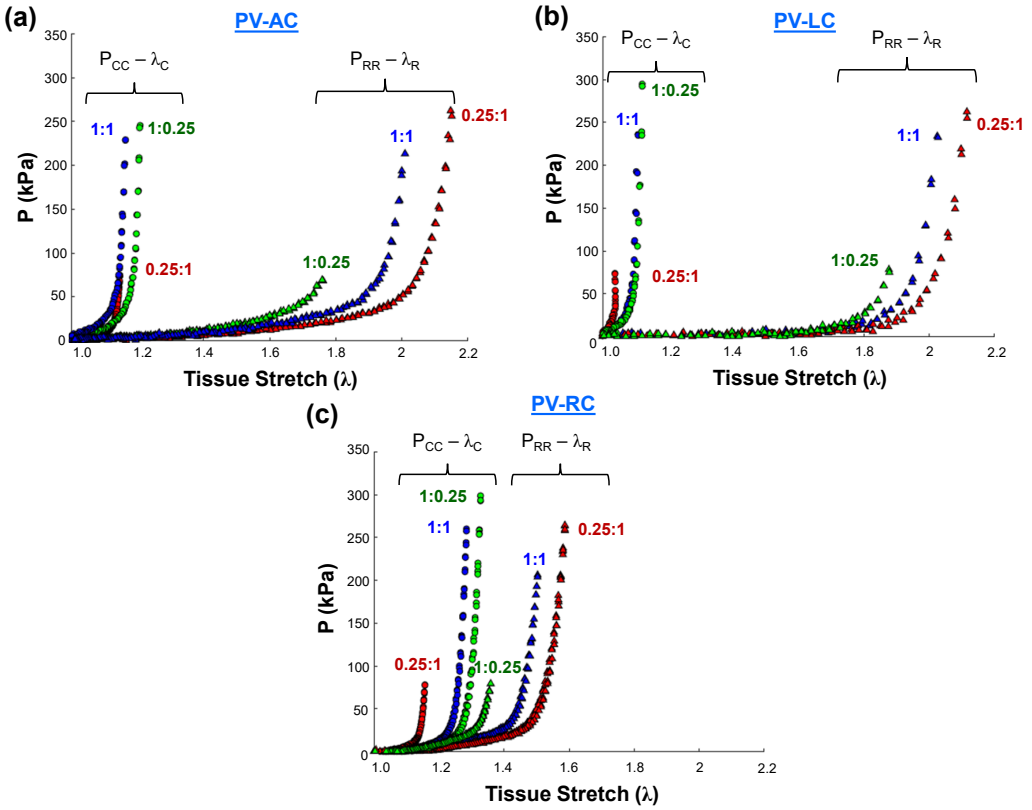

FIGURE 5.9 Equibiaxial and non-equibiaxial mechanical testing results for the (a) PV-AC, (b) PV-LC, and (c) PV-RC representative specimens found in Fig. 5.8

Larger tissue stretches were seen within the PV cusps under the three represented biaxial testing protocols, and distinct directional coupling was observed for both the circumferential and radial direction (Fig. 5.9). The overall extensibility of the PV-AC and

PV-LC exceeded that of the PV-RC, with a much greater tissue stiffness, and smaller collagen fiber reorientation (Fig. 5.9).

5.4.1 Load-Dependent Changes in the Collagen Fiber Architecture

The AV cusps exhibited a predominant circumferential orientation prior to biaxial testing, whereas the PV specimens collagen fiber architecture was aligned with the tissue radial axis (Table 5.3). The median DOA was also observed for each set of cusps, with less alignment for all the AV cusps than their PV counterparts, with the exception of the AV-RCC specimens that had the greatest alignment among all the investigated semilunar valve cusp specimens. For the representative AV-NCC specimen, a circumferentially dominant collagen fiber orientation was observed at the mounting configuration (Fig. 5.10a). As incremental loading was applied, a more defined bimodal collagen fiber distribution were observed with two distinct histogram peaks (Fig. 5.10f). In comparison, a low-level alignment was observed at the mounting configuration, prior to the steady increases at each incremental loading point Fig. 5.10a-e). The largest change in the collagen fiber alignment was seen between Loading Point 1 and Loading Point 2 in the belly portion of the tissue, as evidenced by the DOA color map (Fig. 5.10b,c).

TABLE 5.3 Baseline values for the collagen fiber orientation (θ_{fiber}) and DOA prior to preconditioning and biaxial testing. Values are reported as median$\pm$0.5*IQR.

Specimen	θ_{fiber}	*p*-value	DOA	*p*-value
AV-LCC	157.1°$\pm$10.8°	LCC vs. RCC [0.969]	0.054$\pm$0.005	LCC vs. RCC [0.104]
AV-RCC	157.6°$\pm$36.7°	RCC vs. NCC [0.507]	0.065$\pm$0.008	RCC vs. NCC [0.095]
AV-NCC	125.5°$\pm$26.2°	NCC vs. LCC [0.472]	0.053$\pm$0.004	NCC vs. LCC [0.601]
PV-LC	79.4°$\pm$31.6°	LC vs. RC [0.656]	0.064$\pm$0.012	LC vs. RC [0.548]
PV-RC	71.1°$\pm$33.5°	RC vs. AC [0.405]	0.061$\pm$0.013	RC vs. AC [0.786]
PV-AC	88.1°$\pm$36.7°	AC vs. LC [0.698]	0.064$\pm$0.019	AC vs. LC [0.742]

Similar quantification was made for a representative PV-LC as shown in Fig. 5.11. While under zero equibiaxial load, the PV-LC specimen maintained a predominantly radial collagen fiber orientation with relatively smaller alignment throughout the tissue (Fig. 5.11a). Under initial loading (Loading Point 1), the bi-modal distribution of the collagen fiber response became more prominent, with little change in the alignment of the fibers (Fig. 5.11b). With increased loading, the median collagen fiber orientation shifts towards the circumferential direction while the DOA showed slight increases throughout the tissue (Fig. 5.11d). This trend can be seen throughout the remaining incremental loading points up to peak equibiaxial loading, pointing towards collagen fiber reorientation and realignment with increased load for the PV-LC specimen (Fig. 5.11f).

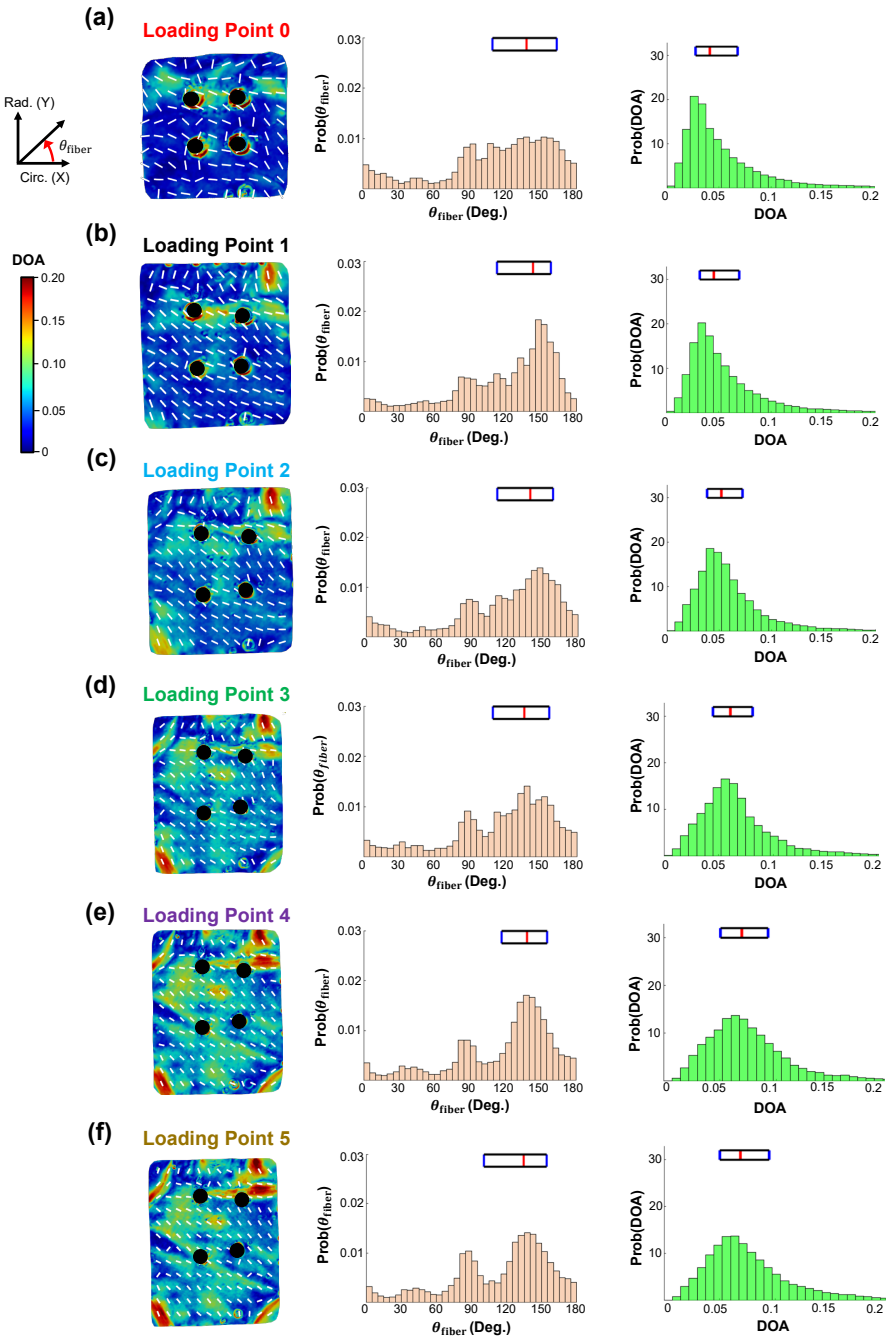

FIGURE 5.10 Incremental changes in the collagen fiber orientation and DOA were examined for an AV-NCC specimen between the (a) unloaded state (loading Point 0) and subsequent loading states as follows: (b) Loading Point 1, (c) Loading Point 2, (d) Loading Point 3, (e) Loading Point 4, and (f) Loading Point 5. The white lines represent the predicted collagen fiber orientations, and the colormap intensities denote the degree of optical anisotropy (DOA).

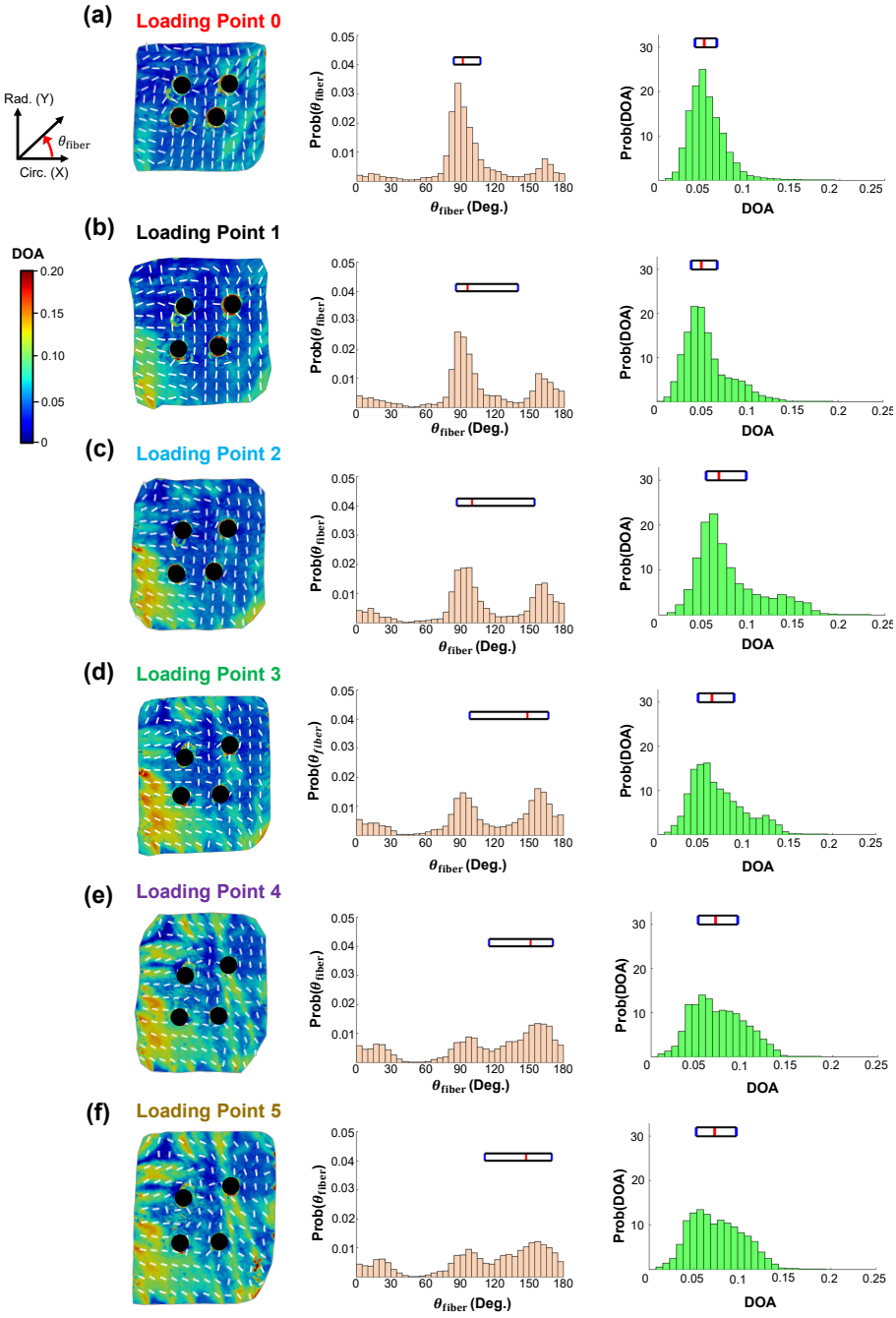

FIGURE 5.11 Incremental changes in the collagen fiber orientation and DOA were examined for an PV-LC specimen between the (a) unloaded state (loading Point 0) and subsequent loading states as follows: (b) Loading Point 1, (c) Loading Point 2, (d) Loading Point 3, (e) Loading Point 4, and (f) Loading Point 5. The white lines represent the predicted collagen fiber orientations, and the colormap intensities denote the degree of optical anisotropy (DOA).

5.4.2 Load-Dependent Changes in Collagen Fiber Architecture - All AV/PV Specimens

For the AV-LCC and AV-RCC specimens, the collagen fiber architecture showed slight reorientation towards the circumferential direction between Loading Points 0 and 1 (Table 5.4). The AV-NCC collagen fiber orientation showed small changes between these two loading points, maintaining a predominantly radial orientation. Between each sequential loading point, the AV-LCC reoriented towards the radial direction between Loading Points 1 and 2, and maintained this fiber orientation before reorienting towards the circumferential direction at Loading Points 4 and 5. The AV-RCC exhibited the largest change in the sequential loading points between Loading Points 0 and 1, followed by the minimal changes in the collagen fiber orientation up to Loading Point 5. Interestingly, the AV-NCC specimens exhibited a radially oriented collagen fiber architecture at Loading Point 0 (θ_{fiber}=$125.5^{\circ}\pm26.2^{\circ}$), and displayed large reorientation between the sequential loading points up to Loading Point 5. When considering non-sequential loading points, the AV-LCC and AV-NCC had the greatest changes in the collagen fiber reorientation from Loading Points 3 to 5 ($-9.0^{\circ}\pm9.7^{\circ}$) and from Loading Points 3 to 4 ($+24.3^{\circ}\pm14.8^{\circ}$), respectively. After initial applied stress, the AV-RCC had a less tendency to reorientation, exhibiting the largest collagen fiber reorientation between Loading Points 0 and 2 ($-10.3^{\circ}\pm14.4^{\circ}$). More consistent load-dependent changes in the quantified DOA was observed with several key findings summarized as follows. First, when comparing the sequential loading points, the largest change in DOA was observed between Loading Points 1 and 2, before steadily decreasing in percent change as loading increases (Table 5.5). Second, the greatest change in the quantified DOA occurred between Loading Points 0 and 5 for the AV-NCC ($43.4\%\pm6.3\%$) and AV-RCC ($23.7\%\pm4.7\%$), and between Loading Points 0 and 4 for the AV-LCC ($35.0\%\pm3.4\%$) when comparing the non-sequential loading points. Finally, the AV-RCC specimens seemed to be less sensitive to collagen fiber realignment, yielding the smallest changes in the quantified DOA under sequential loading compared to the other two AV cusps.

TABLE 5.4 Difference in the quantified collagen fiber orientation (θ_{fiber}) between two biaxial tension states of the 5 loading points for the AV cusps. Changes in θ_{fiber} are reported as mean±SEM.

Loading Point	Loading Point as the reference (baseline)				
	0	1	2	3	4
AV-LCC					
1	-5.1°±5.2°	-	-	-	-
2	2.0°±1.2°	7.1°±5.1°	-	-	-
3	3.6°±1.5°	8.7°±5.2°	1.6°±0.9°	-	-
4	3.5°±2.4°	8.6°±5.2°	1.6°±2.1°	-0.1°±1.4°	-
5	-5.4°±8.9°	-0.3°±5.2°	-7.4°±9.2°	-9.0°±9.7°	-8.9°±10.1°
AV-RCC					
1	-8.7°±13.3°	-	-	-	-
2	-10.3°±14.4°	-1.6°±2.6°	-	-	-
3	-9.2°±14.6°	-0.5°±1.8°	1.1°±2.4°	-	-
4	-9.0°±14.4°	-0.3°±2.2°	1.3°±1.9°	0.2°±2.0°	-
5	-8.8°±15.0°	-0.1°±2.7°	1.5°±2.1°	-0.4°±2.0°	0.2°±0.7°
AV-NCC					
1	0.1°±6.6°	-	-	-	-
2	3.2°±10.3°	11.8°±10.9°	-	-	-
3	-10.2°±8.7°	-1.6°±4.4°	-13.5°±14.5°	-	-
4	14.0°±8.7°	22.6°±12.0°	10.8°±6.8°	24.3°±14.8°	-
5	12.6°±8.6°	21.2°±11.8°	9.4°±6.5°	22.9°±14.6°	-1.4°±0.5°

†The positive changes in the fiber orientation (θ_{fiber}) denote the counterclockwise reorientation,whereas the negative changes represent the clockwise reorientation.

TABLE 5.5 Percent change in the quantified degree of optical anisotropy (DOA) between two biaxial tension states of the 5 loading points for the AV cusps. Values are reported as mean±SEM.

Loading Point	Loading Point as the reference (baseline)				
	0	1	2	3	4
AV-LCC					
1	7.0±1.6%	-	-	-	-
2	16.0±2.2%	8.4±1.1%	-	-	-
3	25.2±2.8%	17.0±1.9%	7.9±1.1%	-	-
4	35.0±3.4%	26.3±3.2%	16.4±2.3%	7.9±1.6%	-
5	34.3±3.5%	25.7±3.3%	15.8±2.4%	7.3±1.6%	-0.5±0.6%
AV-RCC					
1	0.6±3.2%	-	-	-	-
2	7.8±3.9%	7.4±1.9%	-	-	-
3	15.7±4.3%	15.1±2.4%	7.2±1.3%	-	-
4	22.9±5.0%	22.5±4.0%	14.2±2.4%	6.2±1.5%	
5	23.7±4.7%	23.3±3.7%	15.0±2.3%	7.0±1.7%	0.7±0.9%
AV-NCC					
1	6.8±2.2%	-	-	-	-
2	19.9±4.7%	11.8±2.3%	-	-	-
3	30.7±5.3%	22.0±3.2%	9.0±1.6%	-	-
4	42.4±6.4%	33.0±4.4%	18.8±2.9%	8.9±1.6%	-
5	43.4±6.3%	33.9±4.4%	19.6±2.7%	9.7±1.3%	0.8±0.8%

Changes in the collagen fiber orientation and DOA were also quantified for the three PV specimen (see Table 5.6 & Table 5.7). Small-value changes in the fiber orientation were observed between Loading Points 0 and 1 for the PV-LC ($-0.8^{\circ} \pm 1.7^{\circ}$), whereas the collagen fiber architecture for the PV-RC ($+18.1^{\circ} \pm 21.7^{\circ}$) and the PV-AC ($+14.2^{\circ} \pm 8.2^{\circ}$) exhibited large reorientation towards the radial direction under the initial applied load (Table 5.6). When comparing the sequential loading points, the collagen fiber architecture of the PV-LC reoriented towards the circumferential direction between Loading Points 1 and 2 ($-9.2^{\circ} \pm 11.3^{\circ}$), before realigning with the radial axis until Loading Point 4. Both the PV-RC and the PV-AC demonstrated the largest changes between Loading Points 0 and 1, with smaller changes between the remaining sequential loading points.

Prior to the peak loading, however, the PV-AC specimens became abruptly aligned with the circumferential axis between Loading Points 4 and 5 ($-13.2^{\circ} \pm 11.9^{\circ}$). The greatest collagen fiber reorientation was observed in the toe region of the stress-stretch curve (i.e., Loading Points 0, 1, and 2) for the PV-LC and the PV-RC, whereas the PV-AC showed the greatest difference in fiber orientation between Loading Points 3 and 5 (Table 5.6). Similar to the AV cusps, consistent changes in the quantified DOA were found with several key findings summarized as follow. First, when comparing sequential loading points, the PV-LC ($11.7\% \pm 3.3\%$) and the PV-RC ($10.1\% \pm 1.8\%$) exhibited the greatest change in the DOA between Loading Points 1 and 2. The PV-AC, on the other hand, experienced the largest change in the fiber alignment ($18.3\% \pm 6.8\%$) between Loading Points 0 and 1 (Table 5.7). Second, the difference in the fiber alignment increased incrementally between Loading Point 0 and other non-sequential loading points for all the PV specimens. Finally, the PV-LC and the PV-RC specimens were the most similar in collagen fiber realignment throughout the equibiaxial loading, while the PV-AC displayed much larger increases between Loading Point 0 and other loading points (Table 5.7).

TABLE 5.6 Difference in the quantified collagen fiber orientation (θ_{fiber}) between two biaxial tension states of the 5 loading points for the PV cusps. Changes in θ_{fiber} are reported as mean±SEM.

Loading Point	Loading Point as the reference (baseline)				
	0	1	2	3	4
PV-LC					
1	-0.8°±1.7°	-	-	-	-
2	-10.0°±11.0°	-9.2°±11.3°	-	-	-
3	-4.1°±11.1°	-3.3°±11.1°	5.9°±4.1°	-	-
4	-2.2°±11.6°	-1.4°±11.6°	7.8°±4.6°	1.9°±1.8°	-
5	-2.5°±11.5°	-1.7°±11.5°	7.5°±4.6°	1.6°±2.4°	-0.3°±1.11°
PV-RC					
1	18.1°±21.7°	-	-	-	-
2	18.0°±20.3°	-0.1°±20.7°	-	-	-
3	16.0°±20.2°	-2.2°±20.9°	-2.0°±1.1°	-	-
4	14.9°±21.5°	-3.2°±21.1°	-3.1°±2.3°	-1.1°±1.9°	-
5	16.2°±21.2°	-1.9°±20.2°	-1.8°±2.0°	0.3°±1.8°	1.4°±1.0°
PV-AC					
1	14.2°±8.2°	-	-	-	-
2	14.7°±9.0°	0.4°±9.4°	-	-	-
3	18.7°±9.7°	4.5°±7.0°	4.0°±5.6°	-	-
4	11.9°±8.4°	-2.4°±9.6°	-2.8°±8.5°	-6.8°±5.7°	-
5	-1.3°±15.9°	-15.6°±17.0°	-16.0°±14.5°	-20.0°±13.3°	-13.2°±11.9°

†The positive changes in the fiber orientation (θ_{fiber}) denote the counterclockwise reorientation,whereas the negative changes represent the clockwise reorientation.

TABLE 5.7 Percent change in the quantified degree of optical anisotropy (DOA) between two bi-axial tension states of the 5 loading points for the PV cusps. Values are reported as mean±SEM.

Loading Point	Loading Point as the reference (baseline)				
	0	1	2	3	4
PV-LC					
1	2.7±3.1%	-	-	-	-
2	14.8±5.1%	11.7±3.3%	-	-	-
3	18.5±6.7%	15.2±4.8%	2.9±2.4%	-	-
4	21.0±7.4%	17.6±5.8%	5.0±3.7%	1.8±1.7%	-
5	22.1±7.3%	18.7±5.7%	6.1±3.6%	2.9±1.4%	1.1±0.9%
PV-RC					
1	8.2±2.5%	-	-	-	-
2	19.0±2.6%	10.1±1.8%	-	-	-
3	21.3±3.0%	12.2±2.2%	2.0±1.2%	-	-
4	20.4±4.2%	11.2±3.0%	1.0±2.0%	-1.0±1.2%	
5	22.7±4.5%	13.4±3.3%	3.0±2.3%	0.9±1.8%	2.0±1.3%
PV-AC					
1	18.3±6.8%	-	-	-	-
2	31.1±8.4%	11.6±5.3%	-	-	-
3	39.8±9.2%	18.6±5.5%	6.5±1.9%	-	-
4	37.6±8.4%	17.7±6.5%	5.6±3.7%	-1.0±2.2%	-
5	43.5±11.8%	21.3±7.4%	11.0±7.9%	3.3±5.6%	4.3±5.2%

5.5 Discussion

5.5.1 Tissue-Level Mechanical Properties

Combined mechanical and microstructural characterizations of the SHV cusps allowed for the comparisons of the tissue-level mechanical properties between two similar anatomical structures, located at different positions within the heart. Overall, we found that the AV and the PV cusps displayed an anisotropic, stress-strain response with greater extensibility in the tissue radial direction versus the circumferential direction under all the loading protocols. Mechanical directional coupling was also observed

among all the non-equibiaxial loading protocols, where the magnitude of the tissue stretch in the radial direction increased with the decreasing circumferential stress, highlighting the unique mechanical anisotropy and directional coupling of the SHV cusps (Fig. 5.3). This material anisotropy, although present within both semilunar valves, was the most profound in the PV for both the low stress and the high stress regimes of the stress-stretch curve. Under the low-stress regime, the PV yielded a slightly stiffer circumferential response to the mechanical loading, although the $E_{\mathrm{R}}^{\mathrm{LT}}$ was relatively similar for both valves. During the high-stress regime, however, the circumferential direction was roughly four times stiffer than the radial direction for the PV. This observation is complemented by the derived index of extensibility λ^* with similar values observed in the circumferential direction between both SHVs, whereas the PV had a much larger index of extensibility in the radial direction. The lower value of λ^* in the radial direction for the AV cusps is directly correlated to a faster recruitment of the fibers under mechanical loads, owing to their initial circumferential collagen fiber alignment compared to the PV (Table 5.1). The greater anisotropic response in the PV cusps for both the low- and high-stress regimes suggest a considerable amount of collagen fiber uncrimping and straightening that is required to bring the collagen fiber architecture to its fully aligned state, primarily due to the more randomly distributed fibers within the PV cusp compared to the AV cusps. These microstructural and mechanical observations for the SHV cusps were in agreement with those first reported by Christie *et al.* which utilized suture-based biaxial mechanical testing. Our results agreed more with other recent studies aimed at investigating the mechanical properties of the valve cusps using the biaxial testing methods similar to our experiment [53, 57, 60, 62]. Interestingly, the derived circumferential moduli of the PV cusps in the low-stress regime did not agree with Huang *et al.* and Pham *et al.*, which reported the PV to be more isotropic in the low-stress regime than their left-sided counterparts for both porcine and human hearts, respectively [53, 57]. The discrepancies in the results between the present work and the existing literature could have occurred due to two potential sources: (i) the method used to extract the low- and high-stress moduli of the specimens could be different between studies. For example, our study utilized a set number of points to determine the pre-transitional region in the low-stress regime, whereas Huang *et al.* sectioned the stress-strain curve into three zones ranging from 0% to 35% strains; and (ii) the use of porcine hearts versus aged human hearts (70.1 ± 3.7 years old) warrants variations

in the morphological and mechanical properties [53, 78, 123]. Conclusively, it is likely that these different mechanical analyses and the use of human specimens contributed to the discrepancy in the observed anisotropy of the SHV within the low-stress regime.

5.5.2 Microstructural Findings

From the pSFDI-based collagen fiber quantification, we observed a load-dependent collagen fiber architecture for both the AV and PV cusps. In the mounting configuration, the AV and the PV cusps exhibited distinctly different median collagen fiber orientation and alignment throughout the tissue (Table 5.3). The AV exhibited a predominantly circumferential collagen fiber orientation, compared to the radial orientation and higher fiber alignment in the PV. A larger $0.5\times$IQR range for both the collagen fiber orientation and DOA were found for the PV cusps, pointing towards a more random collagen structure and alignment for these specimens (Table 5.3). The more homogeneously distributed collagen fiber architecture in the AV cusps could be explained by the need to counteract greater transvalvular stresses experienced *in vivo* compared to the PV. Further, the greater thickness of the AV cusps could also be explained by its anatomical position, as it has been previously reported that thicker heart valve leaflets are more effective in reducing the peak stresses experienced *in vivo* compared to a thinner structure [60, 124]. Overall, morphological and microstructural differences were observed between the two valves, which can elucidated by the variations in physiological environment. For both SHV cusps, the collagen fiber architecture was found to reorient towards the direction of the greatest applied stress, which can especially be seen in the mechanical directional coupling between the two tissue directions. For example, under radially dominant loading (P_{CC}:P_{RR}=0.25:1), the collagen fibers straighten under initial applied load before reorienting towards the radial axis, resulting in a much larger tissue stretch in the radial direction. The AV cusps were the most aligned under circumferentially dominant loading (P_{CC}:P_{RR}=1:0.25), primarily due to their initial circumferential alignment at the mounting configuration. In contrast, the greatest alignment in the PV cusps varied among specimens, further highlighting the role of collagen fiber variance in tissue-level mechanical behavior. Similar behaviors can be seen when incremental points along the stress-stretch curve were examined. More specifically, the collagen fiber architecture was randomly aligned at the mounting configuration (Loading Point 0), and a greater

increase in stress resulted in greater fiber realignment within the tissue and a shift in the median collagen fiber orientation. The PV cusps, although showing greater collagen fiber alignment, were much more susceptible to collagen fiber reorientation as greater stress was applied to the tissue. A more homogeneous collagen fiber architecture for the AV specimens and a greater fiber alignment in the PV specimens were also observed in the previous studies by Billiar & Sacks and Joyce & Sacks [61, 85, 87]. Interestingly, these studies reported negligible collagen fiber reorientation under pressure loading after fixation, which could be related to the method used to induce physiological stress on the leaflets. Previous mechanical studies have highlighted that the form of loading (i.e., pressure loading vs. controlled biaxial mechanical loading) can lead to significant differences in the tissue-level mechanical responses [125, 126]. Therefore, the discrepancy in the load-driven collagen microstructural changes can likely be attributed to the distinct differences in applied loading between the these studies. The use of this non-destructive, opto-mechanical approach improves the current understanding of the load-dependent collagen fiber architecture within the SHV cusps, providing the ability to observe microstructural changes within *the same specimen*.

5.5.3 Study Limitations and Future Work

There are several limitations in this study. First, displacement-controlled biaxial testing methods were utilized to emulate the stresses experienced by the leaflet *in vivo*. For pSFDI imaging, displacement-controlled loading was used to achieve the specimen size associated with the peak stress for all protocols, but there was a reduction in the target stress values due to the stress relaxation of the tissues. Second, the BioRake tine-based mounting system may elicit shear within the tissue, which may be present under physiological conditions. To negate these shear-induced effects, the tissue circumferential and radial axis were aligned with the X- and Y-axes of the biaxial testing system. Third, there were small mispredictions in the collagen fiber orientation for some of the AV and PV samples, which could have been caused by surface defects (e.g., bubbles) or tissue folding. In this work, the tissue was carefully mounted to the biaxial testing device and bubbles were removed from the PBS bath to minimize the mispredictions in θ_{fiber} throughout the sample. It is important to note that the collagen fiber orientation and DOA were averaged across every pixel within the region of interest, which would

make those potential, small mispredictions negligible in regards to the bulk-tissue microstructural response. Finally, the DOA metric is connected to the optical anisotropy of the sample, whereas structural-based metrics, such as the normalized orientation index, have been used for previous collagen fiber quantification [49, 86].

The fundamental extension of this study is to utilize the load-dependent collagen fiber quantification to improve fiber-based multi-scale models. Current fiber-based models assume homogeneous CFA distributions or employ information from destructive and small FOV imaging techniques, which provide inconsistency due observations being made across fix samples and the inability to observe both the local and bulk-tissue microstructural properties of collagen fibers [90, 127, 128]. Therein, the ability to non-destructively evaluate the collagen fiber architecture within the same specimen at the micro and macro scale could improve the fidelity of these models. Further investigations would also benefit from employing the SFDI aspects of this system to quantify the collagen fiber orientation at varying tissue depths, as it known that the microstructure in heart valve leaflets vary both spatially and transmurally throughout the tissue [12–16]. The implementation of these variations into computational models could bridge the gap between bulk-tissue and layer specific microstructural contributions under physiological loading. Further, the pSFDI-based quantification system would allow improvements to tissue engineering based scaffolds containing birefringent fibers. Previous investigations have noted that the fiber alignment within these scaffolds are important to the ECM morphology and smooth muscle cell phenotype of tissue engineered structures during development. Unique quantification for other collagenous tissues, such as the coronary arteries, could be made to observe the microstructural-mechanical relationship under physiologically relevant loads. From a clinical standpoint, this approach can improve the development of bio-prosthetic heart valves (BHVs), which have shown to have varying life cycles and can lead to calcification *in vivo* due to collagen cross-linking. Insight to the collagen fiber architecture of these BHVs could also aid in biomaterial selection and tissue engineering methods widely used in industry. Expanding our fundamental understanding of the tissue mechanics-microstructure relationship of the SHVs provides unique insight into computational modeling and BHV design, improving current clinical therapeutics and surgical procedures used to treat valvular disease.

5.5.4 Conclusion

This investigation, which is the *first of its kind*, further elucidates the interconnected relationship between the tissue-level mechanics and the load-dependent collagen fiber architecture of the AV and PV cusps using an integrated pSFDI-biaxial testing system. The AV had a distinct homogeneous collagen fiber orientation with a more isotropic response to stress, whereas the collagen fibers in the PV cusps were more anisotropic, with greater alignment and a randomly distributed collagen fiber network. Evaluating the microstructural-mechanical relationship within the SHV cusps is essential to enhancing the accuracy of current fiber-based multi-scale models. Such enhancements in current modeling frameworks would not only aid in better understanding the individual organ-level function and diseases associated with each valve, but could be used for patient-specific surgical planning and to evaluate available therapeutic options. As part of our future investigations, we plan to employ our pSFDI-based method to evaluate the microstructure in other collagenous soft tissues, and improving the depth-discrimination capabilities of our system.

6 CONCLUSION

6.1 Key Research Findings

The results presented in this thesis further our fundamental understanding of the interrelationship between the collagen fiber architecture (CFA) and the mechanical behavior of heart valve leaflets. A novel pSFDI-based experimental framework was used to quantify the CFA load-dependent changes in TV leaflets, *for the first time*, at improved acquisition speeds, a larger field of view, and without the need for tissue alterations. Then, to bridge existing gaps in connecting the CFA to the mechanical behaviors, a holistic examination of the biomechanical and microstructural properties of the MV and the SHVs was performed. These results showed that all heart valve leaflets/cusps were not well aligned at their intrinsic state and had a preferred circumferential orientation, except for the PV cusps which were more randomly distributed [60].

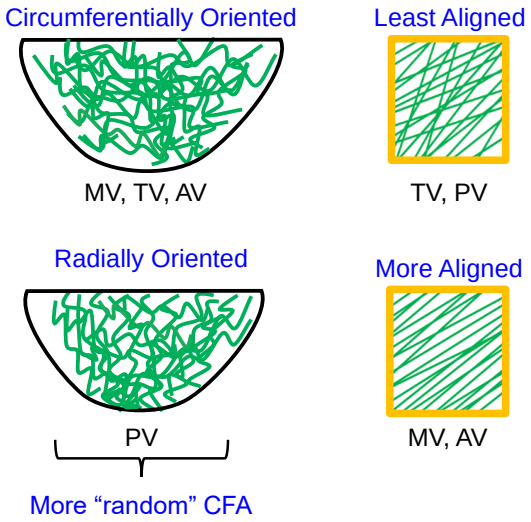

FIGURE 6.1 Schematic detailing the intrinsic properties of the four heart valve leaflets/cusps: (left column) the preferred fiber direction and (right column) the alignment of the collagen fibers at the mounting coniguration.

Under mechanical loading, all four hearts valves demonstrated directionally-dependent properties. Specifically, we saw CFA reorientation towards the preferential loading direc-

tion and greater DOA values during circumferential loading, which was more dominant in the SHVs compared to the AHVs. Biomechanical observations similarly pointed towards a more dynamic CFA in the SHVs, exhibiting greater circumferential stiffness and radial extensibility than the AHVs. In conjunction, anatomical positioning within the heart (i.e., left, right) further impacted the observed CFA alignment and mechanical responses for all four heart valves. The left-sided heart valve structures, the MV leaflets and AV cusps, had greater collagen fiber alignment at the mounting configuration and at all peak loading scenarios, reflective of their functional requirements to counteract greater a pressure gradient (Fig. 6.1). The TV leaflets and PV cusps, although less aligned, had greater tissue deformations in the radial direction and a more stiff circumferential direction, connected to their lower collagen content and smaller average thickness.

These research investigations have provided a microstructural basis for the observed mechanical behavior in all four heart valves, informing multiscale models that mimic healthy tissue behavior. The opto-mechanical approach utilized in these analyses serves as a potential tool to better understand the mechanics-microstructure interactions for other collagenous soft tissues.

6.2 Future Research Directions

6.2.1 SFDI Investigations of the Layered HV Microstructure

While we have provided detailed information on the CFA alignment and orientation in heart valve leaflets, we utilized the aggregate DC signal that summarizes the transmural microstructural information. The mechanical properties and collagen content have been shown to vary throughout each layer in AV and TV leaflets, and, therefore, future investigations into the layer-specific CFA changes via the AC signal would be useful for elucidating the contribution of multiple collagen fiber networks under load (Fig. 6.2). Further, SFDI has proved to be a reliable technique to build 3-dimensional topographic representations of soft tissue structures, which would be of great benefit for multiscale models and biaxial testing simulations. We expect this portion of our opto-mechanical system to provide robust quantifications of the varied microstructure, however these observations were outside the scope of this thesis.

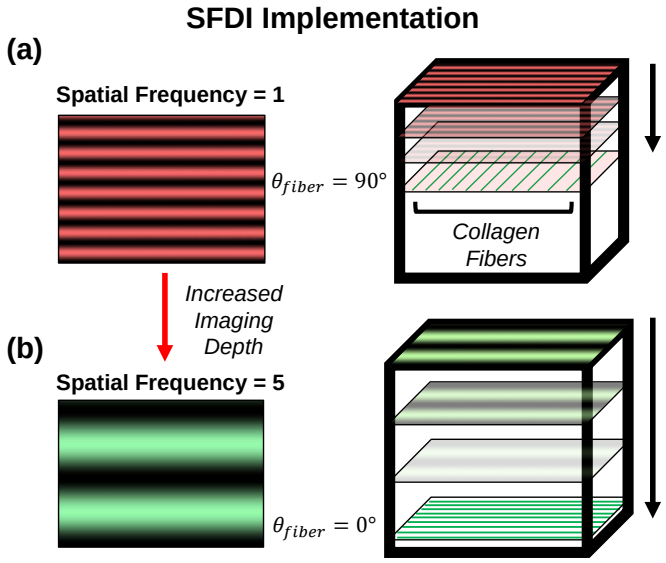

FIGURE 6.2 The SFDI technique used to quantify the collagen fiber orientation at (a) halfway through the specimen and (b) through the thickness by altering the spatial frequency pattern.

6.2.2 Further Collagenous Soft Tissue Testing

To compliment the characterizations provided for the HV leaflets, our groups plans to extend this pSFDI-based approach towards investigating other cardiovascular tissues, such as the coronary arteries. Microstructural and mechanical characterizations for these vessels are of great importance for creating bio-mimetic materials that rely heavily on fiber alignment and orientation to facilitate similar *in vivo* function. Other useful studies would include mechanical and microstructural testing for the right ventricular myocardium, which has also been shown to be affected by many TV diseases and pathologies. This mutliscale information could then be implemented into *in silico* models and enhance the current understanding of right ventricular failure that may be linked to TV regurgitation. In both cases, our proposed framework will lead to developments both within industry and in the clinical setting in treating various cardiovascular diseases.

6.2.3 Application Towards Tissue Engineering

’ Optimal development of tissue engineered heart valves (TEHVs) rely heavily on various factors, such as the cell phenotype, mechanical cues, and the scaffolding material used. Typically, techniques such as electrospinning (ES) are used to create highly aligned fiber networks that mimic the ECM of the native valve, however, current techniques have fallen short of matching the long-term efficacy of mechanical heart valves. Using the opto-mechanical system outlined in this thesis research, ES techniques could be further refined by examining the alignment and orientation of birefringent fibers (e.g., polycaprolactone, polyethylene oxide) in ES scaffolds. Proper fiber alignment and anisotropic mechanical properties in these scaffolds is important to the ECM morphology and smooth muscle phenotype throughout the development, therefore informing ES techniques through pSFDI would be of great value. Additive manufacturing techniques, such as 3D printing, have also played a role in the advancement of TEHVs. Traditionally, CT scan data is used to recreate the native valve geometry, but does not consider the underlying ECM or collagenous microstructure of the heart valve leaflets. Incorporating these novel printing techniques with pSFDI-based bulk-tissue characterizations, therefore, could further expand the implementation of additive manufacturing towards TEHVs.

6.2.4 Development and Refinement of Computational HV Models

As iterated throughout this thesis, the incorporation of the spatially varied, load-dependent CFA into the constitutive model development will help create more accurate representations of valvular function compared to existing models based homogenous assumptions. Moreover, these observations can be incorporated with previous studies in our lab, which examined the spatial and layer-specific mechanical variation in HV leaflet. Computational models that more accurately capture the bulk-tissue response in turn can be used to evaluate the efficacy of clinical therapeutics for valvular disease, such as annulolasty surgical repair or valve suturing techniques. Similarly, these models can guide manufacturing techniques for the development of tissue-engineered heart valves, evaluating efficacy and performance in computational simulations.

A BIAXIAL MECHANICAL TESTING PROCEDURES

In Appendix A, the detailed procedures for biaxial mechanical testing of the AHV leaflets and SHV cusps are described.

A.1 Tissue Acquisition and Preparation

(1.1) Retrieve the animal hearts on the same day as the slaughter, store the hearts in an ice chest, and transport them to the lab space.

(1.2) Prior to dissection, place a surgical underpad on the countertop and duct tape the edges to the surface to prevent sliding throughout the dissection process. Retrieve fresh razor blade, surgical forceps, and containers for the excised tissues.

(1.3) Remove a heart from ice chest and rinse any remaining blood with phosphate buffered saline (PBS) solution and place on the underpad. Using the forceps, remove any blood clots present in the artia or ventricles of the heart.

(1.4) Observe the heart from a top-down (superior) view and create axial incisions at the posterior commissure of the MV and the postero-septal commissure of the TV. Continue these excisions through the ventricle (downwards) and towards the apex of the heart (Fig. A.1a,b).

(1.5) Fold open the left ventricle and identify the MV anterior and posterior leaflets (Fig. A.1c). Grasp each leaflet with the forceps and sever all chordae tendineae attachments.

(1.6) With the forceps, stretch the leaflets taut orthogonal from the ventricular surface and slice the leaflet along the annular attachment. Place each leaflet in a labeled container and store in the freezer at $-20\,^{\circ}\mathrm{C}$.

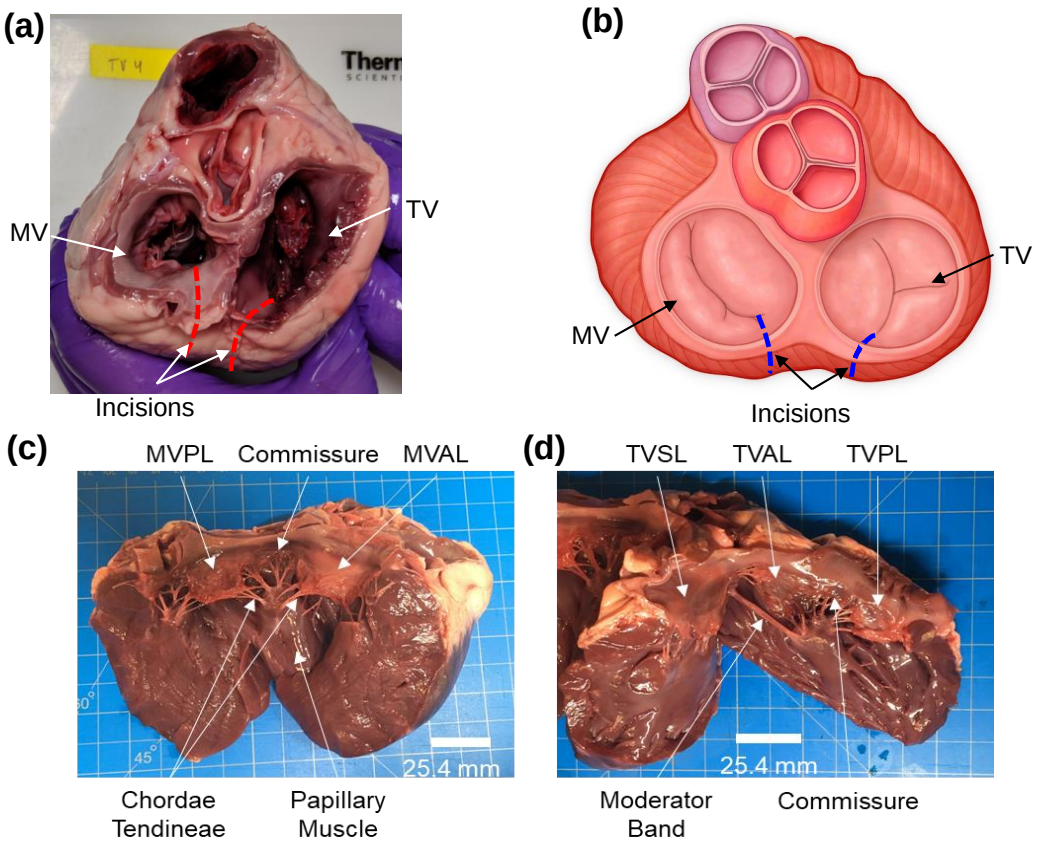

FIGURE A.1 (a-b) A top-down (superior) view of the heart showing incision lines along the MV and TV commissures. (c-d) Show the mitral and tricupsid valves fully opened prior to leaflet dissection (image adapted from [50]).

(1.7) Fold open the right ventricle and identify the TV anterior, posterior, and septal leaflets (Fig. A.1d). Extract each leaflet as detailed in Steps 1.5 and 1.6, place them in labeled containers, and store in the freezer at $-20\,^{\circ}$C.

(1.8) Place the heart in a top-down view and use the forceps to hold remaining portions of the aorta taut. Cut the remaining portion of the aorta just above the aortic valve and identify the AV left coronary, right coronary, and non-coronary cusps.

(1.9) Use the forceps to stretch each cusp away from the attachment to the wall of the vessel, expanding the sinus located behind the cusp (Fig. A.2a). Slice along the cusp attachment along the vessel wall, following the scalloped shaped pattern, place each cusp into a labeled container, and store in the freezer at $-20\,^{\circ}$C (Fig. A.2b).

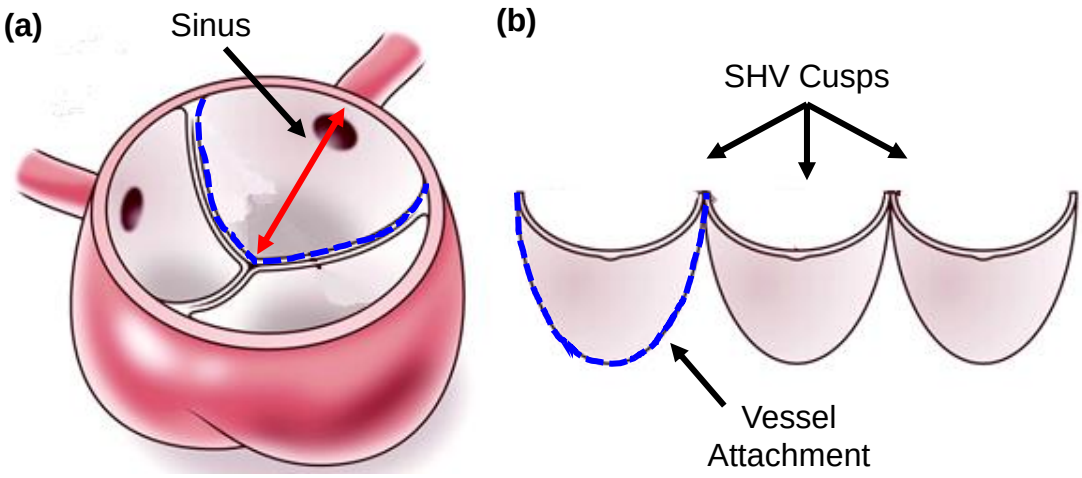

FIGURE A.2 (a) Schematic showing extension of the SHV cusp sinus (red arrow), and the attachment to the vessel wall (blue dotted line). (b) Each cusp is carefully removed by cutting along the vessel attachment (blue dotted line).

(1.10) Placing the heart again in a top-down view, use the forceps to extend the remaining ascending pulmonary artery. Remove the remaining tissue just above the pulmonary valve and identify the PV left, right, and anterior cusps.

(1.11) Carefully extract each cusp as detailed in Step 1.10, making sure not to damage the tissue. Store the cusps in the freezer at $-20\,^{\circ}$C prior to test.

A.2 Tissue Thickness and Sectioning

(2.1) Retrieve a leaflet (or cusp) from the fridge along with a cutting mat, forceps, razor blade, surgical ruler, and a surgical pen.

(2.2) Place the container on the cutting board, remove the cap, and fill the container with PBS to help thaw the leaflet. Once thawed, arrange the leaflet with the forceps on the cutting board so that the radial direction (Rad.) is aligned to the Y-direction, and the circumferential direction (Circ.) aligned to the X-direction (Fig. A.3a).

(2.3) For AHVs, remove any excess chordae tendineae that may cause problems for testing. Identify the center portion of the specimen, and use the surgical ruler and razor blade to cut a square sample of desired dimensions from the belly region of the tissue (Fig. A.3b).

(2.4) Using the surgical pen, mark the top right corner of the specimen to denote proper orientation throughout testing.

(2.5) Once marked with surgical pen, ensure that the excised portion of the leaflet remains flat on the cutting board. Retrieve and plug-in the non-contact laser displacement sensor (Keyence IL-030, Itaska, IL).

(2.6) Hover the laser sensor over the cutting board away from the tissue and press ”Zero Shift” to calibrate the device. Next, slide the sensor over the leaflet and record 3 different thickness measurements in the center of the excised square in a triangular formation. Record these measurements in an Excel spreadsheet.

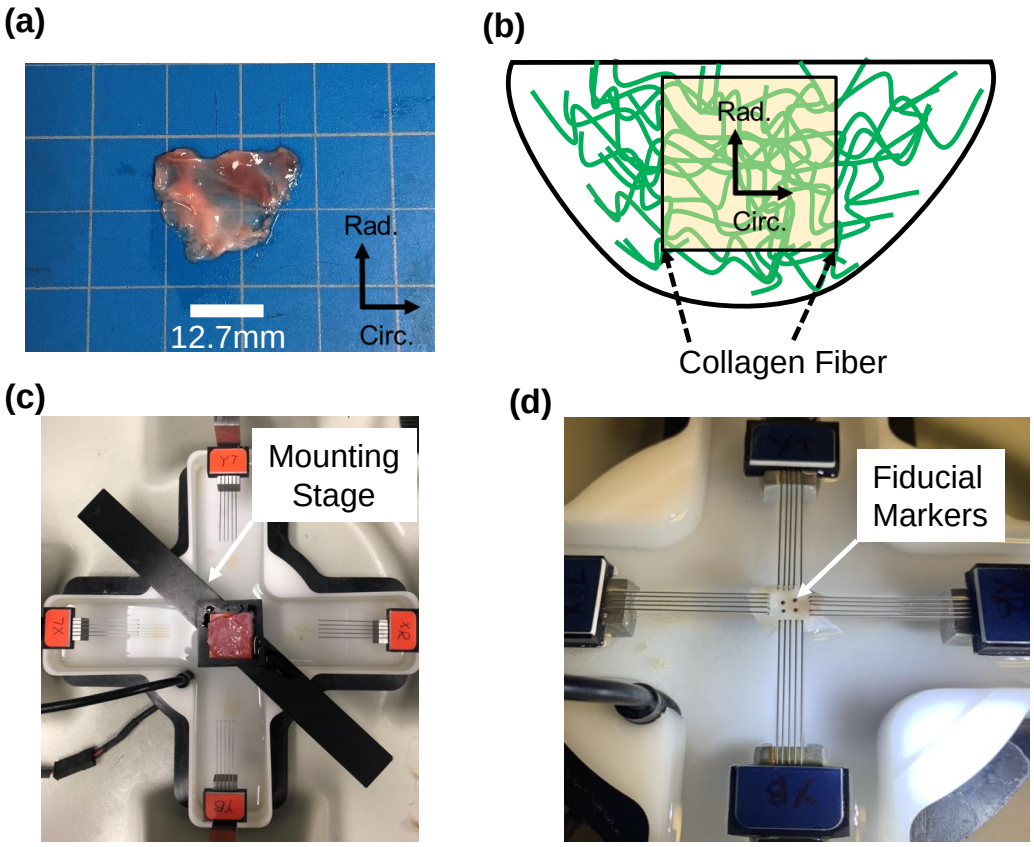

FIGURE A.3 (a) Prior to testing, the leaflet is thawed and the circumferential and radial directions are identified. (b) A square portion is extracted frm the belly region of the leaflet and (c) placed on a mounting stage above the PBS bath. (d) The leaflet is mounted and fiducial markers are placed in a 2x2 array in the center portion of the tissue.

A.3 Tissue Mounting and Fiducial Marker Placement

(3.1) Prepare a PBS bath at $37\,^{\circ}$C, which is correspondent to the tissue's physiologic conditions.

(3.2) Retrieve the mounting stage and place a drop of PBS on the rubber backing material to prevent shrinkage and friction during mounting. Place the leaflet on the rubber portion of the stage while keeping the original orientation .

(3.3) Ensure that the biaxial testing tines are set to appropriate dimensions, and that the tines are in line with one another.

(3.4) Place the mounting stage on the biaxial testing bath diagonally, and raise the bath and mounting stage so that the leaflet is center between each set of tines. While mounting, ensure the tissue's circumferential and radial directions are aligned with the machine's X- and Y-directions, respectively (Fig. A.3c).

(3.5) Raise the mounting stage until the BioRake tines penetrate the tissue, providing slight tension in each tissue direction. Using the forceps, lightly press each tine into the leaflet.

(3.6) Once mounted, retrieve the glass beads, fine-tipped tool, and super glue. Using the fine-tipped too, coat the tip with a small amount of super glue and stick an individual bead to the tip of the tool.

(3.7) Carefully use the tool to place the bed to one corner of the middle third of the tissue's testing region, and repeat this step until a 2x2 square array of four beads is formed (Fig. A.3d). Glass beads should be placed in between the 2nd and 3rd tine and between the 3rd and 4th tine respectively for all of the tines which will form a square.

(3.8) Ensure that there is no excess glue that would cause the glass beads to remain stuck together before dismounting. When dismounting from the mounting stage, place the forceps underneath the tissue to help separation from the rubber backing. This prevents some of the slippage that can be cause when just grabbing the tines. Lower the mounting stage/PBS bath while dismounting to help generate the separation.

A.4 Preconditioning and Timing Step

(4.1) Raise the PBS bath so that the leaflet is fully submerged (add PBS if not fully submerged). Situate the lights attached to the mechanical tester over the leaflet so that the glass beads are visible for the camera.

(4.2) A testing template (.tmt) for preconditioning can be built manually in the LabJoy software (CellScale, Canada), or through programming languages such as MATLAB. Generate a preconditioning template consisting of ten loading/unloading cycles that target a peak membrane tension or stress including a preload of 2.5% of the maximum load applied to the specimen.

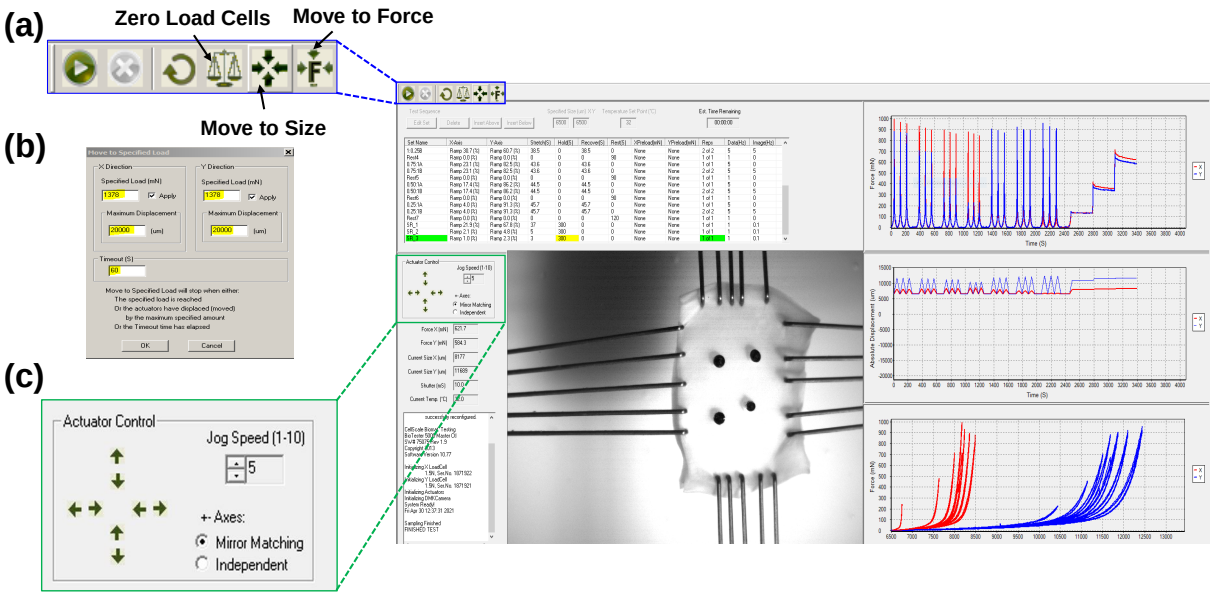

FIGURE A.4 Overview of the LabJoy software used for biaxial mechanical testing. (a) The top toolbar is used to displace the specimen to a defined size or force reading and zero the load cells prior to testing. (b) When moving the specimen to a particular force, the user is able to input the specified load in the X- and Y-directions and set maximum displacement values. (c) The actuators can be controlled manually through the actuator control panel, and the jog speed and axis displacement can be modified.

(4.3) Create a new testing directory to store the preconditioning information, and store the test in the appropriate data directory. Ensure that the mounting dimensions for

the leaflet are set through the 'Move to Size' feature and press 'Zero Load Cells'. Perform preconditioning and record the final size at the end of the protocol in the Excel sheet (Fig. A.4a).

(4.4) Retrieve a stopwatch for timing purposes. Click on the 'Move to Force' button, and set the 'Specified Load' in the X- and Y-directions to the maximum membrane tension or stress indicated by the Excel sheet for equibiaxial loading ($1{:}1$). Add $3-4$ zeroes to the 'Maximum Displacement' in both directions to ensure the biaxial tester does not time out (Fig. A.4b).

(4.5) Press the green 'Execute' button and start the stopwatch simultaneously when the actuators begin to displace the tissue. Stop the stopwatch when the actuators have moved the specimen to peak loading, this will be evident through auditory cues. Record the time and size of the specimen in the Excel spreadsheet.

(4.6) For the remaining biaxial testing protocols ($1{:}0.75$, $1{:}0.5$, $1{:}0.25$, $0.75{:}1$, $0.5{:}1$, $0.25{:}1$), jog the actuators to meet the desired force in the X- and Y-directions and record the size of the specimen for each protocol (Fig. A.4c). The projected time for each biaxial testing protocol is calculated by multiplying the time to equibiaxial load (Step 4.5) by the ratio between the equibiaxial specimen size to the size of the specimen at the desired loading protocol.

(4.7) Move the specimen to the mounting configuration and zero the load cells. A testing template for mechanical testing can be built manually in the Labjoy software or through MATLAB programming. Generate a mechanical testing template consisting of the biaxial testing loading protocols, recorded size of the leaflet at each protocol, and the time till maximum force for each biaxial protocol.

A.5 Study Specific Biaxial Testing Procedures

This thesis presented the results of various biaxial mechanical studies for the four HVs. Due to the size, composition, and position within the heart, each study consisted of individualized biaxial testing procedures. The breakdown of these studies are as follows:

(i) *Tricuspid Valve Leaflet Study (Section 3.2)*: The center portion of each tissue in this pilot study was sectioned to a 11.5×11.5 mm square. Using the BioRake tines, and effective testing region of 10×10 mm was used to capture the mechanical

response. A preconditioning protocol was utilized with six equibiaxial and non-equibiaxial loading/unloading cycles that target peak membrane tension of 25 N/m. Biaxial tension protocols were each applied for three loading/unloading cycles, and the forces and displacements were recorded at 5 Hz.

(ii) *Mitral Valve Leaflet Study (Section 4.2)*: In this study, a 7.5×7.5 mm square from the center portion of each mitral valve leaflet was extracted. An effective testing region of 6.5×6.5 mm was used for mechanical testing, and a pre-conditioning protocol consisting of 10 loading/unloading cycles was applied to the tissue with a target membrane tension of 150 N/m. All biaxial testing protocols were repeated for three load/unloading cycles, and the load cell force readings and CCD images (15 Hz) were acquired throughout each biaxial testing procedure.

(iii) *Aortic and Pulomonary Valve Studies (Section 5.2)*: For the SHVs, a 7.5×7.5 mm square from the center portion of each cusp was extracted and an effective testing region of 6.5×6.5 mm was used for mechanical testing. A preconditioning protocol, consisting of six loading/unloading cycles at a target first Piola-Kirchhoff peak stress $P_{\max}$ of 240 kPa was employed prior to biaxial testing. Each protocol was repeated for three loading/unloading cycles, and force readings from the load cells and CCD camera images were recorded at 15 Hz throughout the test.

B POLARIZED SPATIAL FREQUENCY DOMAING IMAGING (PSFDI) PROCEDURES

In Appendix B, the goal is to describe the physical set-up and calibration of the pSFDI-based system, and the subsequent imaging and post-processing procedures for HV leaflets

B.1 System Calibration

(1.1) After mechanical testing, identify the imaging points along the force-deformation curve that are of interest. Typical points of interest are outlined in Section 4.2, consisting of the mounting configuration, intermediate points within the toe region of the force-deformation curve, 30% of maximum equibiaxial load, and peak equibiaxial load.

(1.2) Rotate the CellScale camera (black pole) couterclockwise until it is no longer above the tissue (Fig. B.1a). Carefully remove the covers above each load cell, and position the pSFDI system above the biaxial testing system.

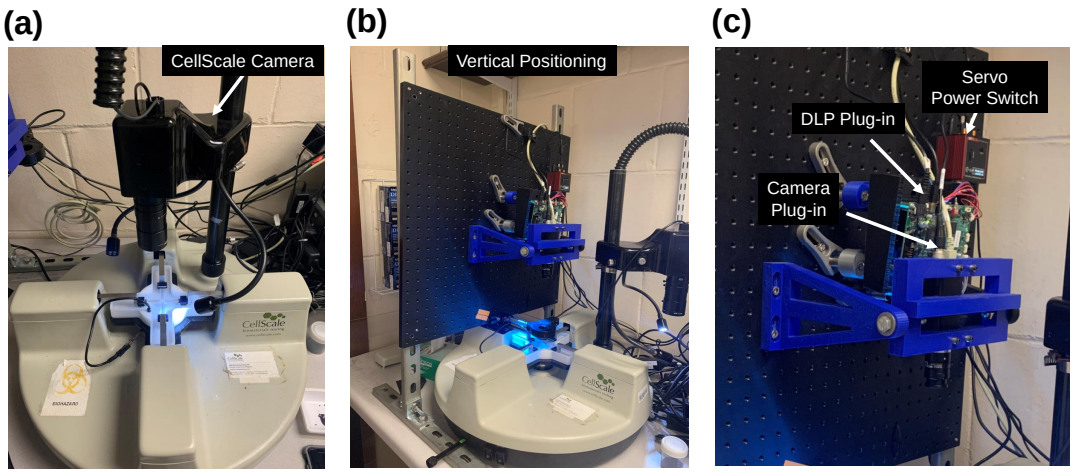

FIGURE B.1 (a) The CellScale camera is rotated counterclockwise before (b) vetical positioning of the pSFDI system above the biaxial tester. (c) The CCD camera, DLP projector, and servo motor are intiated prior to use of the pSFDI system.

(1.3) Slide the system until CCD camera (Basler, Germany) is directly above the tissue (Fig. B.1b). Proceed to plug in the DLP projector (Texas Instruments, Dallas, TX) and the CCD camera. On the red servo motor (Thorlabs, Inc., Newton, NJ), flip the red switch to the 'On' position (Fig. B.1c).

(1.4) Remove the linear polarizer and rotational mount (Thorlabs, Inc., Newton, NJ) from the storage position and place in the threaded holster at the bottom of the breadboard.

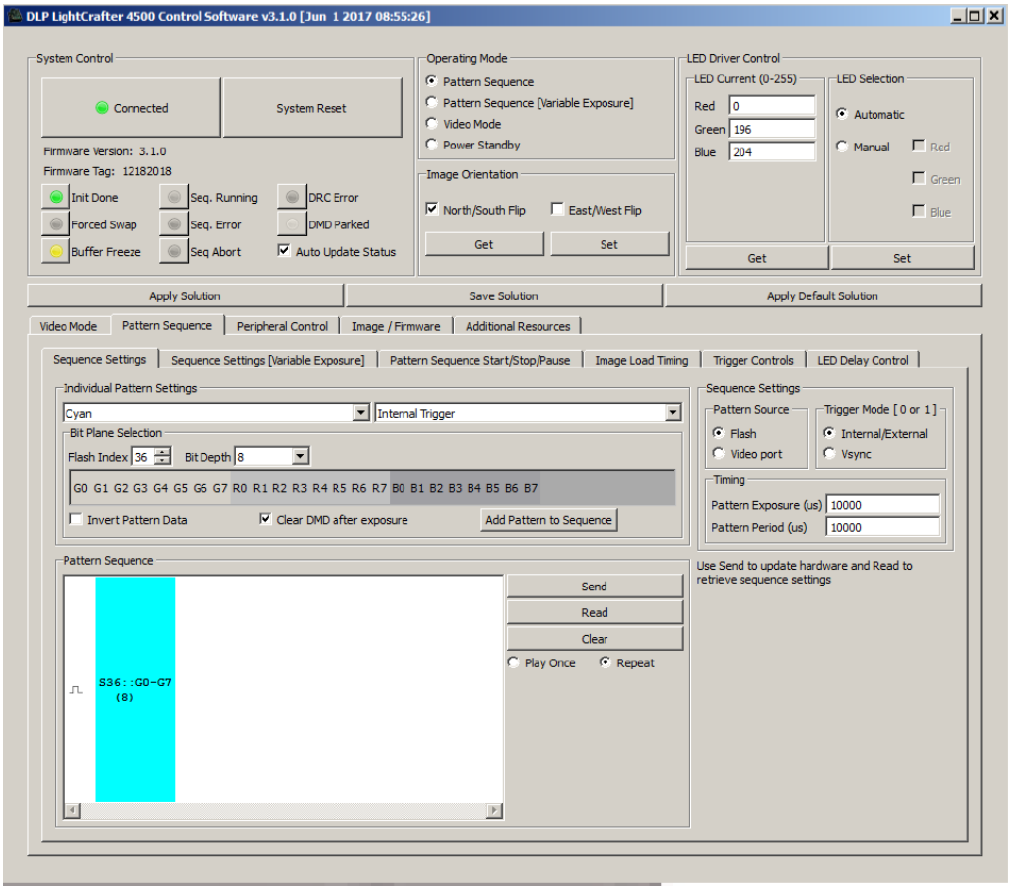

FIGURE B.2 The LigthCrafter software used to project incident cyan with a spatial frequency of 12.

(1.5) Open the LightCrafter software (Texas Instruments, Dallas, TX) and ensure the DLP projector is in 'Pattern Sequence Mode'. Adjust the LED values for cyan light (RGB: 0, 196, 204) and the individual pattern settings (flash index of 36, bit

depth of 8), hit 'Send' to project the proper striped, cyan light pattern on the tissue (Fig. B.2). The 'Flash Index' is subject to change if depth-modulated imaging is desired.

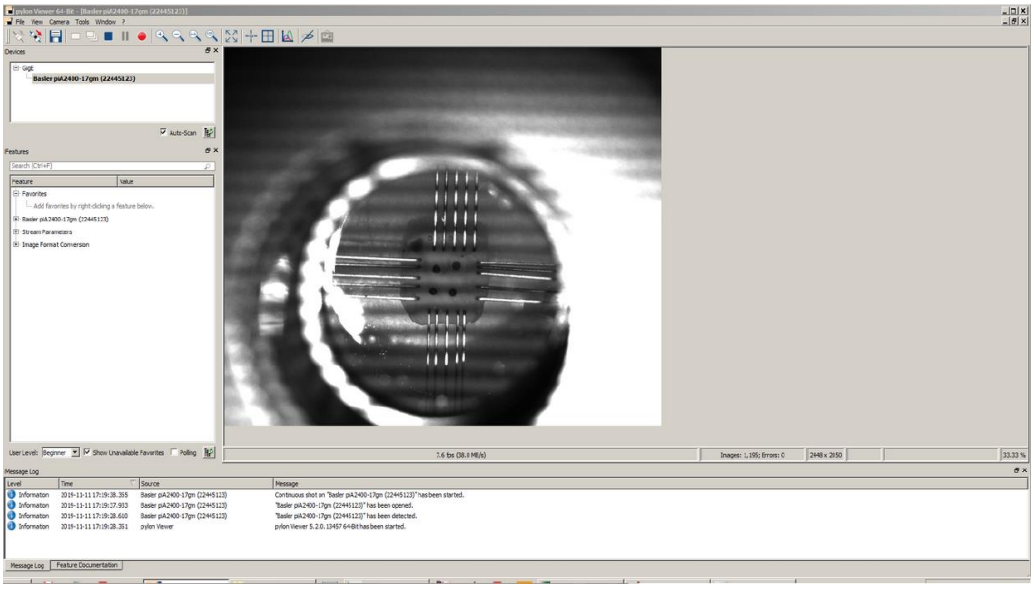

FIGURE B.3 The Pylon Viewer software to verify that the tissue is within the polarizer's field of view.

(1.6) Open the Pylon Viewer (Basler, Germany) application and double-click on the 'Basler piA2406' camera from the list. Select the red circle to begin sampling (Fig. B.3).

(1.7) Adjust the position of the pSFDI system so that the tissue is within the polarizer's view. If needed, adjust the brightness of the incident light by opening/closing the iris in front of the DLP projector (Fig. B.3).

(1.8) Check the polarizer lens for dust or other imperfections that could interfere with the pSFDI results. Manually rotate the polarizer using the red servo motor for $0°$ to $180°$ while observing the tissue within the camera software. If there are any imperfections, use a microfiber cloth and lens cleaning solution to clean the polarizer lens.

B.2 pSFDI Testing Procedures

This section presents a custom LabVIEW program (National Instruments, TX, USA) that captures the polarization-state images (2560×2048 pixels) for each phase shift in $5°$ increments, from $0°$ to $180°$ (Fig. B.4). The program inputs the *Test Name*, *Spatial Frequency Index*, *Camera* (if multiple camera are connected to the computer), *Step Size* ($5°$ increments), and *End Position* ($180°$ for our current studies). The name of the test and the spatial frequency index are typically the only parameters changed throughout the pSFDI procedure. For the purpose of this thesis research, a spatial frequency of 12 is used for all imaging points to ensure full penetration of the incident light patterns. To perform pSFDI for any given imaging point, this program is used as follows:

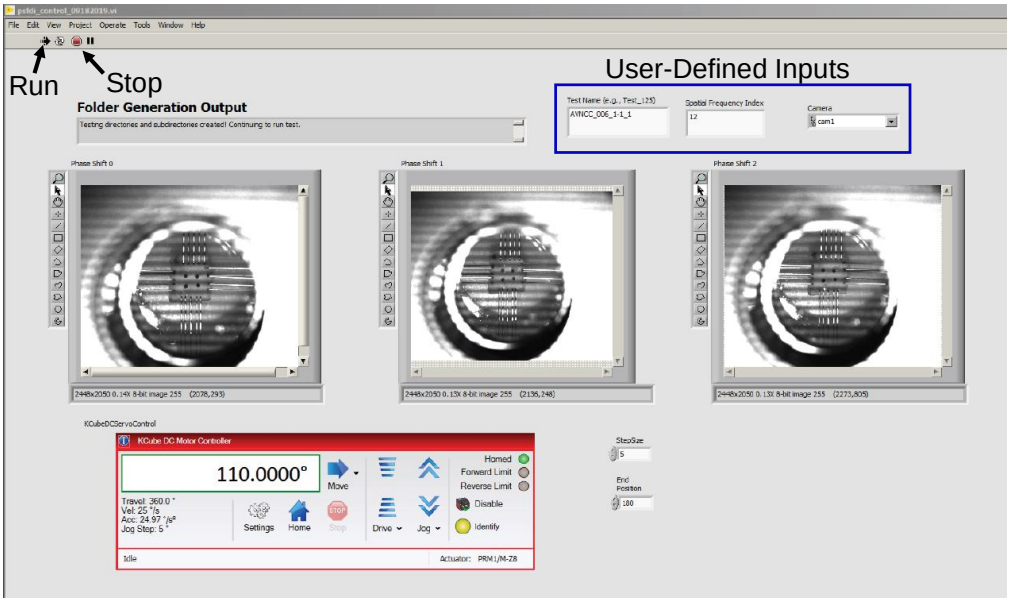

FIGURE B.4 In-house custom LabVIEW graphical user interface used for pSFDI quantification.

(2.1) Using the defined X- and Y-direction displacements that correspond to the imaging points along the force-deformation curve, press 'Move to Size' in the LabJoy software and input the tissue configuration.

(2.2) Input the 'Test Name' and the 'Spatial Frequency Index' for the first imaging point. Select the CCD camera from the 'Camera' drop-down menu (Fig. B.4).

(2.3) Click the 'Run' button in the LabVIEW software. The servo motor will rotate the polarizer to the 'Home' configuration at $0°$ (Fig. B.4).

(2.4) After the imaging process is complete ($45-50$seconds), click the 'Stop' button on the top toolbar.

(2.5) Repeat Steps 2.1-2.4 for all imaging points, moving the specimen to each defined size before imaging.

(2.6) Following the pSFDI procedure, the images can be analyzed using an in-house MATLAB program (MathWorks, MA, USA) as described in Section B.3, in accordance with the theory outlined in Section 3.2.3.

B.3 Post-Processing Analysis

In this section, the MATLAB processing scripts used to quantify the pSFDI information for each specimen is described. There are two primary steps in processing the pSFDI data: (i) selecting the region of interest (ROI) for each HV specimen; and (ii) quantifying the birefringent intensity response to extract the collagen fiber orientation and alignment. The ROI is defined using the user-created function *grabit.m* (available via MathWorks). First, the full tissue geometry is captured and stored as *capture_coor* - this region includes the regions outside and inside of the BioRake tines. Second, the geometry within the BioRake tines is selected and stored as *capture_coor_2*. Data processing begins once the file locations of the collected pSFDI images has been defined, and the images are read into the MATLAB script using the *imread()* built-in function:

```
temp_txt = ['spatial_freq_' num2str(sf_idx) '_'];

    folder1 = [test_folder test_name '/' temp_txt 'ps_0'];
    folder2 = [test_folder test_name '/' temp_txt 'ps_1'];
    folder3 = [test_folder test_name '/' temp_txt 'ps_2'];
     if ~exist(folder1)
        test_name_new{iitesting,2} = 'FAIL';
        continue
    end

    [X_temp_1,cmap1] = imread([folder1 '/image_' ...
  num2str((1-1)*5) '.tiff']);

    RI = imref2d(size(X_temp_1));
    temp1 = RI.XWorldLimits;
```

```
    temp2 = RI.YWorldLimits;
  [X_temp_1] = imread([folder1 '/image_' num2str((1-1)*5) '.tiff']);

    RI = imref2d(size(X_temp_1));


    II_1 = zeros(37, RI.ImageExtentInWorldY, RI.ImageExtentInWorldX);
    II_2 = zeros(37, RI.ImageExtentInWorldY, RI.ImageExtentInWorldX);
    II_3 = zeros(37, RI.ImageExtentInWorldY, RI.ImageExtentInWorldX);


    for ii = 1:37
        fprintf('ii = %d,  ', ii);

        [X_temp_1] = imread([folder1 '/image_' num2str((ii-1)*5) '.tiff']);
        [X_temp_2] = imread([folder2 '/image_' num2str((ii-1)*5) '.tiff']);
        [X_temp_3] = imread([folder3 '/image_' num2str((ii-1)*5) '.tiff']);


        II_1(ii, :, :) = (X_temp_1); % I_0
        II_2(ii, :, :) = (X_temp_2); % I_120
        II_3(ii, :, :) = (X_temp_3); % I_240

        if mod(ii,5) == 0  ii == 37
            fprintf('\n');
        end
    end

    clear X_temp_1  X_temp_2  X_temp_3

```

Next, an ID mask is created to identify the pixels within the images associated with the ROI of the tissue (*capture_coor*). The pixels within this ROI will provide our reported values and quantifications of the CFA under load:

```
capture_coor = [capture_coor; capture_coor(1,:)];

    id_mask = zeros(RI.ImageExtentInWorldY, RI.ImageExtentInWorldX);

    [bb, cc] = size(id_mask);
```

```
51
52      [xx1_temp yy1_temp] = meshgrid(1:1:bb, 1:1:cc);
53
54      xx1 = reshape(xx1_temp, [bb*cc 1]);
55      yy1 = reshape(yy1_temp, [bb*cc 1]);
56
57      point_in = inpolygon(xx1, yy1, capture_coor(:,1), capture_coor(:,2));
58
59      info_in = find(point_in == 1);
60
```

Smoothing is performed on the collected data using a user-defined (*smoothing_window*) parameter and pSFDI-based parameters are loaded into the MATLAB enviorment for subsequent calculations:

```
61 load(['PSFDI_Auxiliary/neighbor_list_' num2str(smoothing_window) '.mat'])
62
63      id_list = id_list(info_in(:,1), :);
64
65      ifac_AC = sqrt(2)/3;  ifac_DC = 1/3;
66      theta = 0:5:180;
67
68      nid_process = length(info_in(:,1));
69
70      II_DC = zeros(37, nid_process);
71      DC_par = zeros(8, nid_process);
72
73      II_1_grid = zeros(37, nid_process);
74      II_2_grid = zeros(37, nid_process);
75      II_3_grid = zeros(37, nid_process);
76
77
78      II_AC = zeros(37, nid_process);
79      AC_par = zeros(8, nid_process);
```

After smoothing, each image was then combined at each pixel and a linear least-squares regression is used to fit the data, and the three Fourier series coefficients were extracted:

```
80 for ii = 1:nid_process
81          if mod(ii, 50000) == 0
```

```
            fprintf('ii = %d \n', ii);
        end



        nn_temp = 0;
        I1_temp = zeros(37, 1);  I2_temp = zeros(37, 1);  I3_temp = zeros
    (37, 1);

        for jj = 1:id_list(ii,1)
            jj_id = id_list(ii, jj+1);

            if point_in(jj_id, 1) == 1
                nn_temp = nn_temp + 1;
                aa_temp = point_in(jj_id,3);  bb_temp = point_in(jj_id,2);

                I1_temp = I1_temp + II_1(:, aa_temp, bb_temp);
                I2_temp = I2_temp + II_2(:, aa_temp, bb_temp);
                I3_temp = I3_temp + II_3(:, aa_temp, bb_temp);
            end

        end

        if idddd > 0
            I1_temp = [I1_temp(idddd+1:end); I1_temp(1:idddd)];
            I2_temp = [I2_temp(idddd+1:end); I2_temp(1:idddd)];
            I3_temp = [I3_temp(idddd+1:end); I3_temp(1:idddd)];

        elseif idddd < 0
            idddd = abs(idddd); %quick correction
            I1_temp = [I1_temp(end-idddd+1:end); I1_temp(1:end-idddd)];
            I2_temp = [I2_temp(end-idddd+1:end); I2_temp(1:end-idddd)];
            I3_temp = [I3_temp(end-idddd+1:end); I3_temp(1:end-idddd)];
            idddd = -idddd;
        end

        ifac_temp = 1 / nn_temp;

        I1_temp = I1_temp * ifac_temp;
        I2_temp = I2_temp * ifac_temp;
        I3_temp = I3_temp * ifac_temp;
```

```
121
122         II_1_grid(:, ii) = I1_temp;
123         II_2_grid(:, ii) = I2_temp;
124         II_3_grid(:, ii) = I3_temp;
125
126
127
128         II_DC(:, ii) = (I1_temp + I2_temp + I3_temp) * ifac_DC;
129
130         [theta_fiber, DOA_1, DOA_2, beta] = ...
131     user_LLSR(II_DC(:, ii)', theta);
132
133         DC_par(:, ii) = [theta_fiber, DOA_1, DOA_2, beta']';
134         mod(DC_par(1,:)+90,180);
135
136         II_AC(:, ii) = sqrt((I1_temp - I2_temp).^2 + ...
137             (I2_temp - I3_temp).^2 + ...
138             (I3_temp - I1_temp).^2) * ifac_AC;
139
140         [theta_fiber, DOA_1, DOA_2, beta] = ...
141     user_LLSR(II_AC(:, ii)', theta);
142
143         AC_par(:, ii) = [theta_fiber, DOA_1, DOA_2, beta']';
144     end
```

Lastly, the polygon defined by the selected ROI is saved for data visualization purposes:

```
145
146 clear xxx yyy tri cg ROI_poly tri_bool tri_ID
147
148     xxx = info_in(:,2);
149     yyy = info_in(:,3);
150
151
152     tri = delaunay(xxx, yyy);
153
154     cg(:,1) = (xxx(tri(:,1),1) + xxx(tri(:,2),1) + xxx(tri(:,3),1))/3;
155     cg(:,2) = (yyy(tri(:,1),1) + yyy(tri(:,2),1) + yyy(tri(:,3),1))/3;
156
157     ROI_poly = polyshape(capture_coor(:,1), capture_coor(:,2));
158
```

```
159     tri_bool = isinterior(ROI_poly, cg(:,1), cg(:,2));
160     tri_ID = find(tri_bool(:,1) == true);
161 
162     tri = tri(tri_ID,:);
```

REFERENCES

1. Tretter, J., Sarwark, A., Anderson, R. & Spicer, D. ”Assessment of the Anatomical Variation to be found in the Normal Tricuspid Valve”. *Clinical Anatomy* **29,** 399–407 (2016).
2. Krawczyk-Ożóg, A., Hołda, M. K., Sorysz, D., Koziej, M., Siudak, Z., Dudek, D. & Klimek-Piotrowska, W. ”Morphologic Variability of the Mitral Valve Leaflets”. *The Journal of Thoracic and Cardiovascular Surgery* **154,** 1927–1935 (2017).
3. Sell, S. & Scully, R. E. ”Aging Changes in the Aortic and Mitral Valves”. *The American Journal of Pathology* **46,** 345–365 (1965).
4. Waller, B. F., Howard, J. & Fess, S. ”Pathology of Tricuspid Valve Stenosis and Pure Tricuspid Regurgitation—Part I”. *The American Journal of Pathology* **18,** 97–102 (1995).
5. Cheitlin, M. D. ”Cardiovascular Physiology—Changes With Aging”. *The American Journal of Pathology* **12,** 9–13 (2003).
6. De Paulis, R., Salica, A., Pisani, G., Morbiducci, U., Weltert, L. & Maselli, D. ”Hemodynamics of the Aortic Valve and Root: Implications for Surgery”. *Annals of Cardiothoracic Surgery* **2,** 40–43 (2013).
7. Pisani, G., Scaffa, R., Ieropoli, O., Dell’Amico, E. M., Maselli, D., Morbiducci, U. & De Paulis, R. ”Role of the Sinuses of Valsalva on the Opening of the Aortic Valve”. *The Journal of Thoracic and Cardiovascular Surgery* **145,** 999–1003 (2013).
8. Rabbah, J.-P. M., Saikrishnan, N., Siefert, A. W., Santhanakrishnan, A. & Yoganathan, A. P. ”Mechanics of Healthy and Functionally Diseased Mitral Valves: A Critical Review”. *Journal of Biomechanical Engineering* **135** (2013).
9. Kramer, K. E., Ross, C. J., Laurence, D. W., Babu, A. R., Wu, Y., Towner, R. A., Mir, A., Burkhart, H. M. & Holzapfel Gerhard A.and Lee, C.-H. ”An Investigation of Layer-Specific Tissue Biomechanics of Porcine Atrioventricular Heart Valve Leaflets”. *Acta Biomaterialia* **96,** 368–384 (2019).

10. Jett, S. V., Laurence, D. W., Kunkel, R. P., Babu, A. R., Kramer, K. E., Baumwart, R., Towner, R., Wu, Y. & Lee, C.-H. ”An Investigation of the Anisotropic Mechanical Properties and Anatomical Structure of Porcine Atrioventricular Heart Valves”. *Journal of the Mechanical Behavior of Biomedical Materials* **87,** 155–171 (2018).

11. Stephens, E. H., Chu, C.-K. & Grande-Allen, K. J. ”Valve Proteoglycan Content and Glycosaminoglycan Fine Structure Are Unique to Microstructure, Mechanical Load and Age: Relevance to an Age-Specific Tissue-Engineered Heart Valve”. *Acta Biomaterialia* **4,** 1148–1160 (2008).

12. Tseng, H. & Grande-Allen, K. J. ”Elastic Fibers in the Aortic Valve Spongiosa: A Fresh Perspective on its Structure and Role in Overall Tissue Function”. *Acta Biomaterialia* **7,** 2101–2108 (2011).

13. Stella, J. A. & Sacks, M. S. ”On the Biaxial Mechanical Properties of the Layers of the Aortic Valve Leaflet”. *Journal of Biomechanical Engineering* **129,** 757–766 (2007).

14. Misfeld, M. & Sievers, H.-H. ”Heart Valve Macro- and Microstructure”. *Philosophical transactions of the Royal Society of London. Series B, Biological sciences* **362,** 1421–71436 (2007).

15. Stradins, P., Lacis, R., Ozolanta, I., Purina, B., Ose, V., Feldmane, L. & Kasyanov, V. ”Comparison of Biomechanical and Structural Properties Between Human Aortic and Pulmonary Valve”. *European Journal of Cardio-Thoracic Surgery* **26,** 634–639 (2004).

16. Scott, M. & Vesely, I. ”Aortic Valve Cusp Microstructure: The Role of Elastin”. *The Annals of Thoracic Surgery* **60,** 391–394 (1995).

17. Latif, N., Sarathchandra, P., Taylor, P. M., Antoniw, J. & Yacoub, M. H. ”Localization and Pattern of Expression of Extracellular Matrix Components in Human Heart Valves”. *The Journal of Heart Valve Disease* **14,** 218–227 (2005).

18. Delling, F. N. & Vasan, R. S. ”Epidemiology and Pathophysiology of Mitral Valve Prolapse: New Insights into Disease Progression, Genetics, and Molecular basis”. *Circulation* **129,** 2158–2170 (2014).

19. Stuge, O. & Liddicoat, J. ”Emerging Opportunities for Cardiac Surgeons within Structural Heart Disease”. *The Journal of Thoracic and Cardiovascular Surgery* **132,** 1258–1261 (2006).

20. Bach, D. S., Radeva, J. I., Birnbaum, H. G., Fournier, A.-A. & Tuttle, E. G. ”Prevalence, Referral Patterns, Testing, and Surgery in Aortic Valve Disease: Leaving Women and Elderly Patients Behind”. *The Journal of Heart Valve Disease* **16,** 362–369 (2007).

21. Apostolidou, E., Maslow, A. D. & Poppas, A. ”Primary Mitral Valve Regurgitation: Update and Review”. *Global Cardiology Science and Practice* **2017,** e201703 (2017).

22. Prihadi, E. A., Delgado, V., Leon, M. B., Enriquez-Sarano, M., Topilsky, Y. & Bax, J. J. ”Primary Mitral Valve Regurgitation: Update and Review”. *JACC: Cardiovascular Imaging* **12,** 491–499 (2019).

23. Singh, G. K. ”Congenital Aortic Valve Stenosis”. *Children* **6,** 69 (2019).

24. Maurer, G. ”Aortic Regurgitation”. *Heart* **92,** 994–1000 (2006).

25. Corno, A. F. ”Pulmonary Valve Regurgitation: Neither Interventional Nor Surgery Fits All”. *Frontiers in Pediatrics* **6,** 69 (2018).

26. Idrizi, S., Milev, I., Zafirovska, P., Tosheski, G., Zimbakov, Z., Ampova-Sokolov, V., Angjuseva, T. & Mitrev, Z. ”Interventional Treatment of Pulmonary Valve Stenosis: A Single Center Experience”. *Open Access Macedonian Journal of Medical Sciences* **6,** 408–412 (2015).

27. Salgo, I. S., Gorman, J. H., Gorman, R. C., Jackson, B. M., Bowen, F. W., Plappert, T. & St John Sutton, M. G. ”Effect of Annular Shape on Leaflet Curvature in Reducing Mitral Leaflet Stress”. *Circulation* **106,** 711–717 (2020).

28. Padala, M., Hutchison, R. A., Croft, L. R., Jimenez, J. H., Gorman, R. C., Gorman, J. H., Sacks, M. S. & Yoganathan, A. P. ”Saddle Shape of the Mitral Annulus Reduces Systolic Strains on the P2 Segment of the Posterior Mitral Leaflet”. *The Annals of Thoracic Surgery* **88,** 1499–1504 (2009).

29. Rausch, M. K., Mathur, M. & Meador, W. D. ”Biomechanics of the Tricuspid Annulus: A Review of the Annulus’ in vivo Dynamics with Emphasis on Ovine Data”. *GAMM-Mitteilungen* **42,** e201900012 (2019).

30. Matthews, P. B., Azadani, A. N., Jhun, C., Ge, L., Guccione, J. M. & Tseng, E. E. ”Comparison of Porcine Pulmonary and Aortic Root Material Properties”. *The Annals of Thoracic Surgery* **89,** 1981–1988 (2010).

31. Schwartz, M. L., Gauvreau, K., del Nido, P., Mayer, J. E. & Colan, S. D. ”Long-Term Predictors of Aortic Root Dilation and Aortic Regurgitation After Arterial Switch Operation”. *Circulation* **110,** 128–132 (2004).

32. Youssefi, P., El-Hamamsy, I. & Lansac, E. ”Rationale for Aortic Annuloplasty to Standardise Aortic Valve Repair”. *Annals of Cardiothoracic Surgery* **8** (2019).

33. Pozzoli, A., Elisabetta, L., Vicentini, L., Alfieri, O. & De Bonis, M. ”Surgical Indication for Functional Tricuspid Regurgitation at Initial Operation: Judging from Long Term Outcomes”. *General Thoracic and Cardiovascular Surgery* **64,** 509–516 (2016).

34. Huang, X., Gu, C., Men, X., Zhang, J., You, B., Zhang, H., Wei, H. & Li, J. ”Repair of Functional Tricuspid Regurgitation: Comparison between Suture Annuloplasty and Rings Annuloplasty”. *General Thoracic and Cardiovascular Surgery* **97,** 1286–1292 (2014).

35. Vassileva, C. M., Boley, T., Markwell, S. & Hazelrigg, S. ”Meta-Analysis of Short-Term and Long-Term Survival Following Repair Versus Replacement for Ischemic Mitral Regurgitation”. *European Journal of Cardio-Thoracic Surgery* **39,** 295–303 (2010).

36. Lansac, E., Di Centa, I., Sleilaty, G., Lejeune, S., Khelil, N., Berrebi, A., Diakov, C., Mankoubi, L., Malergue, M.-C., Noghin, M., Zannis, K., Salvi, S., Dervanian, P. & Debauchez, M. ”Long-Term Results of External Aortic Ring Annuloplasty for Aortic Valve Repair”. *European Journal of Cardio-Thoracic Surgery* **50,** 350–360 (2016).

37. Falk, V., Seeburger, J., Czesla, M., Borger, M. A., Willige, J., Kuntze, T., Doll, N., Borger, F., Perrier, P. & Mohr, F. W. ”How Does the Use of Polytetrafluoroethylene Neochordae for Posterior Mitral Valve Prolapse (Loop Technique) Compare with Leaflet Resection? A Prospective Randomized Trial”. *The Journal of Thoracic and Cardiovascular Surgery* **136,** 1200–1206 (2008).

38. Salvador, L., Mirone, S., Bianchini, R., Regesta, T., Patelli, F., Minniti, G., Masat, M., Cavarretta, E. & Valfrè, C. ”A 20-Year Experience with Mitral Valve Repair with Artificial Chordae in 608 PA 20-year experience with Mitral Valve Repair with Artificial Chordae in 608 Patients”. *The Journal of Thoracic and Cardiovascular Surgery* **135,** 1280–1287 (2008).

39. Boyd, J. H., Edelman, J. B., Scoville, D. H. & Woo, Y. J. ”Tricuspid Leaflet Repair: Innovative Solutions”. *Annals of Cardiothoracic surgery* **6,** 248–254 (2017).

40. Jiang, X., Liu, J. & Gu, T. ”Successful Resection of a Posterior Tricuspid Leaflet Lipoma and Reconstruction of Tricuspid Valve”. *The Annals of Thoracic Surgery* **371,** 248–254 (2021).

41. Jaffer, I. H. & Whitlock, R. P. ”A Mechanical Heart Valve is the Best Choice”. *Heart Asia* **8,** 62–64 (2016).

42. Brennan, J. M., Edwards, F. H., Zhao, Y., O’Brien, S., Booth, M. E., Dokholyan, R. S., Douglas, P. S. & Peterson, E. D. ”Long-Term Safety and Effectiveness of Mechanical Versus Biologic Aortic Valve Prostheses in Older Patients”. *Circulation* **127,** 1647–1655 (2013).

43. Catterall, F., Ames, P. R. & Isles, C. ”Warfarin in Patients with Mechanical Heart Valves”. *British Medical Journal* **371,** 248–254 (2020).

44. Kostyunin, A. E., Yuzhalin, A. E., Rezvova, M. A., Ovcharenko, E. A., Glushkova, T. V. & Kutikhin, A. G. ”Degeneration of Bioprosthetic Heart Valves: Update 2020”. *Journal of the American Heart Association* **9,** e018506 (2020).

45. Hasan, A., Ragaert, K., Swieszkowski, W., Selimović, Š., Paul, A., Camci-Unal, G., Mofrad, M. R. & Khademhosseini, A. ”Biomechanical Properties of Native and Tissue Engineered Heart Valve Constructs”. *Journal of Biomechanics* **47,** 1949–1963 (2014).

46. May-Newman, K. & Yin, F. C. ”Biaxial Mechanical Behavior of Excised Porcine Mitral Valve Leaflets”. *American Journal of Physiology-Heart and Circulatory Physiology* **269,** H1319–H1327 (1995).

47. Heyden, S., Nagler, A., Bertoglio, C., Biehler, J., Gee, M. W., Wall, W. A. & Ortiz, M. ”Material Modeling of Cardiac Valve Tissue: Experiments, Constitutive Analysis and Numerical Investigation”. *Journal of Biomechanics* **48,** 4287–4296 (2015).

48. Khoiy, K. & Rouzbeh, A. ”On the Biaxial Mechanical Response of Porcine Tricuspid Valve Leaflets”. *Journal of Biomechanical Engineering* **138,** 104504 (2016).

49. Pierlot, C. M., Lee, M. J., Amini, R., Sacks, M. S. & Wells, S. M. ”Pregnancy-Induced Remodeling of Collagen Architecture and Content in the Mitral Valve”. *Annals of Biomedical Engineering* **42,** 2058–2071 (2014).

50. Ross, C., Laurence, D., Wu, Y. & Lee, C.-H. ”Biaxial Mechanical Characterizations of Atrioventricular Heart Valves”. *Journal of Visualized Experiments : JoVE* **146,** e59170 (2019).

51. Pokutta-Paskaleva, A., Sulejmani, F., DelRocini, M. & Sun, W. ”Comparative Mechanical, Morphological, and Microstructural Characterization of Porcine Mitral and Tricuspid Leaflets and Chordae Tendineae”. *Acta Biomaterialia* **85,** 241–252 (2019).

52. Meador, W. D., Mathur, M., Sugerman, G. P., Jazwiec, T., Malinowski, M., Bersi, M. R., Timek, T. A. & Rausch, M. K. ”A Detailed Mechanical and Microstructural Analysis of Ovine Tricuspid Valve Leaflets”. *Acta Biomaterialia* **102,** 100–113 (2020).

53. Pham, T., Sulejmani, F., Shin, E., Wang, D. & Sun, W. ”Quantification and Comparison of the Mechanical Properties of Four Human Cardiac Valves”. *Acta Biomaterialia* **54,** 345–355 (2017).

54. Grashow, J. S., Yoganathan, A. P. & Sacks, M. S. ”Biaixal Stress–Stretch Behavior of the Mitral Valve Anterior Leaflet at Physiologic Strain Rates”. *Annals of Biomedical Engineering* **34,** 315–324 (2006).

55. Grashow, J. S., Sacks, M. S., Liao, J. & Yoganathan, A. P. ”Planar Biaxial Creep and Stress Relaxation of the Mitral Valve Anterior Leaflet”. *Annals of Biomedical Engineering* **34,** 1509–1518 (2006).

56. Laurence, D., Ross, C., Jett, S., Johns, C., Echols, A., Baumwart, R., Towner, R., Liao, J., Bajona, P., Wu, Y. & Lee, C.-H. ”An Investigation of Regional Variations in the Biaxial Mechanical Properties and Stress Relaxation Behaviors of Porcine Atrioventricular Heart Valve Leaflets”. *Journal of Biomechanics* **83,** 16–27 (2019).

57. Huang, H.-Y. S., Balhouse, B. N. & Huang, S. ”Application of Simple Biomechanical and Biochemical Tests to Heart Valve Leaflets: Implications for Heart Valve Characterization and Tissue Engineering”. *Proceedings of the Institution of Mechanical Engineers, Part H: Journal of Engineering in Medicine* **226,** 868–876 (2012).

58. Martin, C. & Sun, W. ”Biomechanical Characterization of Aortic Valve Tissue in Humans and Common Animal Models”. *Journal of Biomedical Materials Research Part A* **100,** 1591–1599 (2012).

59. Kubíková, T., Kochová, P., Brázdil, J., Špatenka, J., Burkert, J., Králíčková, M. & Tonar, Z. ”The Composition and Biomechanical Properties of Human Cryopreserved Aortas, Pulmonary Trunks, and Aortic and Pulmonary Cusps”. *Annals of Anatomy-Anatomischer Anzeiger* **212,** 17–26 (2017).

60. Christie, G. W. & Barratt-Boyes, B. G. ”Mechanical Properties of pPorcine Pulmonary Valve Leaflets: How Do They Differ From Aortic Leaflets?”. *The Annals of Thoracic Surgery* **60,** S195–S199 (1995).

61. Billiar, K. L. & Sacks, M. S. ”Biaxial Mechanical Properties of the Natural and Glutaraldehyde Treated Aortic Valve Cusp—Part I: Experimental Results”. *Journal of Biomechanical Engineering* **122,** 23–30 (2000).

62. Anssari-Benam, A., Tseng, Y.-T., Holzapfel, G. A. & Bucchi, A. ”Rate-Dependency of the Mechanical Behaviour of Semilunar Heart Valves Under Biaxial Deformation”. *Acta Biomaterialia* **88,** 120–130 (2019).

63. Stella, J. A., Liao, J. & Sacks, M. S. ”Time-Dependent Biaxial Mechanical Behavior of the Aortic Heart Valve Leaflet”. *Journal of Biomechanics* **40,** 3169–3177 (2007).

64. Huang, S. & Huang, H.-Y. S. ”Biaxial Stress Relaxation of Semilunar Heart Valve Leaflets During Simulated Collagen Catabolism: Effects of Collagenase Concentration and Equibiaxial Strain State”. *Proceedings of the Institution of Mechanical Engineers, Part H: Journal of Engineering in Medicine* **229,** 721–731 (2015).

65. Anssari-Benam, A., Screen, H. R. & Bucchi, A. ”Insights Into the Micromechanics of Stress-Relaxation and Creep Behaviours in the Aortic Valve”. *Journal of the Mechanical Behavior of Biomedical Materials* **93,** 230–245 (2019).

66. Driessen, N. J., Bouten, C. V. & Baaijens, F. P. ”Improved Prediction of the Collagen Fiber Architecture in the Aortic Heart Valve”. *Journal of Biomechanical Engineering* **127,** 329–336 (2005).

67. Shoulders, M. D. & Raines, R. T. ”Collagen Structure and Stability”. *Annual Review of Biochemistry* **78,** 929–958 (2009).

68. Taylor, P. M. ”Biological Matrices and Bionanotechnology”. *Philosophical transactions of the Royal Society of London. Series B, Biological Sciences* **362,** 1313–1320 (2007).

69. Lee, C.-H., Zhang, W., Liao, J., Carruthers, C. A., Sacks, J. I. & Sacks, M. S. ”On the Presence of Affine Fibril and Fiber Kinematics in the Mitral Valve Anterior Leaflet”. *Biophysical Journal* **108,** 2074–2087 (2015).

70. Carruthers, C. A., Good, B., D’Amore, A., Liao, J., Amini, R., Watkins, S. C. & Sacks, M. S. *”Alterations in the Microstructure of the Anterior Mitral Valve Leaflet Under Physiological Stress”* in *Summer Bioengineering Conference* **44809** (2012), 227–228.

71. Zhang, W., Ayoub, S., Liao, J. & Sacks, M. S. ”A Meso-Scale Layer-Specific Structural Constitutive Model of the Mitral Heart Valve Leaflets”. *Acta Biomaterialia* **32,** 238–255 (2016).

72. Baugh, L. M., Liu, Z., Quinn, K. P., Osseiran, S., Evans, C. L., Huggins, G. S., Hinds, P. W., Black, L. D. & Georgakoudi, I. ”Non-Destructive Two-Photon Excited Fluorescence Imaging Identifies Early Nodules in Calcific Aortic-Valve Disease”. *Nature Biomedical Engineering* **1,** 914–924 (2017).

73. Hutson, H. N., Marohl, T., Anderson, M., Eliceiri, K., Campagnola, P. & Masters, K. S. ”Calcific Aortic Valve Disease is Associated with Layer-Specific Alterations in Collagen Architecture”. *PloS One* **11,** e0163858 (2016).

74. Sulejmani, F., Pokutta-Paskaleva, A., Salazar, O., Karimi, M. & Sun, W. ”Mechanical and Structural Analysis of the Pulmonary Valve in Congenital Heart Defects: A Presentation of Two Case Studies”. *Journal of the Mechanical Behavior of Biomedical Materials* **89,** 9–12 (2019).

75. Krahn, K. N., Bouten, C. V., van Tuijl, S., van Zandvoort, M. A. & Merkx, M. ”Fluorescently Labeled Collagen Binding Proteins Allow Specific Visualization of Collagen in Tissues and Live Cell Culture”. *Analytical Biochemistry* **350,** 117–118 (2006).

76. Ghazanfari, S., Driessen-Mol, A., Sanders, B., Dijkman, P. E., Hoerstrup, S. P., Baaijens, F. P. & Bouten, C. V. ”In Vivo Collagen Remodeling in the Vascular Wall of Decellularized Stented Tissue-Engineered Heart Valves”. *Tissue Engineering Part A* **21,** 2205–2215 (2015).

77. Ghazanfari, S., Driessen-Mol, A., Strijkers, G. J., Baaijens, F. P. & Bouten, C. V. ”The Evolution of Collagen Fiber Orientation in Engineered Cardiovascular Tissues Visualized by Diffusion Tensor Imaging”. *PLoS One* **10,** e0127847 (2015).

78. Oomen, P., Loerakker, S., Van Geemen, D., Neggers, J., Goumans, M.-J., Van Den Bogaerdt, A., Bogers, A., Bouten, C. & Baaijens, F. ”Age-Dependent Changes of Stress and Strain in the Human Heart Valve and Their Relation with Collagen Remodeling”. *Acta Biomaterialia* **29,** 161–169 (2016).

79. Schenke-Layland, K., Madershahian, N., Riemann, I., Starcher, B., Halbhuber, K.-J., König, K. & Stock, U. A. ”Impact of Cryopreservation on Extracellular Matrix Structures of Heart Valve Leaflets”. *The Annals of Thoracic Surgery* **81,** 918–926 (2006).

80. Van de Hulst, H. ”Light Scattering by Small Particles”. *Quarterly Journal of the Royal Meteorological Society* **84,** 198–199 (1958).

81. Kunzelman, K. S. & Cochran, R. P. ”Stress/Strain Characteristics of Porcine Mitral Valve Tissue: Parallel Versus Perpendicular Collagen Orientation”. *Journal of Cardiac Surgery* **7,** 71–78 (1992).

82. Jouk, P.-S., Mourad, A., Milisic, V., Michalowicz, G., Raoult, A., Caillerie, D. & Usson, Y. ”Analysis of the Fiber Architecture of the Heart by Quantitative Polarized Light Microscopy. Accuracy, Limitations and Contribution to the Study of the Fiber Architecture of the Ventricles During Fetal and Neonatal Life”. *European Journal of Cardio-Thoracic Surgery* **31,** 915–921 (2007).

83. Rock, C. A., Han, L. & Doehring, T. C. ”Complex Collagen Fiber and Membrane Morphologies of the Whole Porcine Aortic Valve”. *PLoS One* **9,** e86087 (2014).

84. Liao, J., Joyce, E. M. & Sacks, M. S. ”Effects of Decellularization on the Mechanical and Structural Properties of the Porcine Aortic Valve Leaflet”. *Biomaterials* **29,** 1065–1074 (2008).

85. Joyce, E. M., Liao, J., Schoen, F. J., Mayer Jr, J. E. & Sacks, M. S. ”Functional Collagen Fiber Architecture of the Pulmonary Heart Valve Cusp”. *The Annals of Thoracic Surgery* **87,** 1240–1249 (2008).

86. Sacks, M. S., Smith, D. B. & Hiester, E. D. ”A Small Angle Light Scattering Device for Planar Connective Tissue Microstructural Analysis”. *Annals of Biomedical Engineering* **25,** 678–689 (1997).

87. Sacks, M. S., Smith, D. B. & Hiester, E. D. ”The Aortic Valve Microstructure: Effects of Transvalvular Pressure”. *Journal of Biomedical Materials Research* **41,** 131–141 (1998).

88. Thomas, V. S., Lai, V. & Amini, R. ”A Computational Multi-Scale Approach to Investigate Mechanically-Induced Changes in Tricuspid Valve Anterior Leaflet Microstructure”. *Acta Biomaterialia* **94,** 524–535 (2019).

89. Pant, A. D., Thomas, V. S., Black, A. L., Verba, T., Lesicko, J. G. & Amini, R. ”Pressure-Induced Microstructural Changes in Porcine Tricuspid Valve Leaflets”. *Acta Biomaterialia* **67,** 248–258 (2018).

90. Billiar, K. L. & Sacks, M. S. ”Biaxial Mechanical Properties of the Native and Glutaraldehyde-Treated Aortic Valve Cusp: Part II — A Structural Constitutive Model”. *Journal of Biomechanical Engineering* **122,** 327–355 (2000).

91. Yang, B., Lesicko, J., Sharma, M., Hill, M., Sacks, M. S. & Tunnell, J. W. ”Polarized Light Spatial Frequency Domain Imaging for Non-Destructive Quantification of Soft Tissue Fibrous Structures”. *Biomedical Optics Express* **6,** 1520–1533 (2015).

92. Goth, W., Potter, S., Allen, A. C., Zoldan, J., Sacks, M. S. & Tunnell, J. W. ”Non-Destructive Reflectance Mapping of Collagen Fiber Alignment in Heart Valve Leaflets”. *Annals of Biomedical Engineering* **47,** 1250–1264 (2019).

93. Chen, X., Nadiarynkh, O., Plotnikov, S. & Campagnola, P. J. ”Second Harmonic Generation Microscopy for Quantitative Analysis of Collagen Fibrillar Structure”. *Nature Protocols* **7,** 654–669 (2012).

94. Schriefl, A. J., Wolinski, H., Regitnig, P., Kohlwein, S. D. & Holzapfel, G. A. ”An Automated Approach for Three-Dimensional Quantification of Fibrillar Structures in Optically Cleared Soft Biological Tissues”. *Journal of The Royal Society Interface* **10,** 20120760 (2013).

95. Zhang, Y., Akins, M. L., Murari, K., Xi, J., Li, M.-J., Luby-Phelps, K., Mahendroo, M. & Li, X. ”A Compact Fiber-Optic SHG Scanning Endomicroscope and its Application to Visualize Cervical Remodeling During Pregnancy”. *Proceedings of the National Academy of Sciences* **109,** 12878–12883 (2012).

96. Goth, W., Lesicko, J., Sacks, M. S. & Tunnell, J. W. ”Optical-Based Analysis of Soft Tissue Structures”. *Annual Review of Biomedical Engineering* **18,** 357–385 (2016).

97. Hill, M. R., Duan, X., Gibson, G. A., Watkins, S. & Robertson, A. M. ”A Theoretical and Non-Destructive Experimental Approach for Direct Inclusion of Measured Collagen Orientation and Recruitment into Mechanical Models of the Artery Wall”. *Journal of Biomechanics* **45,** 762–771 (2012).

98. Jett, S. V., Hudson, L. T., Baumwart, R., Bohnstedt, B. N., Mir, A., Burkhart, H. M., Holzapfel, G. A., Wu, Y. & Lee, C.-H. ”Integration of polarized Spatial Frequency Domain Imaging (pSFDI) with a Biaxial Mechanical Testing System for Quantification of Load-Dependent Collagen Architecture in Soft Collagenous Tissues”. *Acta Biomaterialia* **102,** 149–168 (2020).

99. Salinas, S. D., Clark, M. M. & Amini, R. ”Mechanical Response Changes in Porcine Tricuspid Valve Anterior Leaflet Under Osmotic-Induced Swelling”. *Bioengineering* **6,** 70 (2019).

100. Cuccia, D. J., Bevilacqua, F., Durkin, A. J. & Tromberg, B. J. ”Modulated Imaging: Quantitative Analysis and Tomography of Turbid Media in the Spatial-Frequency Domain”. *Optics Letters* **30,** 1354–1356 (2005).

101. Cuccia, D. J., Bevilacqua, F. P., Durkin, A. J., Ayers, F. R. & Tromberg, B. J. ”Quantitation and Mapping of Tissue Optical Properties Using Modulated Imaging”. *Journal of Biomedical Optics* **14,** 024012 (2009).

102. Mazhar, A., Saggese, S., Pollins, A. C., Cardwell, N. L., Nanney, L. B. & Cuccia, D. J. ”Noncontact Imaging of Burn Depth and Extent in a Porcine Model Using Spatial Frequency Domain Imaging”. *Journal of Biomedical Optics* **19,** 086019 (2014).

103. Hudson, L. T., Jett, S. V., Kramer, K. E., Laurence, D. W., Ross, C. J., Towner, R. A., Baumwart, R., Lim, K. M., Mir, A. & Burkhart, H. M. ”A Pilot Study on Linking Tissue Mechanics with Load-Dependent Collagen Microstructures in Porcine Tricuspid Valve Leaflets”. *Bioengineering* **7,** 60 (2020).

104. Laurence, D. W., Homburg, H., Yan, F., Tang, Q., Fung, K.-M., Bohnstedt, B. N., Holzapfel, G. A. & Lee, C.-H. ”A Pilot Study on Biaxial Mechanical, Collagen Microstructural, and Morphological Characterizations of a Resected Human Intracranial Aneurysm Tissue”. *Nature Scientific Reports* **11,** 1–15 (2021).

105. Ross, C. J., Hsu, M.-C., Baumwart, R., Mir, A., Burkhart, H. M., Holzapfel, G. A., Wu, Y. & Lee, C.-H. ”Quantification of Load-Dependent Changes in the Collagen Fiber Architecture for the Strut Chordae Tendineae-Leaflet Insertion of Porcine Atrioventricular Heart Valves”. *Biomechanics and Modeling in Mechanobiology* **20,** 223–241 (2021).

106. Ruifrok, A. C. & Johnston, D. A. ”Quantification of Histochemical Staining by Color Deconvolution”. *Analytical and Quantitative Cytology and Histology* **23,** 291–299 (2001).

107. Mathur, M., Jazwiec, T., Meador, W., Malinowski, M., Goehler, M., Ferguson, H., Timek, T. & Rausch, M. ”Tricuspid Valve Leaflet Strains in the Beating Ovine Heart”. *Biomechanics and Modeling in Mechanobiology* **18,** 1351–1361 (2019).

108. Fung, Y. ”Structure and Stress-Strain Relationship of Soft Tissues”. *American Zoologist* **24,** 13–22 (1984).

109. Lanir, Y. ”A Structural Theory for the Homogeneous Biaxial Stress-Strain Relationships in Flat Collagenous Tissues”. *Journal of Biomechanics* **12,** 423–436 (1979).

110. Lanir, Y. ”Constitutive Equations for Fibrous Connective Tissues”. *Journal of Biomechanics* **16,** 1–12 (1983).

111. Liao, J., Yang, L., Grashow, J. & Sacks, M. S. ”The Relation between Collagen Fibril Kinematics and Mechanical Properties in the Mitral Valve Anterior Leaflet”. *Journal of Biomechanical Engineering* **129,** 78–87 (2007).

112. Duginski, G. A., Ross, C. J., Laurence, D. W., Johns, C. H. & Lee, C.-H. ”An Investigation of the Effect of Freezing Storage on the Biaxial Mechanical Properties of Excised Porcine Tricuspid Valve Anterior Leaflets”. *Journal of the Mechanical Behavior of Biomedical Materials* **101,** 103438 (2020).

113. Huang, H.-Y. S., Liao, J. & Sacks, M. S. ”In-Situ Deformation Of the Aortic Valve Interstitial Cell Nucleus Under Diastolic Loading”. *Journal of Biomechanical Engineering* **129,** 880–889 (2007).

114. Ayoub, S., Tsai, K. C., Khalighi, A. H. & Sacks, M. S. ”The Three-Dimensional Microenvironment of the Mitral Valve: Insights Into the Effects of Physiological Loads”. *Cellular and Molecular Bioengineering* **11,** 291–306 (2018).

115. Lee, C.-H., Carruthers, C. A., Ayoub, S., Gorman, R. C., Gorman III, J. H. & Sacks, M. S. ”Quantification and simulation of Layer-specific Mitral Valve Interstitial Cells Deformation Under Physiological Loading”. *Journal of Theoretical Biology* **373,** 26–39 (2015).

116. Chandran, P. L. & Barocas, V. H. ”Affine Versus Non-Affine Fibril Kinematics in Collagen Networks: Theoretical Studies of Network Behavior”. *Journal of Biomechanical Engineering* **128,** 259–270 (2006).

117. Billiar, K. & Sacks, M. ”A Method to Quantify the Fiber Kinematics of Planar Tissues Under Biaxial Stretch”. *Journal of Biomechanics* **30,** 753–756 (1997).

118. Jan, N.-J. & Sigal, I. A. ”Collagen Fiber Recruitment: A Microstructural Basis for the Nonlinear Response of the Posterior Pole of the Eye to Increases in Intraocular Pressure”. *Acta Biomaterialia* **72,** 295–305 (2018).

119. Zeinali-Davarani, S., Wang, Y., Chow, M.-J., Turcotte, R. & Zhang, Y. ”Contribution of Collagen Fiber Undulation to Regional Biomechanical Properties Along Porcine Thoracic Aorta”. *Journal of Biomechanical Engineering* **137,** 051001 (2015).

120. Rego, B. V., Wells, S. M., Lee, C.-H. & Sacks, M. S. ”Mitral Valve Leaflet Remodelling During Pregnancy: Insights into Cell-Mediated Recovery of Tissue Homeostasis”. *Journal of The Royal Society Interface* **13,** 20160709 (2016).

121. Votta, E., Caiani, E., Veronesi, F., Soncini, M., Montevecchi, F. M. & Redaelli, A. ”Mitral Valve Finite-Element Modelling from Ultrasound Data: A Pilot Study for a New Approach to Understand Mitral Function and Clinical Scenarios”. *Philosophical Transactions of the Royal Society A: Mathematical, Physical and Engineering Sciences* **366,** 3411–3434 (2008).

122. Wenk, J. F., Zhang, Z., Cheng, G., Malhotra, D., Acevedo-Bolton, G., Burger, M., Suzuki, T., Saloner, D. A., Wallace, A. W. & Guccione, J. M. ”First Finite Element Model of the Left Ventricle with Mitral Valve: Insights into Ischemic Mitral Regurgitation”. *The Annals of Thoracic Surgery* **89,** 1546–1553 (2010).

123. Stephens, E. H., de Jonge, N., McNeill, M. P., Durst, C. A. & Grande-Allen, K. J. ”Age-Related Changes in Material Behavior of Porcine Mitral and Aortic Valves and Correlation to Matrix Composition”. *Tissue Engineering Part A* **16,** 867–878 (2010).

124. Bernacca, G. M., O’Connor, B., Williams, D. F. & Wheatley, D. J. ”Hydrodynamic Function of Polyurethane Prosthetic Heart Valves: Influences of Young’s Modulus and Leaflet Thickness”. *Biomaterials* **23,** 45–50 (2002).

125. Sun, W., Sacks, M. S. & Scott, M. J. ”Effects of Boundary Conditions on the Estimation of the Planar Biaxial Mechanical Properties of Soft Tissues”. *Journal of Biomechanical Engineering* **127,** 709–715 (2005).

126. Waldman, S. D. & Lee, J. M. ”Boundary Conditions During Biaxial Testing of Planar Connective Tissues. Part 1: Dynamic Behavior”. *Journal of Materials Science: Materials in Medicine* **13,** 933–938 (2002).

127. May-Newman, K., Lam, C. & Yin, F. C. ”A Hyperelastic Constitutive Law for Aortic Valve Tissue”. *Journal of Biomechanical Engineering* **131,** 081009 (2009).

128. Weinberg, E. J. & Mofrad, M. R. K. ”Transient, Three-Dimensional, Multiscale Simulations of the Human Aortic Valve”. *Cardiovascular Engineering* **7,** 140–155 (2007).